LOCALLY CONTROLLED PHOTONIC CRYSTAL DEVICES WITH COUPLED QUANTUM DOTS: PHYSICS AND APPLICATIONS

A DISSERTATION
SUBMITTED TO THE DEPARTMENT OF APPLIED PHYSICS
AND THE COMMITTEE ON GRADUATE STUDIES
OF STANFORD UNIVERSITY
IN PARTIAL FULFILLMENT OF THE REQUIREMENTS
FOR THE DEGREE OF
DOCTOR OF PHILOSOPHY

Andrei Faraon
August 2009

I certify that I have read this dissertation and that, in my opinion, it is fully adequate in scope and quality as a dissertation for the degree of Doctor of Philosophy.

(Jelena Vučković) Principal Adviser

I certify that I have read this dissertation and that, in my opinion, it is fully adequate in scope and quality as a dissertation for the degree of Doctor of Philosophy.

(Yoshihisa Yamamoto)

I certify that I have read this dissertation and that, in my opinion, it is fully adequate in scope and quality as a dissertation for the degree of Doctor of Philosophy.

(David A.B. Miller)

Approved for the University Committee on Graduate Studies.

Abstract

One of the most promising ways of building future nano-photonic networks for classical and quantum information processing is by using photonic crystals. Quantum dots coupled to optical modes allow for efficient control of light in these devices. In this dissertation I present the work I have done at Stanford University toward building integrated photonic crystal devices with coupled quantum dots.

The most significant experiments that we performed on this platform relied on perfecting the fabrication techniques for photonic crystals, and developing technologies for local control of the cavity and quantum dot properties. In terms of fabrication, our lab is currently able to make state of the art GaAs photonic crystal cavities operating at the wavelength around 930nm with quality factors up to 25000. Combined with quantum dots, these cavities allowed us to achieve the strong coupling regime, which opened the possibility to perform fundamental experiments on cavity quantum electrodynamics. Regarding the local control of cavities and quantum dots, we have developed several techniques. Two of them relied on controlling the local temperature either via laser heating or micron-scale ohmic heaters. Another technique was based on in situ change of the index of refraction using chalcogenide glasses. Finally, we have also developed a method to control the quantum dot properties via a local electric field applied using metallic electrodes.

The local temperature tuning played an essential role in the first experiments on coherent probing of strongly coupled cavity - quantum dot systems. The coherent probing technique enabled a series of fundamental experiments where the quantum dot in the cavity was used as a non-linear medium with an ultra-small mode volume. In one experiment, the phase of photons interacting with the system could be

controlled via optical fields at power levels as low as one photon per characteristic lifetime of the system. Another experiment investigated quantum nonlinearities of the cavity - quantum dot system by demonstrating photon blockade and photon-induced tunneling.

The great promise of using photonic crystals is that they can be combined in an integrated on-chip optical network. To this end, we have developed integrated devices that assemble resonators, waveguide, input/output couplers, and elements for local tuning. Single quantum dots were coupled to the resonators so they could act as on-chip light switches operating at the fundamental limit of light-matter interaction.

For opto-electronic applications, the manipulation of light on a chip should be done either all optically or electrically. For electrical control we have developed techniques where the resonance of the quantum dot in the cavity is controlled by applying a lateral electric field using a metallic electrode. This switch has the promise to operate at energies per switching operation below 1 fJ, orders of magnitude lower than current state of the art devices. The goal is to extend this technique for waveguide-coupled cavities such that electro-optic switching can be implemented for on-chip optical signal processing.

Acknowledgement

The PhD is the first academic experience where the success can not be guaranteed solely by studying hard to accomplish a certain set of academic requirements. It is equally important to learn how to interact and develop solid relationships with all the people in scientific community. During my stay at Stanford I was privileged to work with some of the finest scientists in my research field and I am grateful for all the guidance they have given me.

First of all, I would like to thank my research adviser, Prof. Jelena Vuckovic, for giving me the opportunity to join her research group. I am especially grateful that in her group I found the right balance between theoretical and experimental work, fundamental and applied research. Not only does the Vuckovic group excel in developing cutting edge science and technology, but also she managed to assemble an extraordinary research team where research ideas can flourish, solid working relationships can be developed, and friendships can be built. While in Jelena's group I had plenty of freedom to pursue various research directions, and she was always present to give appropriate guidance. She encouraged me to present at numerous conferences and seminars thus giving me the opportunity to interact with scientists from all over the world.

I would also like to thank the members of my oral and reading committee: Prof. Yoshihisa Yamamoto who was also my academic adviser, Prof. David Miller, Prof. Hideo Mabuchi and Prof. Mark Brongersma. All of them, in many occasions, took time to discuss academic questions with me.

In my first PhD years, I worked very closely with Dirk Englund and Ilya Fushman who joined Jelena's group more than a year before I did, and with Dr. Edo Waks.

In a research group, the senior students and postdocs have the great responsibility of closely guiding the other group members, teaching them the working etiquette, and many times being role models. I was very lucky to work with Edo, Ilya and Dirk. They have the merit of setting my scientific aspirations very high, and showing me every day what it takes to become a truly accomplished scientist. Working with them has been challenging, fun, and rewarding. Toward the end of my PhD I worked very closely with junior students Arka Majumdar, Carter Lin and Kelley Rivoire, extremely gifted young scientists who greatly challenged me with their sharp thinking and richness of research ideas. Given the highly collaborative environment encouraged by Jelena, over my PhD I had the opportunity to interact with most of the members of group: Mitsuru Toishi, Hatice Altug, Maria Makarova, Vanessa Sih, Bryan Ellis, Yiyang Gong, Jesse Lu, Gary Shambat.

One of the reasons why Stanford Applied Physics is such a great place to study, is that students have the opportunity to rotate for one quarter in several research groups until they find the best match. I fully took advantage of the rotation system and I worked in the labs of three different professors before joining Jelena's group: Prof. Marty Fejer, Prof. Mark Kasevich and Prof. Yoshihisa Yamamoto. I thank all of them for accepting me in their groups. The rotations contributed a lot to my scientific breath and helped me find the area of science that best matched my interests. As a rotation student I interacted with several students with whom I developed solid academic relationships: Luigi Scaccabarozzi, Jason Hogan, Jonathan Goldman and Thaddeus Ladd.

I am very grateful to my family who encouraged me to study and made everything possible for me. When the time came to choose a career they advised me to choose the field I liked the most.

Finally, I thank my wife Viviana, who was next to me for my entire graduate and undergraduate years. I am very lucky to have met her. She is my best friend and a great scientist, with whom I can share so closely the same life values.

Contents

List of Tables

List of Figures

Chapter 1

Introduction

1.1 Solid state photonic networks for classical and quantum information processing

During the past decade, the field of micro and nano photonics has witnessed an exponential growth, mainly driven by the increased demand for on-chip optical signal processing. There are several types of mechanisms that allow for control of light at micro and nano scale levels: total internal reflection (TIR)[1], plasmonics [2] and photonic crystals (PCs) [3, 1]. Each of these mechanisms has both advantages and disadvantages depending on the specific application. Devices based on total internal reflection, like micro-toroids, micro-disks and micro-spheres are well known for their ultra-high quality factors and are well suited for integration with optical fiber networks [1], but they have large volumes. Plasmonic devices allow for ultra small optical mode volume and at the same time electrical control can be easily implemented. However, they generally suffer from high optical losses. Photonic crystal devices can be used to confine light in either one (1D), two (2D) or three (3D) dimensions. The 1D photonic crystals (micro-posts or micro-pillars) are well suited for applications where both ultra-small mode volume and good butt-coupling into fibers is needed. The 2D(3D) photonic crystals hold great promise because they allow for sub-wavelength confinement of light in devices that can be monolithically integrated in a 2D(3D)

photonic network. At the same time, they support high and even ultra-high quality factors.

So far, the primary use of photonic micro-resonators has been limited to increasing the efficiency of lasers (e.g., VCSELs) and LEDs. However, nano photonics holds great promise for building on-chip optical networks for classical and quantum information processing. Regarding the classical applications, there is already advanced research on chip-based optical interconnects that would replace the electrical wiring inside computers [4, 5, 6, 7, 8, 9].

The first proposals for optical quantum information processing devices were based on cavity quantum electrodynamics (CQED) systems in atomic physics [10, 11]. In principle, these systems consist of macroscopic optical resonators coupled to atoms or ions that are interconnected via optical beams propagating through free space. Most of the proof of concept experiments have been done in this type of systems [12, 13, 14, 15]. However, their main drawback is the reduced potential for scalability due to their high complexity and macroscopic size. One solution is to implement CQED systems using solid state photonics that has the potential for monolithic fabrication and thus large scale scalability. All the required components for solid state CQED already exist. Optical microcavities with low loss can be built using both whispering gallery modes as in microrings and microdisks, or photonic bandgap materials as in photonic crystals or micropost cavities. Several options exist for suitable optical emitters, like InAs quantum dots (QDs) in GaAs [16], nitrogen vacancy (NV) centers in diamond [17], rare earth ions in orthosilicates [18], or other impurities in different host materials. The advantage of using NV centers and rare earth ions is an inherent quantum structure that allows for coherent q-bit manipulation at room temperature and without applying large magnetic fields. Their disadvantage is that the host material is very hard to process at the micro-scale. Quantum dots on the other hand are grown on semiconductor wafers thus giving the possibility of using all the techniques developed for integrated circuits.

InAs quantum dots coupled to GaAs photonic crystal devices have been so far one of the most successful testbeds for integrated solid state quantum information science, and our group at Stanford has done some of the seminal experiments in the

field [19, 20, 21]. In the remaining of this chapter I will introduce photonic crystals and quantum dots, and I will describe how they can be combined into an integrated platform for quantum information processing.

1.2 Photonic crystal resonators and waveguides

Photonic crystals are made by periodic arrangements of optical media with various refractive indexes. The light in such structures is controlled via Distributed Bragg Reflection (DBR), that allows for the development of photonic band gaps analogous to the electronic bandgaps in semiconductors. In such a material and at frequencies inside the photonic band gap, the propagation of light is prohibited along certain directions. The 2D photonic crystals drew most attention because they can be fabricated in a monolithic fashion using techniques already well developed in the semiconductor industry. They were also our platform of choice for building integrated photonic crystal devices with embedded quantum dots. The most common form for 2D photonic crystals is a periodic lattice of holes patterned in a thin suspended membrane of high refractive index material. The lattice of choice is either triangular or square as shown in Fig.1.1.

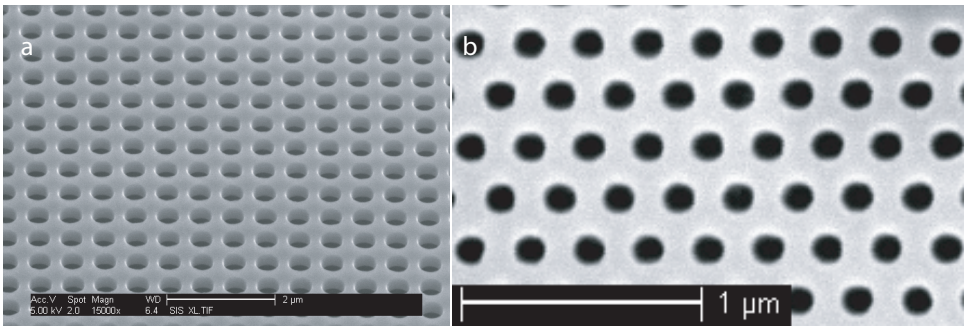

Figure 1.1: (a) Photonic crystal with square lattice fabricated in Si (fabricated by Hatice Altug). (b) Triangular lattice photonic crystal fabricated in GaAs.

The confinement of light can be achieved by introducing perturbations into the

periodicity of the photonic lattice, which leads to formation of photonic crystal cavities. The design of 2D photonic crystal cavities has been perfected in the past few years, such that resonators with quality factors as high as $Q \sim 2.5 \times 10^6$ and mode volumes of $V \sim 1.4(\lambda/n)^3$ (λ is the wavelength in vacuum and n is the index of refraction) have been fabricated in silicon [22]. The confinement of light in these structures is achieved by combination of a DBR (in PC plane) and TIR in the remaining (perpendicular) direction. These state of the art resonators are carefully designed using photonic crystal heterostructures that are very sensitive to any fabrication imperfections. Resonators with quality factors on the order of few thousands, that are very robust to fabrication imperfections, can be obtained by omitting and shifting a few holes in the lattice. In a triangular lattice, depending on the number of omitted holes, the resonators are designated as H0 (two shifted holes) [23, 24], H1 (one omitted hole)[25], L3 (three omitted holes)[26] etc. In our work at Stanford we have used all of these types of resonators, but the most successful work was done first with H1 cavities [27] and later with L3 cavities operating around $930nm$.

Most of the photonic crystal devices were fabricated in a $160nm$ thick GaAs membrane. This membrane was grown via molecular beam epitaxy (MBE) on top of a $1\mu m$ thick AlGaAs sacrificial layer sitting on the GaAs substrate. The photonic crystals were first patterned in the membrane using electron beam lithography and dry plasma etching. Then, the AlGaAs was wet etched resulting in suspended photonic crystal membranes. The detailed fabrication process is described in Appendix. A.

A scanning electron microscope (SEM) image of a linear three hole defect cavity (L3) is shown in Fig.1.2. This type of cavity supports more than one optical mode, as discussed in Ref.[28]. The most widely used is the fundamental mode with electromagnetic field profile shown in Fig.1.3. The mode is TE (transversal electric)-like with the electric field direction primarily in the plane, and the magnetic field direction perpendicular to the plane of the slab. The design of the cavity can be engineered so that this mode can reach quality factors on the order of hundreds of thousands and optical mode volumes smaller than one cubic optical wavelength. There are several reasons why the L3 cavity is very attractive for applications where a single nano-scale emitter needs to be coupled to the cavity mode. First, it provides a good trade off

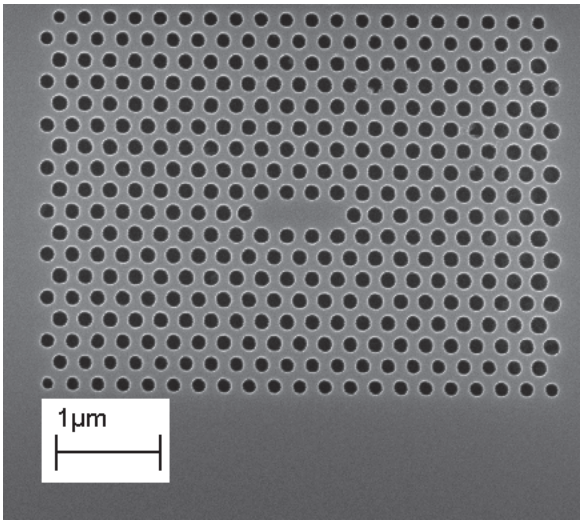

Figure 1.2: Linear three hole defect (L3) cavity fabricated in GaAs. The lattice constant is 246nm and the membrane thickness is 160nm.

between a high quality factor to mode volume (Q/V) ratio and a considerable effective area where an emitter can be placed. Second, it is robust to fabrication imperfections in the sense that the quality factor does not degrade, and the resonance wavelength shifts only by a few percent, when the parameters of the photonic crystal vary because of fluctuations in the fabrication process.

The L3 cavity can be easily connected with photonic crystal waveguides, as described in greater detail in Section 4.2. We used W1 waveguides created by omitting a row of holes in the triangular lattice (Fig.1.4(a)). These waveguides support several modes with different symmetry[28]. The fundamental mode has the same symmetry as the fundamental mode of the L3 cavity thus enabling good coupling efficiencies. The profile of the electromagnetic field and the band diagram of the W1 waveguide are shown in Fig.1.4(b). It can be observed that the dispersion relation for this waveguide is not linear. Thus, one has freedom to operate close to the π/a point where the band is almost flat and the group velocity is slow, or away from the π/a point where the dispersion is linear thus limiting the distortion of optical pulses (a is the periodicity of photonic crystal lattice). For all applications for integrated optical devices, it is desirable to operate below the light line to minimize the losses.

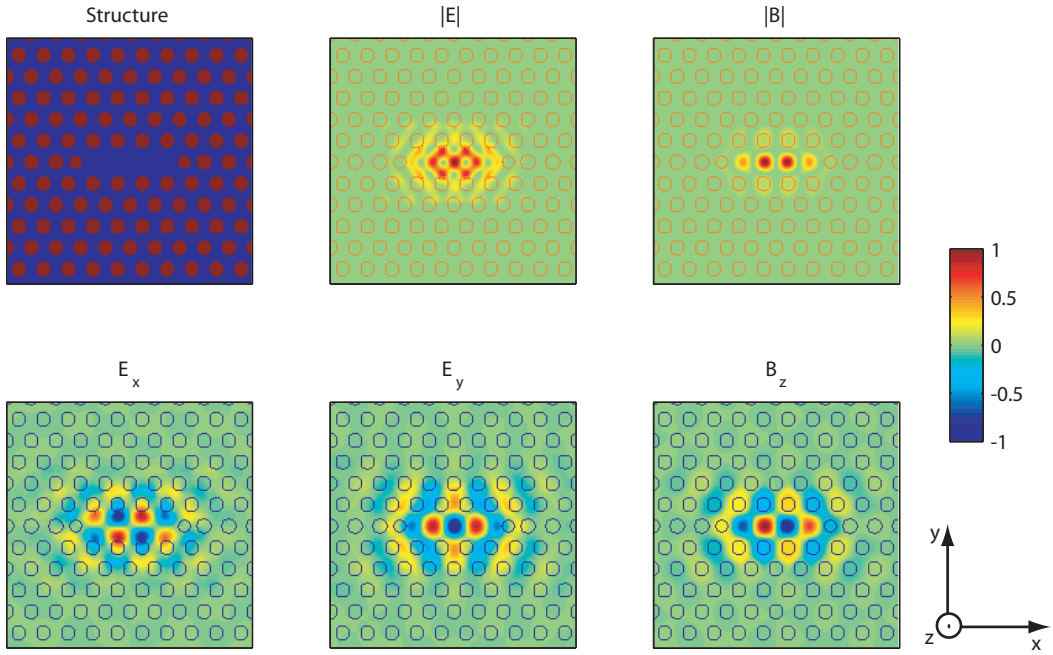

Figure 1.3: (a) Simulated L3 photonic crystal cavity. (b) Magnitude of electric field of the fundamental mode at the central plane of the slab. (d) x -component of electric field (e) y-component of electric field (f) z-component of magnetic field.

1.3 InAs quantum dots

There are several types of quantum dots, but the most widely used are the self assembled InAs quantum dots in GaAs. They were the emitters of choice for the CQED work done by our group during my PhD.

The self assembled InAs quantum dots are three dimensional islands of InAs embedded in GaAs. These dots are grown by molecular beam epitaxy on GaAs wafers as described in Ref.[29]. The quantum dots used in our experiment were grown in the group of Prof. Pierre Petroff at University of California at Santa Barbara. These quantum dots are disk-shaped with a lateral dimension of $\sim 20nm$ and thickness of $\sim 3nm$. Due to the bandgap difference between GaAs (1.42eV) and InAs (0.35eV), these quantum dots form an effective three dimensional potential well that can serve as a trapping potential for electrons and holes. The tight spatial confinement causes

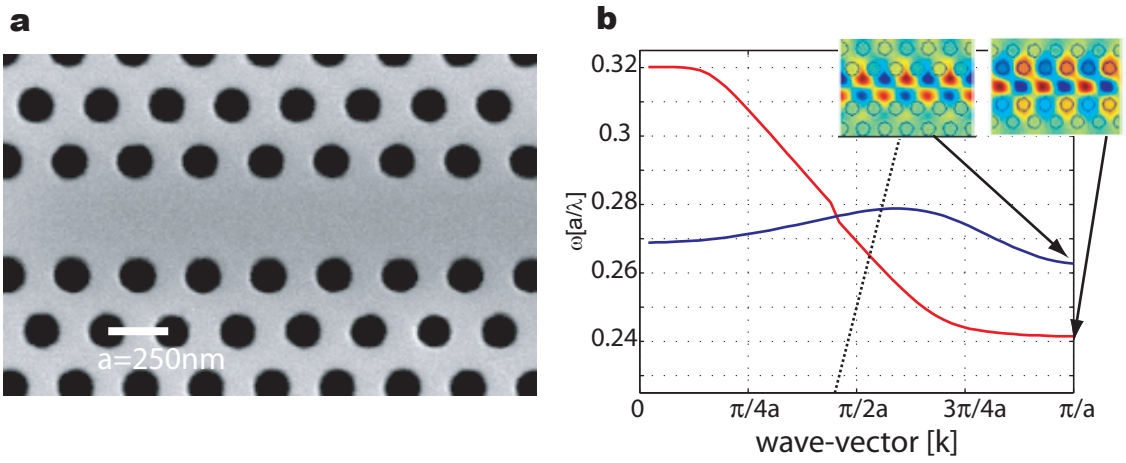

Figure 1.4: (a) Fabricated W1 waveguide. (b) Photonic band diagram, giving the allowed pairs of frequencies and wave-vectors for modes that can propagate through such waveguide. Frequency is plotted in normalized units a/λ, where lambda is the free-space wavelength and a is the lattice periodicity. The wave-vector k is along the wave-guide axis direction. The light line is marked with a black dotted line. The insets show the profile of the out of plane component of the magnetic field.

the energy levels of the quantum dot to be discrete, so the QDs can exhibit atom-like properties. A schematic representation of the energy levels in a QD is shown in Fig.1.5. InAs quantum dots can be designed to operate at various wavelengths spanning the entire near infrared spectrum. For applications in quantum information science it is desirable to operate below the wavelength of $1\mu m$ because of the high performance silicon photodetectors available in this wavelength range. However, in QDs operating at short wavelengths, the ground state energy of the quantum dot is very close to the GaAs bandgap, so carriers confined in the QD can be scattered out by phonon interactions at energy levels of kT (k the Boltzmann constant and T the temperature). To minimize the effect of phonon scattering, the QDs must be cooled down at temperatures below 50K. In all of our measurements we used a continuous flow He cryostat(Janis ST-500).

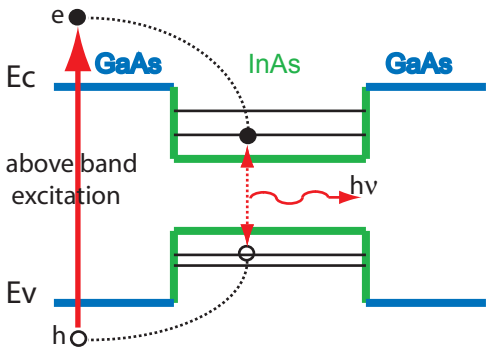

Figure 1.5: Above band excitation of InAs quantum dots. A laser excites carriers above the band gap of GaAs. These carriers can migrate, get trapped in the quantum dot, and then get recombined with the emission of one photon. The emitted photon has a frequency given by the energy difference between the discrete energy levels in the quantum dot.

One of the major drawbacks of all solid-state emitters is the inhomogeneous wavelength broadening. In the case of InAs quantum dots, this broadening is caused by the randomness associated with the MBE self assembly process. Another drawback is the random spatial distribution of the quantum dots. In Fig.1.6 we show the typical spectrum of an ensemble of quantum dots and an AFM image indicating the spatial distribution. In Chapter 2, I discuss the experimental results on local control of the quantum dot frequency that allows for spectral matching between multiple quantum dots coupled to microresonators on the same chip.

Quantum dots can be probed both optically and electrically[29]. One of the most straight-forward methods for probing is via photoluminescence as shown in Fig.1.5. In a photoluminescence measurement, electron-hole pairs are excited in the GaAs surrounding the QDs using a laser tuned above the bangap of GaAs. These carriers migrate in the semiconductor and get trapped in the QD. Finally they recombine with the emission of a photon.

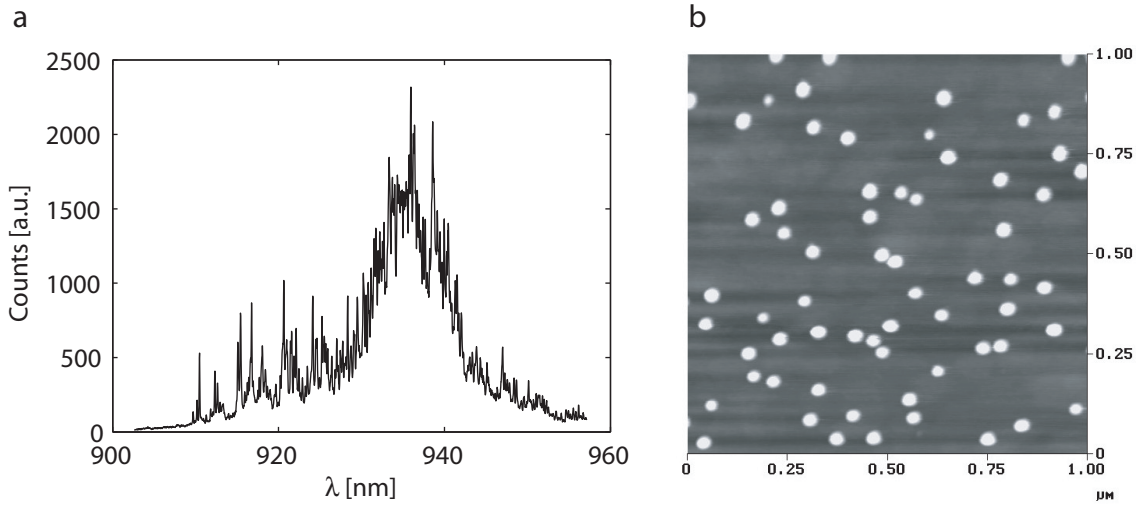

Figure 1.6: (a) Spectrum of an ensemble of quantum dots (grown by Bingyang Zhang, Stanford) showing the inhomogeneous broadening (b) Atomic force microscope image of quantum dots (un-capped) showing their random spatial distribution.

1.4 Quantum dots in photonic crystal resonators

1.4.1 Embedding quantum dots in photonic crystals

Combining quantum dots and photonic crystal devices requires a special design for the semiconductor wafer. Since the photonic crystal devices are patterned in a photonic crystal membrane that is just $160nm$ thick, the quantum dots are pre-grown in a layer located in the middle of the membrane as shown in Fig.1.7.

For CQED experiments, it is desirable that only one quantum dot is coupled to the cavity. The coupling involves both spatial overlap and frequency matching. In Chapter 2 I discuss our techniques for local tuning of the quantum dot and cavity resonance. Regarding the spatial overlap, one can either rely on chance on use positioning techniques. Several positioning techniques have been developed by other research groups. Some of them are based on identifying a QD via atomic force microscopy[30] or optical microscopy [31]. In our group, we opted to use random

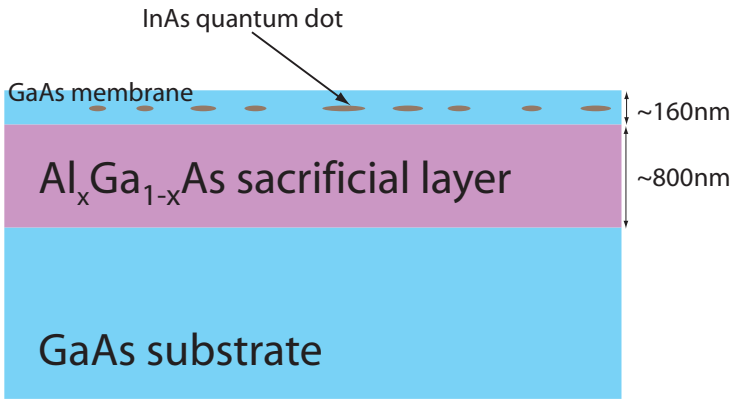

Figure 1.7: Schematic representation (not drawn to scale) of MBE grown GaAs membrane on top to $Al_xGa_(1-x)As$ sacrificial layer ($x \sim 0.8$). A layer of QDs is located in the middle of the membrane.

positioning of quantum dots in cavities. We worked with a quantum dot density of $\sim 100/\mu m^2$ which resulted in a few percent of the fabricated photonic crystal cavities to have coupled quantum dots.

1.4.2 CQED effects

There are several reasons why in optical networks for quantum information science the emitters need to be coupled to cavities. The cavity enhances the coupling of the emitter to very weak optical fields as those of single photons. At the same time the cavity enhances the interaction into some specific optical mode that can be well defined spatially.

To understand why it is important to work with cavities that have a high quality factor and a small volume, let's consider the interaction between a two level quantum system and electromagnetic field of some given energy. This is the case in the interaction between an optical emitter with a ground and excited state ($|g\rangle$ and $|e\rangle$), and the optical field of a single photon with energy hc/λ that is coupled into the cavity over

the timescale τ (λ is the wavelength of the photon, c the speed of light, h the Plank constant). From the interaction with the light field, the emitter transitions from $|g\rangle$ to $|e\rangle$, with a transition rate proportional to the $\Gamma_{|g\rangle\rightarrow|e\rangle} \propto |\vec{\mu}\cdot\vec{E}|^2$ and the transition probability is proportional to $1-e^{-\Gamma\tau}$. Here μ is the transition dipole moment and E is the electric field. Since μ is generally fixed, the transition probability can be enhanced by increasing E and τ, keeping in mind that $\int_{V_{mode}} \epsilon(\vec{r})|E(\vec{r})|^2 dV = hc/\lambda$, the total energy of the electromagnetic field, is fixed. Given this constraint, there are two ways one can increase the transition probability in a resonator. First, one can make the resonator with a higher quality factor Q such that the light escapes from the cavity at a slower rate, and thus the interaction time τ is longer. A longer interaction time also means that the field can accumulate in the cavity for longer, thus giving rise to higher values of E. Second, one can design resonators with smaller mode volume such that the electromagnetic field of a given energy is confined in a tighter space thus giving rise to stronger electric fields. Photonic crystal resonators are excellent candidates for CQED because both mode volumes smaller than one cubic optical wavelength and high quality factors can be achieved.

In a more formal description, the interaction between an emitter and the mode of a cavity is described by the coupling strength $g(\vec{r}) = g_0\psi(\vec{r})\cos(\xi)$, where $g_0 = \frac{\mu}{\hbar}\sqrt{\frac{\hbar\omega}{2\epsilon_M V}}$, $\psi(\vec{r}) = \frac{E(\vec{r})}{|E(\vec{r}_M)|}$, and $\cos(\xi) = \frac{\vec{\mu}\cdot\hat{e}}{\mu}$ [32]. $E(\vec{r})$ represents the electric field magnitude at position $\vec{r}$ and $V = \frac{\iiint \epsilon(\vec{r})|E(\vec{r})|^2 d^3\vec{r}}{\epsilon_M|E(\vec{r}_M)|^2}$ is the cavity mode volume where $\vec{r}_M$ is the point in the resonator with maximum energy density ($\epsilon(\vec{r})|E(\vec{r})|^2$) and $\epsilon(\vec{r})$ is the dielectric constant. For ideal alignment of the quantum dot, the maximum achievable coupling is g_0.

The coupling rate g is one of the important time-scales of the system. The other important timescales that set the dynamics of the system are κ (the cavity decay rate) and γ coupling of the dipole to modes other than the cavity, as shown schematically in Fig.1.8(a). Depending on the relative magnitude of these rates one can distinguish two regimes of operation: *strong coupling regime for* $g > \kappa, \gamma$, and *weak coupling* when $g < \kappa$ or $g < \gamma$. For InAs quantum dots coupled to photonic crystal cavities, the system parameters are such that $g, \kappa >> \gamma$ with $\gamma/2\pi \sim 0.1GHz$, so the strong coupling condition is set by the ratio of g and κ.

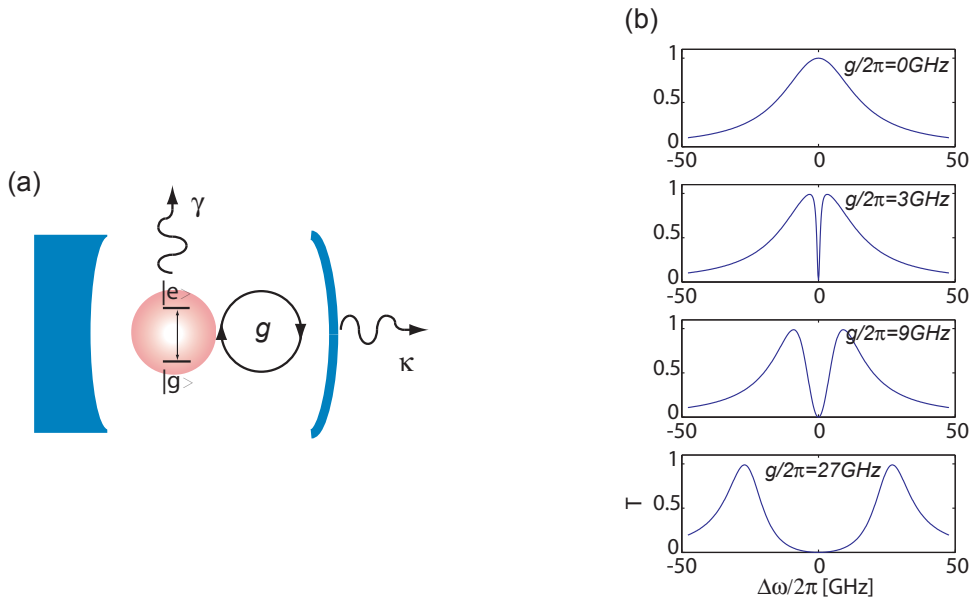

Figure 1.8: (a) Schematic representation of a one-sided optical cavity with a coupled optical dipole. The dipole couples to the cavity mode with rate g, the cavity field decay rate is κ and the spontaneous emission rate of the atom is γ. (b) Transmission (or reflectivity) spectra of a coupled cavity/quantum dot system ($\kappa/2\pi = 16GHz, \gamma/2\pi = 0.1GHz$) for different values of the coupling constant g. These spectra indicate that the transmission function of the cavity is significantly affected by the presence of the dipole even in the weak coupling regime ($g < \kappa/2$)

With ultra-small mode volume optical cavities, interesting CQED effects can be obtained both in the weak and strong coupling regime. In weak coupling, one of the main effects is the Purcell enhancement [33]. In strong coupling regime, the most interesting effects are the vacuum Rabi splitting and the dressed states. In both weak and strong coupling regime, the transmission function of the cavity is strongly affected by the presence of the dipole in the cavity, an effect also known as dipole induced transparency [34, 35].

The Purcell effect is the enhancement of the spontaneous emission rate of emitters weakly coupled to ultra-small mode volume resonators. When an emitter decays in a small mode volume resonator, the resonator traps the photon in a tightly confined

region and locally enhances the electric field. This field creates a positive feedback that further enhances the rate at which the photon is emitted. An alternative explanation is that the cavity enhances the density of optical modes that the emitter can decay to. As a function of the system parameters (index of refraction n, cavity wavelength λ_c, cavity linewidth $\Delta\lambda_c = \lambda_c/Q$, emitter wavelength λ, emitter dipole moment μ, position of the emitter $\vec{r}$, position of maximum field intensity $\vec{r}_M$, direction of the electric field at the position of the dipole $\hat{e}$), the spontaneous emission rate enhancement, or the Purcell factor is given by:

$$F = \frac{\Gamma}{\Gamma_0} = \frac{3}{4\pi^2}\frac{Q}{V}\left(\frac{\lambda}{n}\right)^3\left(\frac{E(\vec{r})}{E(\vec{r}_M)}\right)^2\left(\frac{\vec{\mu}\cdot\hat{e}}{\mu}\right)^2\frac{\Delta\lambda_c^2}{\Delta\lambda_c^2 + 4(\lambda-\lambda_c)^2} \tag{1.1}$$

The Purcell factor is maximized for a quantum dot that is resonant with the cavity, and with its dipole aligned with the maximum electric field vector in the cavity:

$$F = \frac{3}{4\pi^2}\frac{Q}{V}\left(\frac{\lambda}{n}\right)^3. \tag{1.2}$$

As can be observed from eq. 1.2, the Purcell factor increases linearly with the quality factor Q. However, one has to keep in mind that this formula is only valid in the weak coupling regime. If all the parameters of the system are kept constant and only Q is increased, the lifetime of the quantum dot decreases (F increases) and the cavity lifetime increases up to the point when these two lifetimes become equal. After passing this point, the system enters the strong coupling regime, where one can not talk anymore about a quantum dot lifetime and a cavity lifetime. In this regime the quantum dot coherently exchanges energy with the cavity mode, so the entire system is characterized by one lifetime, set by the quality factor, and the rate of coherent energy exchange also named Rabi frequency.

Quantum mechanically, a cavity - quantum dot coupled system is well described by the Jaynes-Cummings Hamiltonian, given by the formula:

$$H = \hbar\left[\omega_d\frac{\sigma_z}{2} + \omega_c a^\dagger a + g(a^\dagger\sigma_- + a\sigma_+)\right] \tag{1.3}$$

Here $\omega_{d,c}$ are the resonance frequencies of the dipole and the cavity, a and $a^\dagger$ are the

annihilation and creation operators for the cavity field, $\sigma_- = |g\rangle\langle e|$ and $\sigma_+ = |e\rangle\langle g|$ are the rising and lowering operators for the atom ($|g\rangle, |e\rangle$ are the ground and excited states of the atom) and $\sigma_z = |e\rangle\langle e| - |g\rangle\langle g|$ is the population operator. After adding damping from the cavity field decay rate (κ) and dipole free space decay rate γ, the eigenstates of this Hamiltonian are:

$$\omega_\pm = \frac{\omega_c + \omega_d}{2} - i\frac{\kappa + \gamma}{2} \pm \sqrt{g^2 + \frac{1}{4}\left(\delta - i(\kappa - \gamma)\right)^2}, \tag{1.4}$$

where $\delta = \omega_d - \omega_c$ is the QD/cavity detuning, and g is the vacuum Rabi splitting. For $\delta = 0$ and $\kappa >> \gamma$ the real part of the system eigenstates are degenerate for $g < \kappa/2$ (weak coupling regime) and non-degenerate with splitting $\sim 2g$ for $g > \kappa/2$ (strong coupling regime).

In the strong coupling regime, the presence of the dipole inside the cavity dramatically changes the spectrum of the system both in photoluminescence and transmission (Fig.1.8(b)). This enables excellent control of the cavity transmission by simply controlling the properties of the dipole coupled to it, with applications in optical signal processing and quantum information.

For the case of quantum dots coupled to nano and micro resonators, strong coupling is not required for the cavity transmission to be strongly affected by the dipole. Even in the weak coupling regime, the coherent interaction between the cavity, quantum dot and the transmitted laser field allows for almost complete destructive interference of the at the output port[34], as shown in Fig.1.8.

1.5 Outline of the Thesis

In this thesis I put together the work that my collaborators and I have done during my PhD on developing devices based on photonic crystals with coupled quantum dots. In Chapter 2 I discuss the techniques developed for local tuning of the resonance frequency for quantum dots and cavities. Due to substantial variations in the resonance of quantum dots and cavities, these techniques are essential for designing devices composed of multiple quantum dots and cavities. In Section 2.2 I describe

the laser heating technique that was key for enabling further coherent probing experiments on coupled quantum dots. The extension of this technique to devices where local heating is performed using micron-scale heaters is described in detail is Section 2.3. The remaining of the chapter is dedicated to two other techniques based on local control of the refractive index (Section 2.4) and electric field (Section 2.5).

- **Relevant publications for Chapter 2**
  - Andrei Faraon, Dirk Englund, Ilya Fushman, Nick Stoltz, Pierre Petroff and Jelena Vuckovic, Local Quantum Dot Tuning on Photonic Crystal Chips, Applied Physics Letters, Vol 90, article 213110 (2007).
  - Andrei Faraon, Dirk Englund, Douglas Bulla, Barry Luther-Davies, Benjamin J. Eggleton, Nick Stoltz, Pierre Petroff and Jelena Vuckovic, Local Tuning of Photonic Crystal Cavities Using Chalcogenide Glasses, Applied Physics Letters, Vol 92, article 043123 (2008)
  - Andrei Faraon and Jelena Vuckovic, Local temperature control of photonic crystal devices via micron-scale electrical heaters, Applied Physics Letters, vol. 95, page 043102, 2009.
  - Andrei Faraon, Arka Majumdar, Hyochul Kim, Pierre Petroff and Jelena Vuckovic, Fast Electrical Control of a Quantum Dot Strongly Coupled to a Nano-resonator, (arXiv:0906.0751)

In Chapter 3 I focus on the coherent probing experiments on photonic crystal cavities with coupled quantum dots. Section 3.2 describes the first experiments done on measuring the transmission function of photonic crystal cavities with strongly coupled quantum dots. Then in Section 3.3 I show how we used a strongly coupled system for coherent generation of non-classical states of light on a chip via photon blockade and photon-induced tunneling.

- **Relevant publications for Chapter 3**
  - (1-3 Equal contributors) Dirk Englund, Andrei Faraon, Ilya Fushman, Nick Stoltz, Pierre Petroff and Jelena Vuckovic, Controlling Cavity Reflectivity

With a Single Quantum Dot, Nature, vol. 450, number 7171, pp. 857-861 (2007)

- (1-3 Equal contributors) Ilya Fushman, Dirk Englund, Andrei Faraon, Nick Stoltz, Pierre Petroff and Jelena Vuckovic, Controlled Phase Shifts with a Single Quantum Dot, Science, vol. 320, number 5877, pp. 769-772 (2008).
- (1-3 Equal contributors) Andrei Faraon, Ilya Fushman, Dirk Englund, Nick Stoltz, Pierre Petroff and Jelena Vuckovic, Coherent generation of nonclassical light on a chip via photon-induced tunneling and blockade, Nature Physics, 4, 859 - 863 (2008)
- Dirk Englund, Arka Majumdar, Andrei Faraon, Mitsuru Toishi, Nick Stoltz, Pierre Petroff and Jelena Vuckovic, Coherent excitation of a strongly coupled quantum dot-cavity system, (arXiv:0902.2428)

After discussing local tuning techniques and coherent probing, in Chapter 4 I describe some experiments where all these techniques are combined together into developing integrated devices composed of cavities with quantum dots, waveguides, tuning and outcoupling elements. Coherent probing is demonstrated in these devices, thus opening the possibility for on chip optical signal processing devices where the flow of light is controlled down to the single photon level (Section 4.3).

- **Relevant publications for Chapter 4**

  - Andrei Faraon, Dirk Englund, Ilya Fushman, Edo Waks and Jelena Vuckovic, Efficient photonic crystal cavity-waveguide couplers , Applied Physics Letters, vol. 90, article 073102 (2007)
  - Andrei Faraon, Ilya Fushman, Dirk Englund, Nick Stoltz, Pierre Petroff and Jelena Vuckovic, Dipole induced transparency in waveguide coupled photonic crystal cavities, Optics Express, Vol 16, pp 12154-12162 (2008)
  - Dirk Englund, Andrei Faraon, Bingyang Zhang, Yoshihisa Yamamoto and Jelena Vuckovic, Generation and Transfer of Single Photons on a Photonic Crystal Chip, Optics Express, Vol. 15, pp. 5550-5558 (2007)

In Chapter 5 I discuss experiments that integrate strongly coupled quantum dots and local electrical control. These experiments demonstrate that CQED devices can be used in opto-electronics for developing electro-optic switches that operate at ultra-low power levels.

- **Relevant publications for Chapter 5**
  - Andrei Faraon, Arka Majumdar, Hyochul Kim, Pierre Petroff and Jelena Vuckovic, Fast Electrical Control of a Quantum Dot Strongly Coupled to a Nano-resonator, (arXiv:0906.0751)

Chapter 2

Local tuning techniques

2.1 Introduction

Solid state optical emitters are promising candidates for future nano-scale quantum networks where the interaction is mediated via photons. However, unlike atoms and molecules, these emitters are characterized by large inhomogeneous broadening. In particular, for InAs/GaAs self assembled quantum dots, the inhomogeneous broadening is caused by the randomness in the growth process. Since QDs are formed as self-assembled islands of InAs on top of a GaAs surface, the QD size and shape are parameters hard to control, which results in QDs having different confining potentials and thus different wavelengths. In Fig.1.6 we show a typical spectrum of an ensemble of InAs QDs under weak excitation such that only the single excitons lines are emitting. It can be observed that the emission wavelengths span an interval of $\sim 30nm$ with most QDs around 935nm.

The QD inhomogeneous broadening is one of the major drawbacks in designing complex systems that combine multiple emitters in photonic crystals. The other major drawback is the random spatial distribution. During the growth process, the QDs self assemble at random locations on the GaAs surface. This imposes difficulties when combining them with nanophotonic devices where the QDs need to be located at specific locations. Spatial alignment can be achieved either by positioning the PC cavity on an already identified QD [30, 36], or by relying on chance. For spectral alignment,

there are a few techniques that can be used to modify the emission wavelength of InAs QDs: DC Stark shift [37], Zeeman shift [38], temperature tuning [39] and strain tuning [40]. Most of these techniques have been used to tune all the QDs on the chip at once.

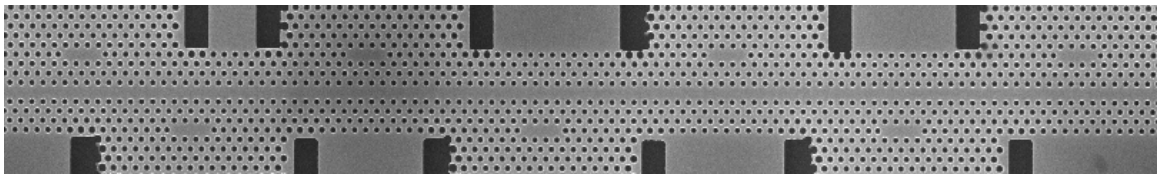

Figure 2.1: Network of multiple photonic crystal cavities connected via a photonic crystal waveguide.

In this chapter, I discuss our effort on spectral tuning of cavities and QDs. Since the long term goal is to make devices composed of QDs embedded in multiple interconnected cavities as those showed in Fig.2.1, we focused on techniques that allow local tuning. By local I mean the capability of tuning one QD or cavity without affecting the other QDs and cavities on the chip. We have developed four different techniques that allow for local tuning. In section 2.2 I discuss our technique to locally control the temperature on the chip using an external laser beam. In section 2.3 we extend the technique by implementing electrical control instead of optical. In section 2.4 I present another method that relies on locally tuning the refractive index using photo-refractive materials. An electrical method that enables the control of the resonance of a QD in a nanocavity via the DC Stark shift is presented in section 2.5 and in chapter 5.

2.2 Local temperature tuning by laser heating

As described in section 1.3, the quantum dot confining potential is created by the difference in bandgap between GaAs and InAs. Since both bandgaps depend on temperature, so do the QD transitions, thus implying that temperature can be used to spectrally tune the QDs. Temperature tuning is routinely used to tune QDs in and out of resonance with optical resonators. In this section I discuss our local

implementation of this technique. The technique we demonstrated can be used for in-situ tuning of QDs by up to $1.4nm$ without significant deterioration in the QD emission. This method works locally and reversibly, making it a useful tool for a range of solid state studies, from local thermometry to quantum information science. In particular, the method is compatible with photonic crystal structures and forms a crucial step toward building an on-chip quantum network involving resonant QDs.

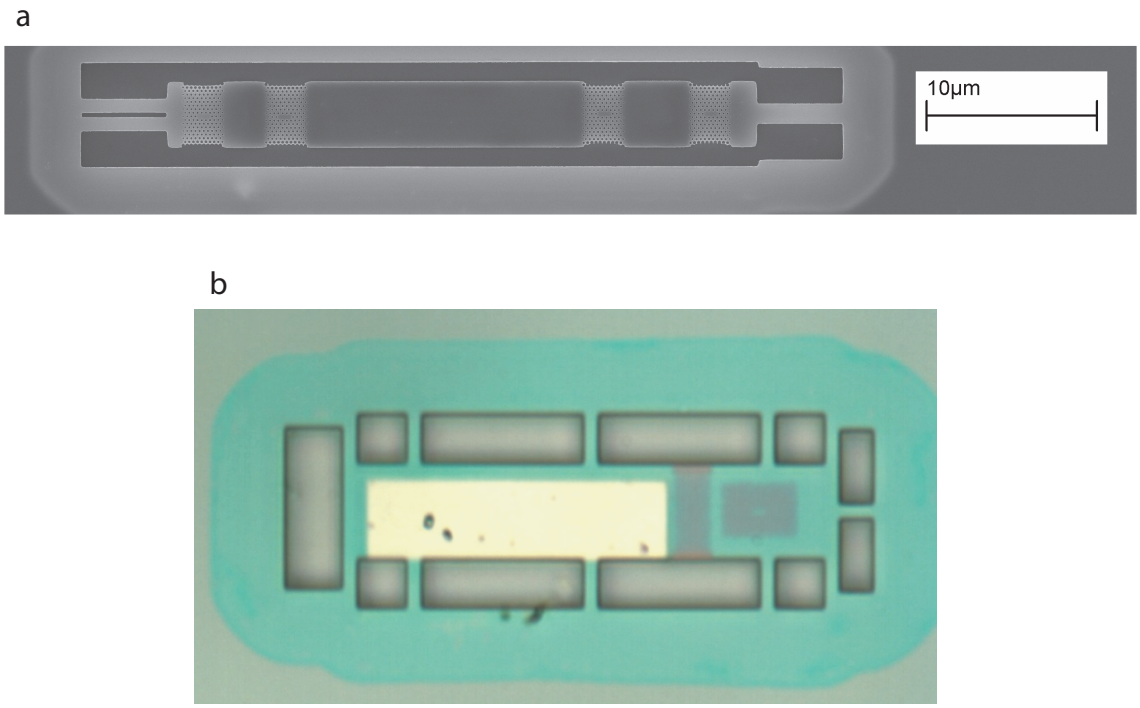

Figure 2.2: (a) Long suspended bridge used in the initial experiments on local quantum dot tuning. (b) First successful design for where local temperature tuning was implemented (optical image). The silver rectangle is the metal pad deposited on the device, the blue area shows the undercut. The photonic crystal cavity is located on the right side of the device.

The basic idea is to use a laser beam to locally change the temperature of the QD of interest without significantly affecting the other quantum dots on the chip. One difficulty in developing this technique is imposed by the large thermal conductivity

of GaAs. In order to achieve significant temperature increase on a specific are of the chip, that area must be thermally insulated. Another thing to keep in mind when designing the device is that the laser inducing the heating must not interfere with other measurements done with the quantum dot of interest. Ideally, the frequency of the heating laser should be below the quantum dot transition frequency.

We went through several iterations until a successful design was developed. The first experiments were done on chip A32 with long suspended bridges as shown in Fig.2.2(a). The suspended design was chosen in order to improve the thermal insulation of the device. A heating laser tuned above the band gap of GaAs was focused on one end of the bridge and quantum dots on the other end of the bridge were monitored. These devices were not so successful because the bridges were sagging and touching the GaAs substrate underneath, and thus destroying the thermal insulation. Then we switched to a different design (chip T1) where the structures were shorter, more connecting bridges were supporting the device, and a metal pad was deposited next to the photonic crystal cavity (Fig.2.2(b)). The metal pad enhances the absorption of laser beams tuned below the emission frequency of the quantum dots. Local temperature tuning was achieved with this type of device, but we went even further and designed a more compact device as shown in Fig.2.3.

The device in Fig.2.3 was fabricated on chip A53. An SEM image of the entire chip is shown in Fig.2.4. On this device there were 32 good structures that were used for five breakthrough experiments: Englund et. al. Nature 450 ,857-861 (2007); Fushman et. al. Science 320 769-772 (2008), Faraon et. al. Nature Physics, 4, 859-863, (2008); Faraon et. al., Applied Physics Letters, 90, 213110 (2008); Faraon et. al., Optics Express, 16, 12154-12162, (2008).

The fabricated structures (12 μm long, 4 μm wide, 150 nm thick) consist of a PC cavity and a heating pad (Fig.2.3). To provide the thermal insulation needed for efficient device heating, the structure was connected to the rest of the chip by only six narrow bridges. The thermal conductivity of narrow ($\approx 100nm$), cold (4K - 10K) GaAs bridges is reduced by up to four orders of magnitude with respect to the bulk GaAs [41], thus improving the thermal insulation. We tested two devices with connection bridges of the same length (2 μm) but different widths: $w = 320nm$

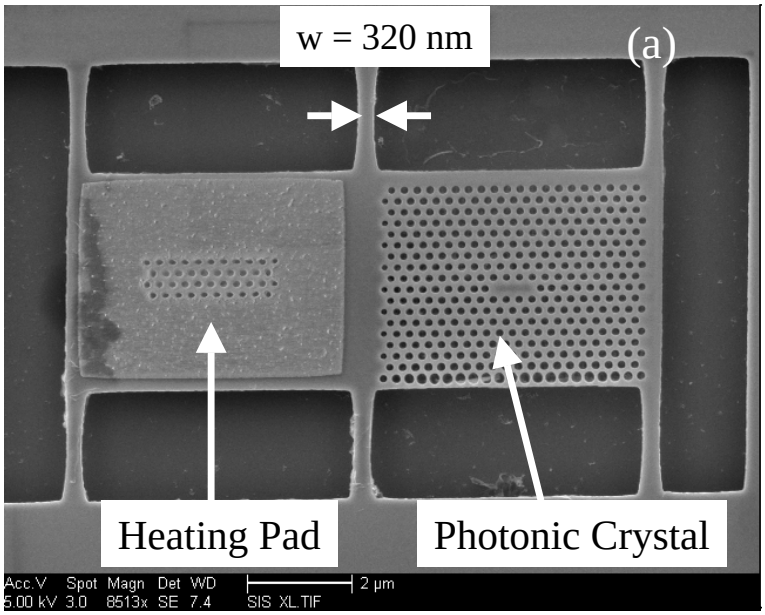

Figure 2.3: Scanning electron microscope image of the fabricated structure showing the PC cavity, the heating pad and the connection bridges. The temperature of the structure was controlled with a laser beam (at 960 nm wavelength, below the GaAs bandgap and QD transition energy) focused on the heating pad.

and $w = 800nm$. The temperature of the device was controlled by using a focused laser beam to heat up the pad next to the photonic crystal cavity. A schematic of the experimental setup is shown in Fig.2.5. To minimize background photoluminescence in single quantum dot measurements, the heating laser is tuned below the QD absorption frequency. A metal layer (20 nm Cr/15 nm Au) was deposited on the heating pad to increase heat absorption. The thermal conductivity of GaAs beams with cross sections on the order of $100nm/100nm$, and the absorption coefficient of the metal layer are not well known. As measured by Fon et. al [41], the thermal conductivity of GaAs beams with dimensions $100nm/200nm/6\mu m$ is about $3 \times 10^{-2} WK^{-1}cm^{-1}$ at $10K$, three orders of magnitude lower than the bulk value. Because of the size similarity, we assume that the connection bridges from our device have a similar thermal conductivity. Assuming that $10^{-2}mW$ of heat is absorbed in the heating pad and considering that the device has the same thermal conductivity as the bridges, we

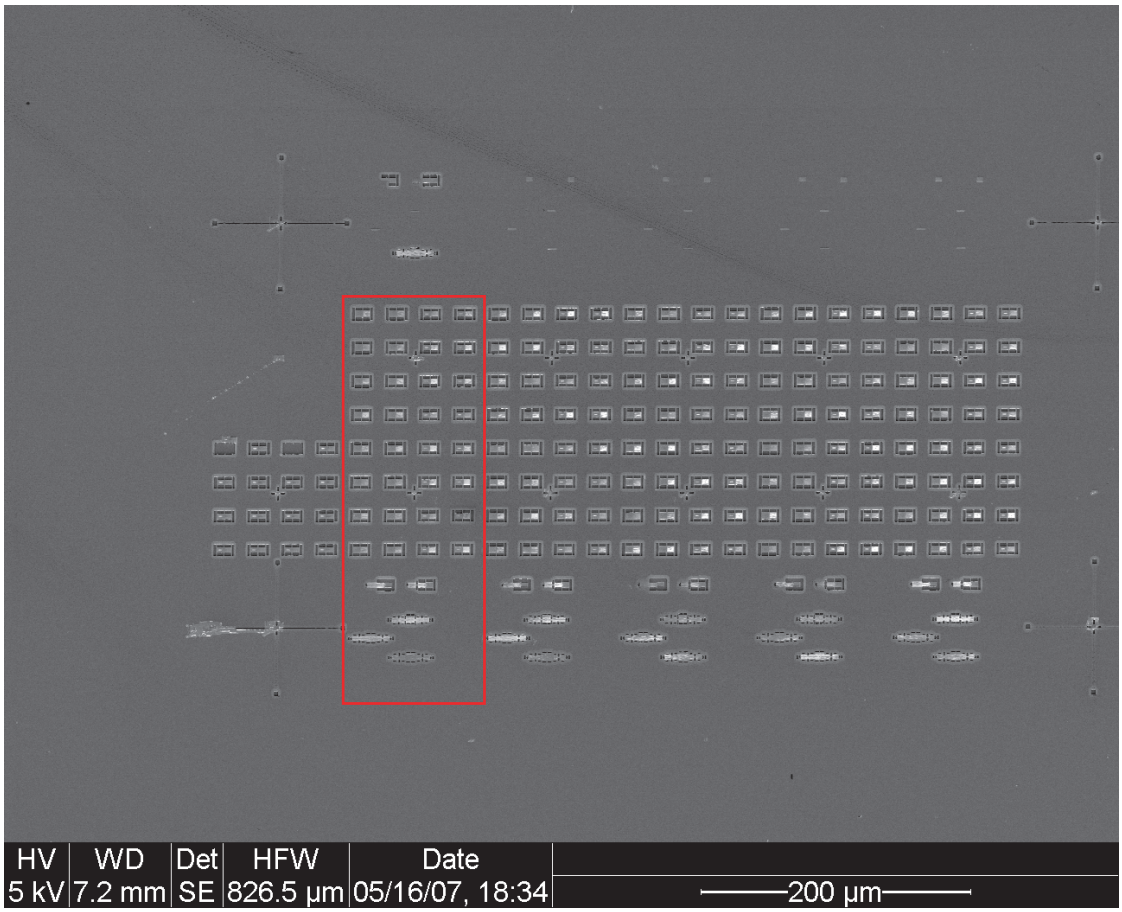

Figure 2.4: SEM image of the A53 chip. The red rectangle marks the structures that were used for several experiments that were published in Nature, Science or Nature Physics

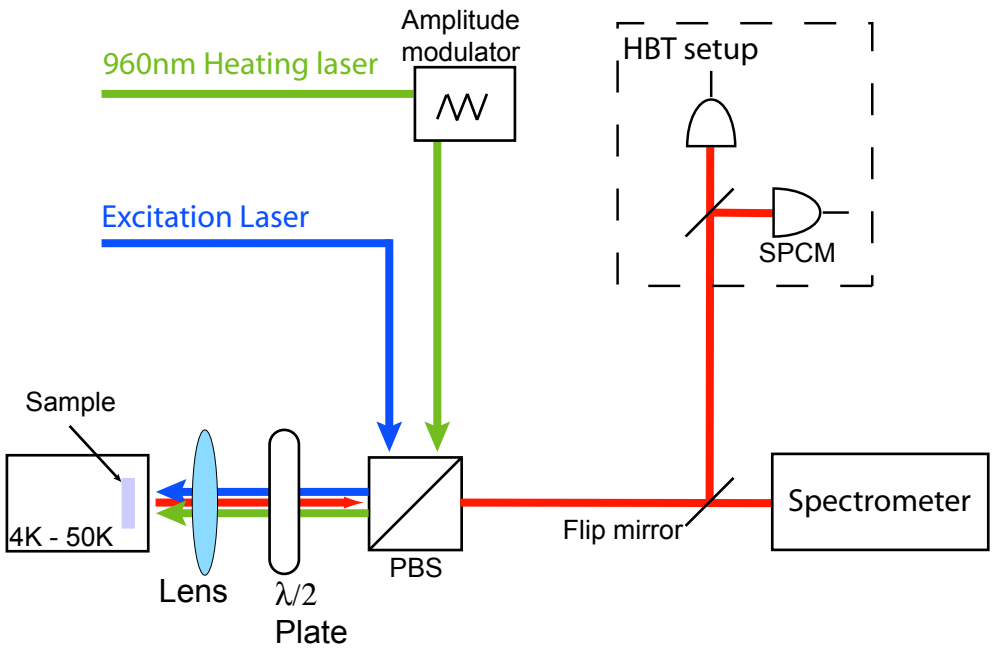

Figure 2.5: Schematic representation of the experimental setup used for local temperature tuning experiments. The HBT setup is composed of a beam-splitter and two single photon counters (SPCMs) connected to a picosecond time analyzer.

expect the temperature of the membrane to increase by a few tens of Kelvins.

The local quantum dot tuning measurements were performed in a continuous flow liquid helium cryostat maintained at 10K. A Ti:Saph laser tuned at 855 nm was used to excite the quantum dots while a 960 nm laser diode acted as the heating laser. Using a pinhole we collected photoluminescence(PL) from a quantum dot located inside the photonic crystal slab. By increasing the power of the heating laser, QD emission was observed to redshift (Fig.2.6 (a)). The QD line-width broadens with increasing heating pump power, as expected from experiments where the full sample is heated. We were able to tune the quantum dot by 1.4 nm while the linewidth broadened from $0.04nm$ to $0.08nm$. The quantum dot could be further shifted by 1.8 nm but the PL intensity dropped rapidly. For quantum information processing, it is

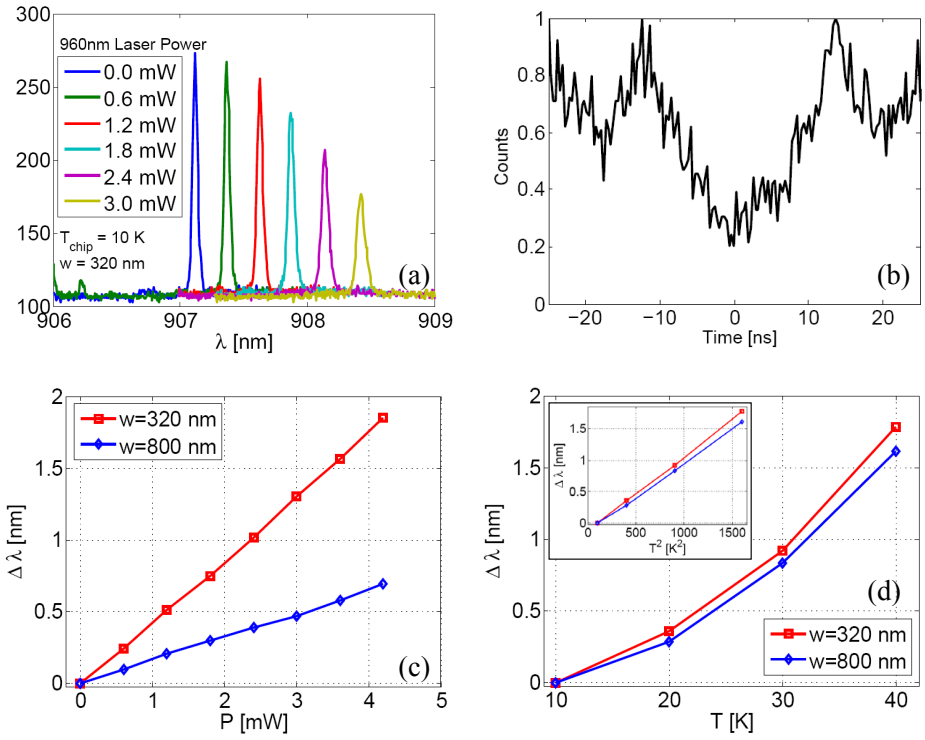

Figure 2.6: (a) Quantum dot tuning vs. heating laser pump power. The structure is connected to the substrate by bridges measuring 320nm in width (Fig. 2.3). The quantum dot emission shifts by 1.4 nm while increasing the heating laser power to 3 mW. Only a small fraction of the heating laser power is absorbed in the metal pad. (b) Autocorrelation measurement showing single photon anti-bunching while the QD was detuned by 0.8 nm using the local tuning technique. (c) Dependence of the QD detuning on the heating laser power. The two data sets correspond to structures with different thermal contact to the substrate (320nm and 800nm bridges). (d) QD temperature tuning by changing the temperature of the entire chip by heating the cryostat. The inset shows that the detuning is linear in T^2.

essential to show the compatibility of this local tuning technique with measurements of the second order correlation function for single photon fields. The normalized second order correlation function is defined as [42]:

$$g^{(2)}(\tau) = \frac{\left\langle a^\dagger(t)a^\dagger(t+\tau)a(t+\tau)a(t)\right\rangle}{\left\langle a^\dagger a\right\rangle^2}, \tag{2.1}$$

where $a^\dagger$ and a are the creation and annihilation operators. For single photon fields, the second order correlation function is null for $\tau = 0$. The second order correlation is generally measured using a Hanbury-Brown and Twiss (HBT) setup composed of a beam splitter and two detectors. The electromagnetic field is incident on the beam splitter and then sent to two single photon counters (SPCMs). The time difference between the clicks registered by the SPCMs is recored in a histogram that resembles the second order correlation function in the limit that the SPCMs have low detection efficiency.

We proved anti-bunched single photon emission from an exciton transition using a HBT interferometer while the emission line was shifted by $0.8nm$ (Fig.2.6 (b)). Antibunching can be measured as long as the thermal energy is not larger than the confining energy of the QD, which in our case corresponds to a detuning of $\approx 1.4nm$.

To investigate the thermal properties of the fabricated devices, we compared the shift of quantum dots located on structures with different bridge widths, $w = 320nm$ and $w = 800nm$. The thermal conductance of the bridges is proportional to their width w. Under the same pump conditions the temperature of the structure is inversely proportional to w so we would expect the QD to shift 2.5 (i.e. 800/320) times further for the structure with thinner bridges. The QD shift observed on the two structures is plotted in Fig.2.6 (c). For the same pump power, the QD shifts 2.65 times further for $w = 320nm$ than for $w = 800nm$, in good agreement with the expected result.

The temperature dependence of the QD shift was determined by changing the temperature of the entire chip by heating the cryostat. The results are plotted in a Fig.2.6 (d) and indicate that a shift of 1.8 nm corresponds to a temperature of 40 K. This implies that during the local temperature tuning experiment the structure was

also heated up to 40 K. The QD shift shows a quadratic dependence with temperature (Fig.2.6 (d) inset), which is expected since the band gaps of GaAs/InAs have a quadratic temperature dependence in this temperature interval [43]. Our experimental data shows a linear dependence of the QD shift with the heating laser power (Fig.2.6(c)), which implies a linear relation between the power of the heating laser and T^2. The local temperature gradient also induces strain which can be responsible for shifting the QD emission. To release the strain in the suspended membrane, we used a focused laser beam to cut some of the connection bridges next to the QD. After the strain release we still observed the same shift of the QD with the heating power which indicates that the shift is mainly due to temperature.

Not only the QDs but also the PC cavities shift their resonant frequency with temperature. The local heating technique was used to shift a PC cavity located on the $w = 320nm$ structure. Using the same heating power as for the QD tuning, we observed the cavity resonance red shift by up to 0.48 nm (Fig. 2.7 (a) and (b)), about 3 times less than the QD shift. The quality factor of the cavity dropped from 7600 to 4900 at the maximum shift. Beside temperature tuning, photonic crystal cavities can be tuned using chemical digital etching [44] or by deposition of molecular layers on top of the PC membrane [45] .

A problem of immediate concern in cavity-QED experiments is spectral tuning of the QD onto the cavity resonance. We used our technique to locally tune a QD into resonance with a PC cavity mode with $Q = 10000$, as shown in Fig. 2.8(a). For low excitation powers, the QD PL increases linearly with pump power, indicating a single exciton line. As the QD is temperature-tuned through the cavity, clear anticrossing between the QD and the cavity lines is observed: the QD splits the cavity spectrum into two polariton peaks (with frequencies $\omega_{\pm}$) when it becomes resonant with the cavity, as shown in Fig.2.8(a-b). A polariton splitting of 0.05nm is observed. This splitting is described by

$$\omega_{\pm} = \frac{\omega_c + \omega_d}{2} - i\frac{\kappa + \gamma}{2} \pm \sqrt{g^2 + \frac{1}{4}\left(\delta - i(\kappa - \gamma)\right)^2}, \tag{2.2}$$

where ω_c denotes the cavity frequency, ω_d the QD frequency, $\delta = \omega_d - \omega_c$ the

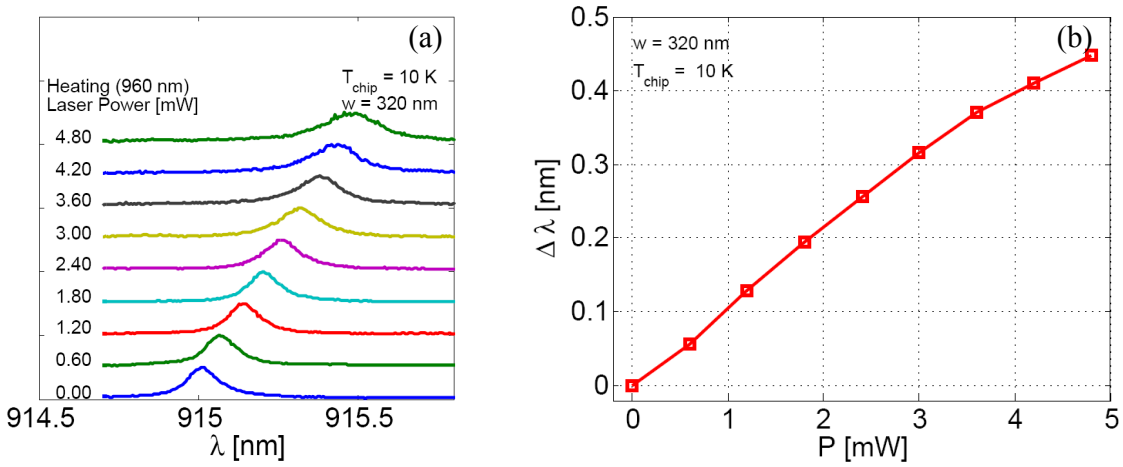

Figure 2.7: (a) Detuning of the PC cavity resonance with increasing temperature due to local heating. (b) Dependence of the PC cavity resonance wavelength on the local heating power.

QD/cavity detuning, cavity field decay rate $\kappa/2\pi = 16$ GHz (cavity linewidth 0.1 nm), Rabi frequency $g/2\pi = 8$ GHz (from Rabi splitting of $2g$ corresponding to 0.05nm), and the dipole decay rate without the cavity $\gamma/2\pi \approx 0.1$ GHz. As $g \approx \kappa/2$, the cavity/QD system operates at the onset of strong coupling, as was also the case for other QD-PC cavity QED experiments done in photoluminescence[46, 36].

The proof of concept experiment presented in our paper shows the local tuning of PC cavities and QDs that are not integrated into a PC circuit. However, it is only a matter of design to build PC circuits with integrated local heaters that could enable the independent tuning of different components of the same circuit. Moreover, this technique can be slightly modified by changing the heating method from optical to electrical by connecting electrical wires to the metal pads, as shown in this chapter.

Our local temperature tuning technique is completely reversible and does not affect the structure of the PC cavities or the QDs. Another tuning technique that relies on locally heating microcavities to permanently change the structure of the resonator and the QDs has been reported by Rastelli et. al. [47].

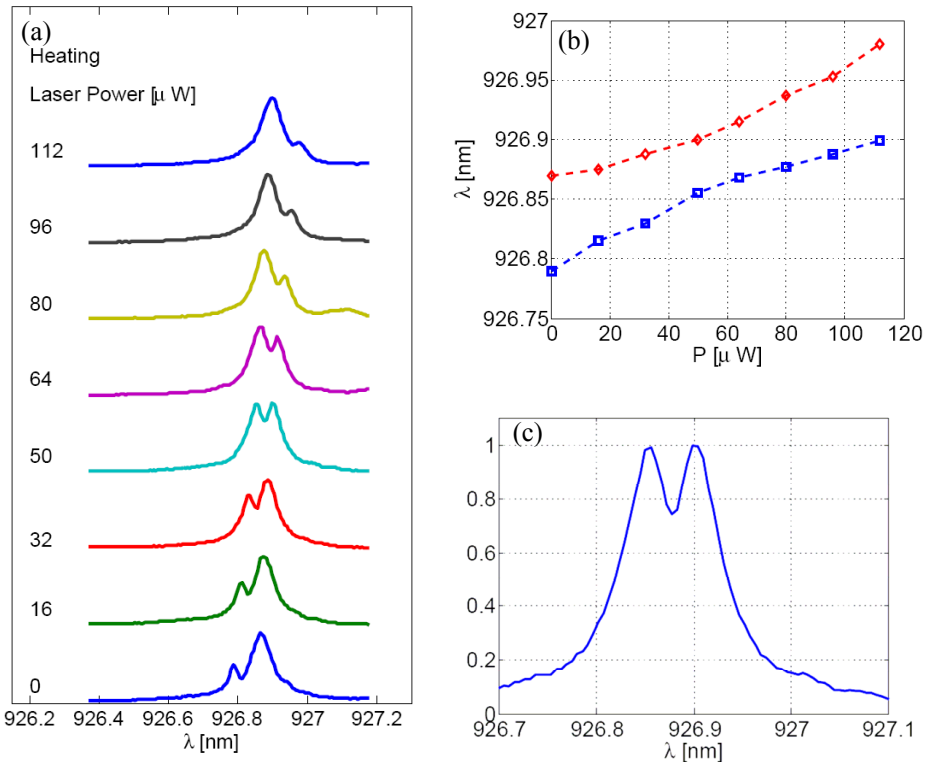

Figure 2.8: (a) Spectra showing the tuning of a single QD into strong coupling with the cavity mode using the local heating technique. (b) Anticrossing between the polariton lines of the strongly coupled PC cavity - QD system. (c) Spectrum showing the 0.05 nm splitting of the polaritons.

2.3 Local temperature tuning via nanoscale electrical heaters

The local local temperature technique using laser heating[48] presented in section 2.2 is very reliable when one needs to tune only a couple of devices. However, for tuning large ensembles of devices it is experimentally challenging to position and control a large number of tuning laser beams. One way to overcome this problem is to perform the temperature control using electrical heaters. This is also useful for experiments where the heating laser interferes with the desired measurement.

To integrate local heaters with the QD/photonic crystal structures, we designed

the device shown in Fig.2.9. The concept of the device is similar to the one in Fig.2.3, but instead of the heating pad, there is a serpentine electrical heater (20nm Cr/15nm Au). I experimented with several designs, some of them are shown in Fig.2.10. For this experiment, I only used one pair of electrical connections to control all the devices on the chip at once. An optical microscope image showing how the structures are connected is shown in Fig.2.11.

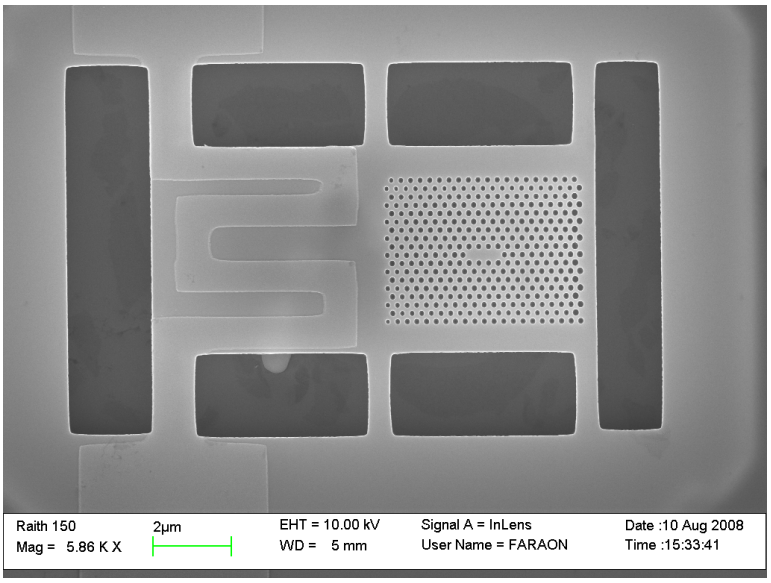

Figure 2.9: Suspended photonic crystal cavity integrated with an Ohmic heater.

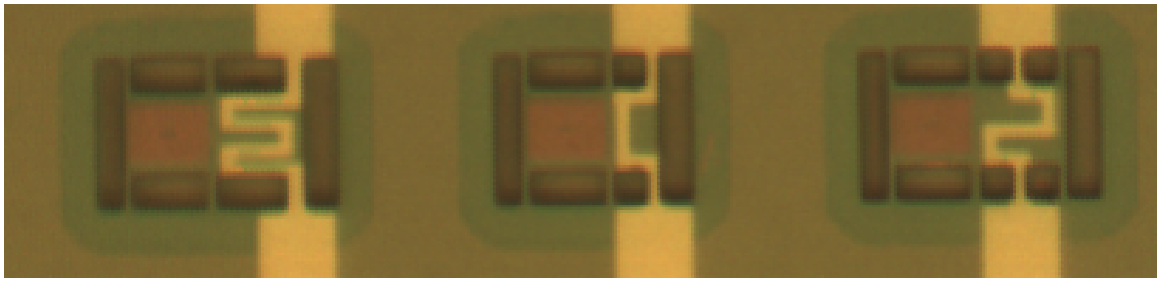

Figure 2.10: Optical microscope image showing several types of designs for the Ohmic heaters.

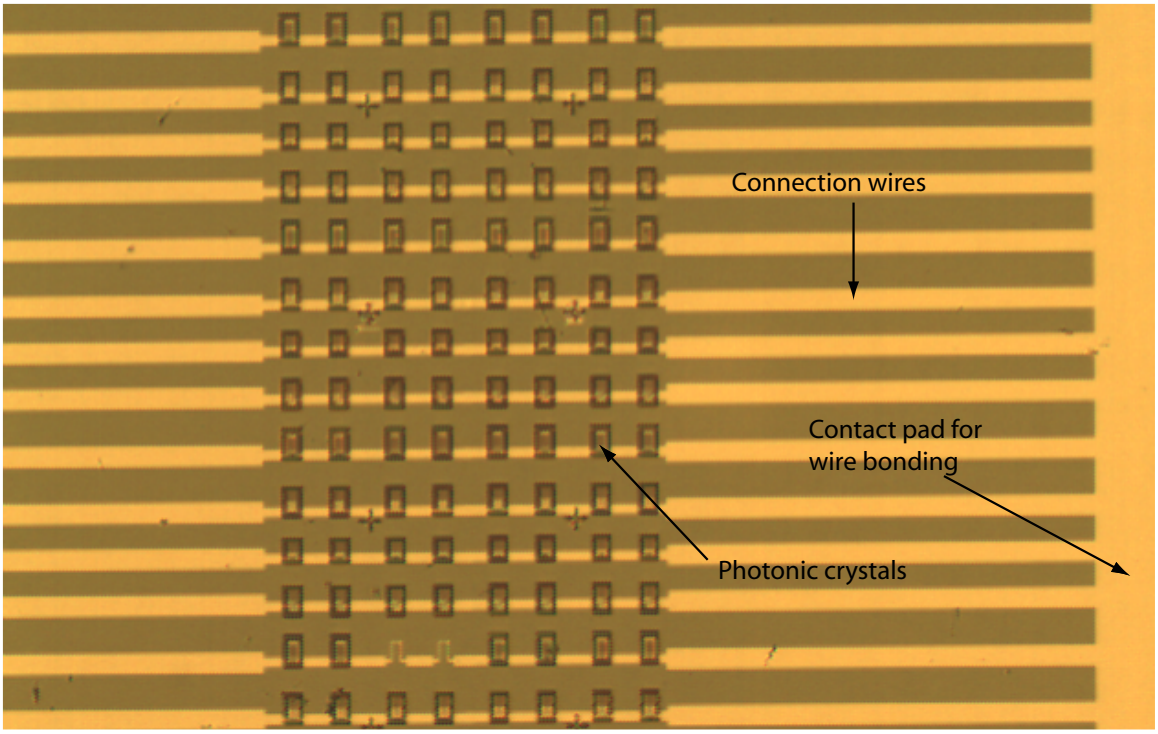

Figure 2.11: Optical microscope image showing how the devices are connected on the chip.

To test the performance of the device, the chip was connected to a power supply and then cooled down into a He flow cryostat. In Fig.2.12, the electrical local tuning technique is used to tune a QD into strong coupling with the mode of a photonic crystal resonator. To obtain the tuning range indicated in Fig.2.12, the voltage was changed from 0V to 1.2V. The shift of the cavity and the quantum dot frequency have a linear dependence on the heating power dissipated in the structure, which corresponds to a quadratic dependence on the voltage, as shown in Fig.2.12.

To test the speed of this tuning technique, a 0-2V square wave was applied and the photoluminescence spectrum of a cavity was monitored on a spectrometer with an integration time much larger than the period of the driving voltage. In case the thermal relaxation time of the device is much shorter than the period of the driving voltage, two spectral lines can be observed on the spectrometer, corresponding to 0V

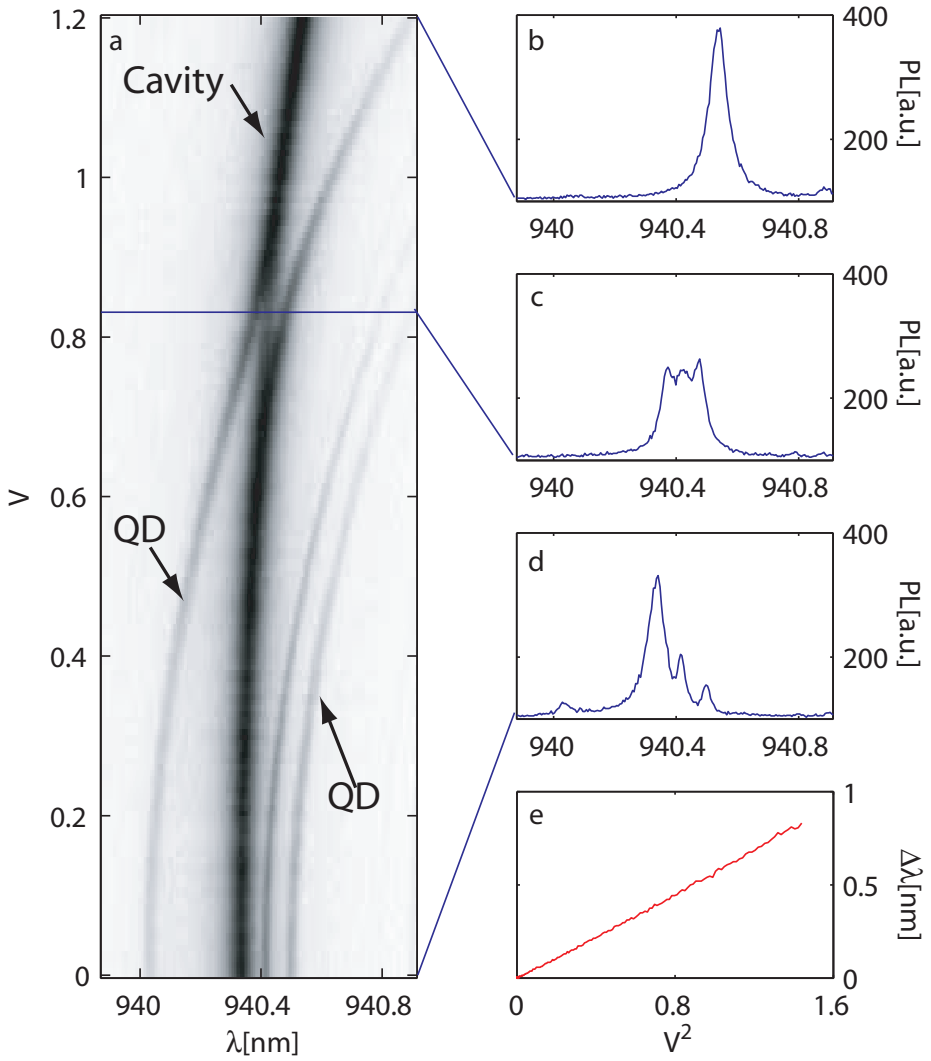

Figure 2.12: (a-d) Quantum dot and cavity tuning performed by controlling the temperature of the device using local electrical heating. Anti-crossing, is observed as the quantum dot is tuned into resonance with the cavity, a signature of the strong coupling regime. (e) Linear dependence of the shift in the quantum dot frequency with the square of the applied voltage.

and 2V. As the frequency of the driving voltage becomes greater than the thermal relaxation rate, only one spectral line, corresponding to the average power dissipated in the structure, will be observed on the spectrum. The experimental data in Fig.2.13 shows the spectrum of the cavity as the frequency is increased from 10Hz to 1MHz. The two spectral line merge into a single spectral line for frequencies of a few hundred kHz, which corresponds to the thermal relaxation rate of the device.

This proof of concept experiment shows that local temperature tuning can be implemented electrically, thus enabling the tuning into resonance of large ensembles of resonators. The technique is not only limited to solid state quantum networks but it can be extended to any optical chips. It is particularly useful in optical interconnects chips where large ensembles of optical resonators can be tuned to exact frequencies.

2.4 Local tuning of photonic crystal cavities using chalcogenide glasses

Local temperature tuning is a powerful and versatile technology that enabled a lot of progress in the coherent study of quantum dot and cavities on photonic crystal chip. However, in the context of tuning quantum dots and cavities in on-chip quantum networks, it does not provide enough control. Since both the cavities and the QDs are sensitive to temperature, the technique does not allow for independent control of the QD and cavity resonance. Moreover, due to fluctuations in the fabrication process, the resonances of cavities fabricated identically on the same chip are not the same. This motivated us to look for another local tuning technique that would allow us to adjust the cavity and quantum dot resonance frequency.

In this section I talk about our method to locally change the refractive index in planar optical devices by photo-darkening of a thin chalcogenide glass layer deposited on top of the device. The method is used to tune the resonance of GaAs-based photonic crystal cavities by up to 3 nm at operating wavelength of 940 nm. This method is not limited to photonic crystal devices for quantum information science, but it has broad applications for post-production tuning of photonic devices. Chalcogenide

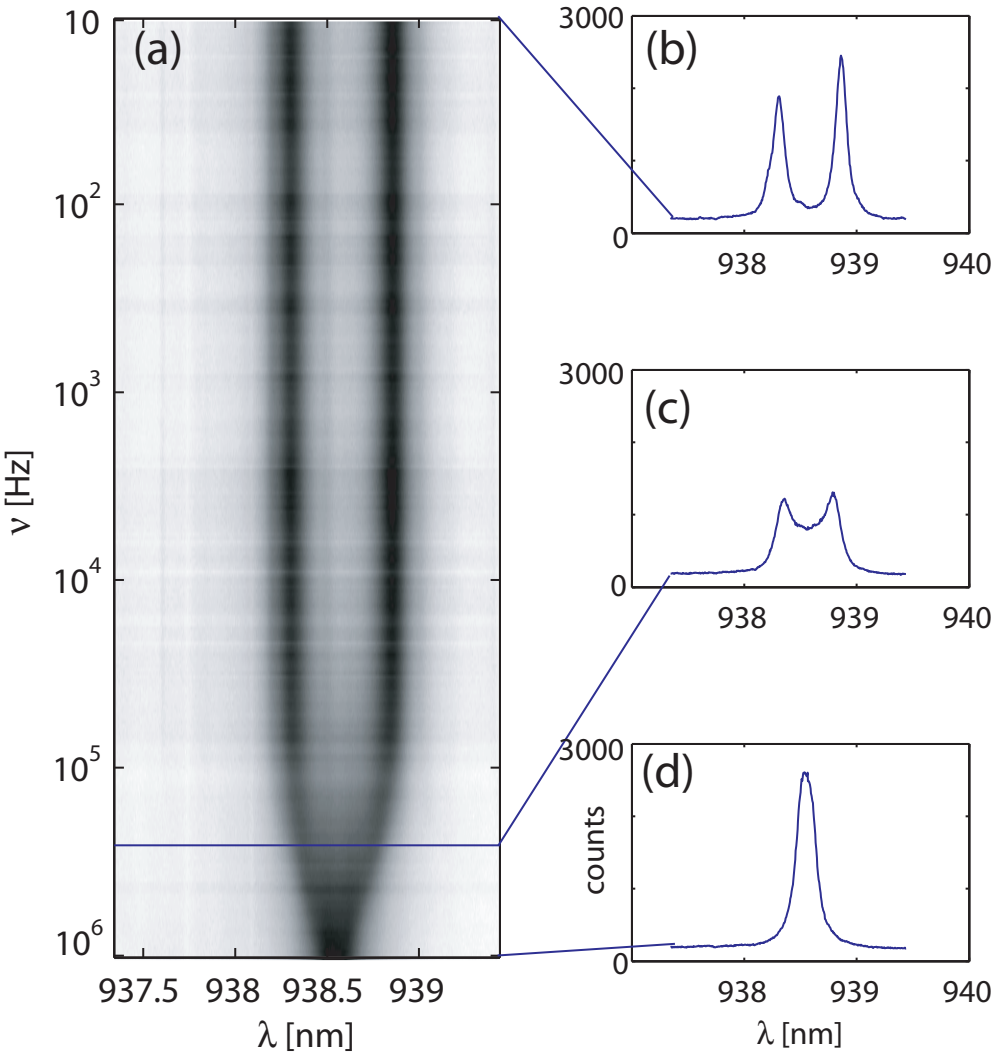

Figure 2.13: Dependence of the cavity spectrum as the frequency of the 0-2V driving voltage is changed from 10Hz to 1MHz.

glasses change their optical properties when illuminated with light above their band gap, and have been used to tune optical devices such as quantum cascade lasers[49]. The tuning of PCs devices directly fabricated in chalcogenide glasses has already been shown in Ref.[50].

In our approach, a photosensitive chalcogenide glass layer (arsenic trisulfide As_2S_3) is deposited on prefabricated GaAs/InAs devices. Linear three-hole defect PC cavities were first fabricated in a 150 nm thick GaAs membrane containing a central layer of InAs QDs. Arsenic trisulphide films with thickness between 30 nm and 100 nm were deposited onto the photonic crystals using thermal evaporation from a temperature controlled baffled boat in a chamber pumped to a base pressure of 3×10^{-7} torr. The deposition geometry was chosen to ensure that the flux of material struck the sample close to normal incidence to prevent coating the inside of the holes. To improve film adhesion the sample surfaces were cleaned using 50 eV Ar ions prior to deposition.

The deposition of arsenic trisulphide was done in the group of Prof. Barry Luther Davies at Australian National University in Canberra. We sent them samples with prefabricated photonic crystals and they did the deposition of chalcogenide glass using thermal evaporation. In total, we sent them 5 chips, for deposition. We started with A48 and A49, where the thickness of the As_2S_3 was 100nm, but the quality factor of the cavity degraded considerably. Then we experimented with 60nm and 30nm on chips A56 and A60 respectively. We also tested with 50nm on chip A58. The most promising results were obtained on A56, A60 and A58, and they were reported in Ref.[51].

Thermal evaporation results in films with substantially different bond structure from the bulk glass. The films have been found to contain disconnected molecular cage-like structures[52] that form in the vapor phase and are then frozen into the deposited film. These cage-like structures are, however, meta-stable and can"open" with optical excitation near the band edge or by heating that allows re-bonding to occur which results in polymerization of a more extended glass network. This re-bonding process is accompanied by an increase in the refractive index and a small decrease of the material volume[53]. This change is permanent unless the glass is annealed above the glass transition temperature which can potentially reset the initial

refractive index[49]. The thermally evaporated films had an index (at 1550 nm) of ~ 2.31 compared with the bulk glass whose index is 2.43. After deposition the films were partially polymerized by annealing at 130°C for 24 hours prior to use which increased the refractive index to ~ 2.38. Subsequent irradiation of the films with actinic light at high fluence can increase the film index to the bulk value.

The experiment was performed at cryogenic temperature (less than $\sim 60K$) to obtain luminescence from the embedded InAs quantum dots, as needed for quantum information processing applications. This illustrates that the method works at low temperatures, though we stress that it is applicable to room temperature nanophotonic circuits. The sample was placed inside a continuous-flow liquid helium cryostat at 10K and the QD photoluminescence was used to measure the cavity resonance. A confocal microscope setup and a laser tuned to 780 nm excited quantum dot luminescence while a spectrometer monitored the signal. A 543 nm HeNe laser ($1\mu W$) focused to $\sim 1\mu m^2$ spot through the same confocal setup was used for photodarkening of the As_2S_3 layer (Fig.2.14). This wavelength was chosen because it is close to the 527 nm bandgap of As_2S_3.

The thickness of the As_2S_3 influences both the quality factor of the cavity and the maximum tuning range. For this reason we experimented with three different thicknesses: 30, 60 and 100 nm (samples S30 (chip A60), S60 (chip A56) and S100 (chips A48 and A49)). For each sample, the spectra of the cavities were recorded before and after the deposition of the chalcogenide layer. For samples S60(S30), the deposition caused the quality factor to degrade by $\sim 5\%(30\%)$ from an average value of $\sim 8500(10000)$ while the resonant wavelength shifted by ~ 40 nm(28 nm). The starting values for Q are different because of fluctuations in the fabrication process. For sample S100 the Q degradation was more severe, from ~ 6500 to ~ 1000 and for this reason we mainly concentrate on samples S30 and S60.

With the chips mounted in the cryostat, we focused the 543 nm laser on the PC cavities for a fixed time and recorded the cavity spectrum. For sample S60, the cavity resonance shifted by up to 3 nm as shown in Fig.2.15(a). For $1\mu W$ of green laser power focused on a spot size of $\sim 1\mu m^2$, the cavity tuning rate levels off after about 20 minutes, as shown in Fig.2.15(b). We observed that this saturation time decreases

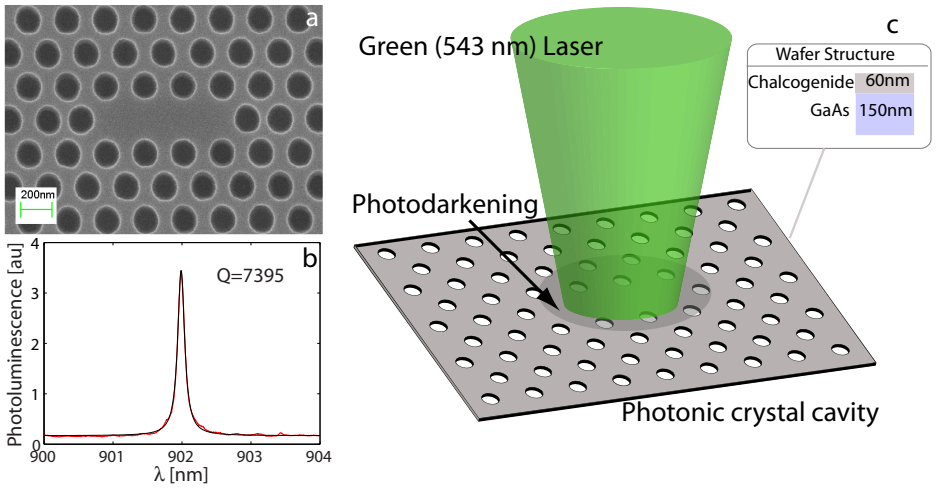

Figure 2.14: (a) Scanning electron microscope image of the photonic crystal cavity fabricated in GaAs before the deposition of As_2S_3. (b) Cavity PL spectrum before the chalcogenide deposition indicating a quality factor Q=7395. (c)Schematic of the method for local cavity tuning. A layer of As_2S_3 is deposited on top of the photonic crystal cavity. Then a laser tuned close to the As_2S_3 band gap is focused on the cavity, increasing the effective refractive index and causing a resonance red-shift.

with increasing power of the 543nm laser. During the tuning process Q degraded to 4650. The maximum tuning range depends on the thickness of the chalcogenide layer. For 30 nm and 100 nm, a tuning range of 1 nm (Fig.2.15(b)) and 4 nm was observed, respectively. Similar to S60, the quality factor for S30 also degraded to $Q \sim 4650$. We suspect that this is a limiting value given by a loss mechanism in the glass layer. It is possible that during the tuning process there are dislocations in between the glass layer and the GaAs substrate which induce scattering loss. The cavity resonance was stable after the green laser was turned off.

Illumination of As_2S_3 with light at 543 nm causes changes both in the refractive index and in the density of the material. Experiments at room temperature with films of As_2S_3 show that the increase in the refractive index is accompanied by a $\sim 1.5\%$ decrease in the film thickness. The decrease in thickness should result in a blue-shift of the cavity resonance. The red-shift observed experimentally implies that the dominant effect responsible for the shift of the cavity resonance is the change in

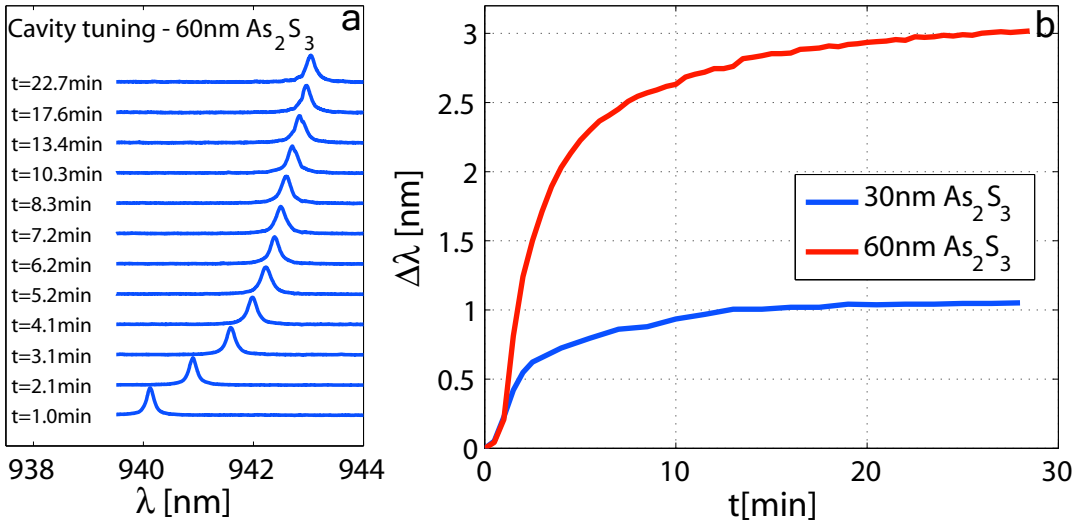

Figure 2.15: (a)Spectra showing the shift of the cavity resonance because of the photodarkening of the 60 nm thick chalcogenide layer. (b) Time dependence of the cavity resonance for 60 nm and 30 nm As_2S_3 during the tuning process.

the refractive index.

The behavior of the QDs during the tuning process is important for applications where QDs need to be spectrally aligned. In Fig.2.16 we show the tuning of a cavity that has several QD lines weakly coupled to it. For this data set we used a sample with 50nm of As_2S_3 (chip A58). Early in the exposure, these lines shift in the characteristic fashion shown in Fig.2.16: QDs first rapidly red-shift, then relax to a constant frequency. As coupled QDs tune across the cavity spectrum, they become bright due to the enhanced emission rate and outcoupling efficiency[27]. The cavity itself steadily red-shifts, even after the QDs have stopped tuning. We attribute the QD tuning behavior to strain in the sample. Initially, strain builds up as the sample is cooled to $\sim$ 10K because its thermal expansion coefficients is larger than that of GaAs[54]. The strain increases as the tuning beam is applied and the chalcogenide compresses, reaching a maximum after about 36 seconds in Fig.2.16. About 1 minute into exposure, the strain appears to relax as the QDs settle to a fixed emission wavelength. We attribute the relaxation to nanofracturing of the chalcogenide glass as the compressive

pressure exceeds the material's tensile strength (We estimate that without fracture, the chalcogenide layer would reach a tensile stress of $\sigma = Y_m \Delta L/L \approx 0.3$GPa, where $Y_m \approx 20$ GPa is Young's modulus, and $\Delta L/L \approx 0.015$ is the shrinkage. σ exceeds the glass's tensile strength of ~ 0.1GPa[55, 56], so we expect material fracture. Because of electron charging of the glass layer during SEM imaging, we could not observe fracture lines, but place a bound of less than 15 nm on their width). Once the strain is relaxed, only the cavity continues to red-shift. In applications where QDs must be tuned independent of the cavity, it might be necessary to first relax the strain or induce fracturing of the chalcogenide layer in some other way. However, we note that this ability to induce local strain may actually be useful for other applications, such as creating locally strained quantum wells[57], quantum dots, or impurities[17].

For our experiment, the smallest area that can be locally tuned is a few square microns, limited by the size of the laser beam focus and the propagation of the structural changes in the glass layer. The locality of the technique allows for independent tuning of interconnected optical components on photonic crystal chips. The method is not only suitable for GaAs devices, but can possibly be implemented with any other materials, including silicon nanophotonic circuits. Also, the As_2S_3 can easily be replaced by other types of chalcogenide glasses or other photosensitive materials depending on the specific application.

In conclusion, we have shown that chalcogenide glasses such as As_2S_3 can be combined with semiconductor photonic crystals to create nanophotonic devices whose optical properties can be independently fine-tuned on the same chip. This technique is relevant for fabrication of integrated nanophotonic circuits for classical and quantum information processing, including applications such as filtering, multiplexing, optical storage, fine-tuning of modulators and lasers, and local tuning of distinct PC cavities on GaAs/InAs chips for quantum optics. Combined with local temperature tuning, this technique provides another degree of freedom that allows for independent alignment of multiple cavities on a chip.

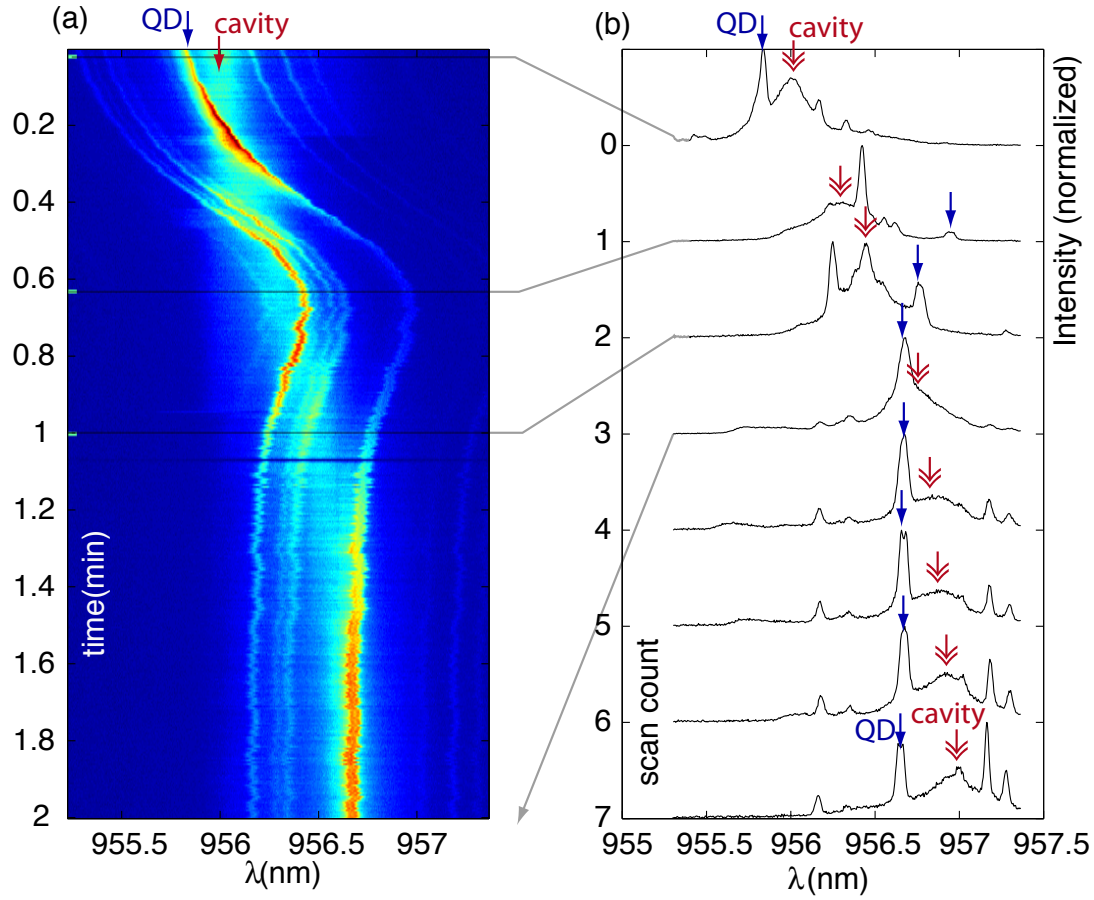

Figure 2.16: (a) Spectra showing cavity and QD shifting, as a function of exposure time. The QD lines first shift rapidly, presumably through changing material strain induced by the chalcogenide layer. Soon after, the QD lines become stationary, while the cavity continues to red-shift. This data set was taken on a sample with 50 nm of As_2S_3 (b) Individual scans of QD/cavity tuning show that after strain relaxation, the cavity can be shifted independently of the QDs. Scans 4-7 were taken for $t >$ 2min when the pump power was temporarily increased to speed up the chalcogenide exposure.

2.5 Local quantum dot tuning using DC Stark shift

The radiative properties of InAs quantum dots can also be controlled via an an electric field applied across the quantum dot. We have implemented this technique by placing the quantum dot in the depletion layer of a Schottky contact. This enables ultrafast control of the QD resonance inside the photonic crystal and tuning of the quantum dot resonance of a few tenths of nanometers, enough to detune the QD from a high Q cavity. The details of this technique are discussed in Chapter 5, where we present our electro-optic control of quantum dots in photonic crystal resonators.

Chapter 3

CQED with quantum dots in photonic crystals

3.1 Introduction

Cavity quantum electrodynamics (CQED) studies the interaction between the modes of an electromagnetic resonator and various emitters of electromagnetic radiation. The classical experiments in CQED involve the interaction between single atoms and the modes of high finesse resonators in either the optical regime or the microwave regime[58, 12]. However, in the past few years, several solid state CQED systems have been implemented. The most notable are the circuit QED[59] and the systems based on solid state optical emitters and micro/nano resonators[19, 60, 36]. The main focus of our work at Stanford has been the development of the experimental tools for studying the CQED with quantum dots coupled to photonic crystal resonators.

The first experiments showing cavity CQED effects with quantum dots and photonic crystals were done in photoluminescence[46, 36, 27]. The photoluminescence measurements are incoherent since they rely on the random trapping of carriers in the quantum dot. However, for any information processing application, the interaction between the photons and the cavity/QD system needs to be coherent. We performed the first coherent measurements on cavity/QD systems where we showed the coherent probing of a QD strongly coupled photonic crystal resonator[19]. I present this

measurement technique in section 3.2. The system was also used to show that the phase and amplitude of the light reflected/transmitted by the cavity can be controlled by saturating the QD[20]. In another experiment we demonstrated photon blockade and photon-induced tunneling [21] as described in section 3.3. All these experiments were done in collaboration with Dirk Englund and Ilya Fushman and they are equal co-authors on this work. The experiments were done on chip A53 that I fabricated in April 2007.

3.2 Coherent Probing of Quantum Dots Coupled to Photonic Crystal Cavities

In CQED experiments with atoms and Fabry-Perot cavities, the probing of the system is done via transmission measurements as schematically shown in Fig. 3.1(a). While this type of measurement is the natural choice for this kind of system, the most straight-forward measurement for quantum dots in photonic crystals was the photoluminescence [46, 36]. Direct transmission measurements are desirable in solid-state systems and in this section I describe our successful effort in implementing this type of measurements. To take full advantage of the photonic crystal architecture, one would ideally operate in a configuration where the cavity is interconnected via waveguides, as shown in Fig.3.1(a). However, for proof of concept experiments, the integration with waveguides is not necessary and the cavity can be probed via a reflectivity measurement.

The demonstration of QD-controlled cavity reflectivity has far-reaching implications for quantum information processing in solid-state systems, as it opens the door to high-fidelity controlled phase gates [11], single photon detection [61], coherent transfer of the QD state to photon state [10], and quantum repeaters employing nondestructive Bell measurements with the addition of a third long lived QD level [34].

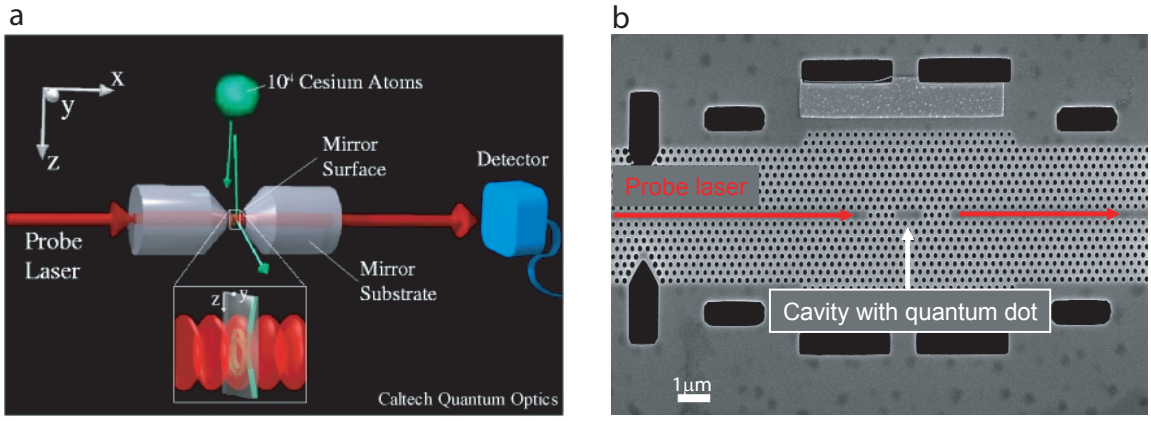

Figure 3.1: Transmission CQED measurements. (a) Schematic of the transmission measurement employed in CQED with atoms and Fabry Perot resonators. (J. Kimble group at Caltech, http://www.its.caltech.edu/ qoptics/) (b) On chip transmission measurement setup for a photonic crystal cavity connected to photonic crystal waveguides.

In the experiment, a narrow-bandwidth laser beam is scanned through the resonance of a GaAs photonic crystal cavity (Fig.3.2(c)). Our initial reflectivity measurements were done on a cavity with strongly coupled InAs quantum dot (QD) that splits its spectrum into two polariton states and causes the cavity transmission to vanish at the QD frequency. A linear three-hole defect in the photonic crystal (PC) forms the cavity with a resonant mode at $\lambda = 926$nm and measured quality factor $Q = 1.0 \cdot 10^4$ ($\Delta\lambda_{cav} = 0.10$nm). We observe a polariton splitting of 0.05nm.

The principle of the reflectivity measurement is shown in in Fig.3.2(b). It is difficult to observe the cavity spectrum directly because only a small fraction of the incident light couples to the PC cavity due to poor mode matching between the Gaussian probe beam and the cavity mode. For that reason, the signal reflected by the cavity is monitored in cross-polarization. A vertical ($|V\rangle$-polarized) probe laser is directed onto the linearly polarized cavity oriented at 45° ($|H + V\rangle$). Due to interaction with the cavity, the $|H + V\rangle$ component of the probe beam is reflected with a

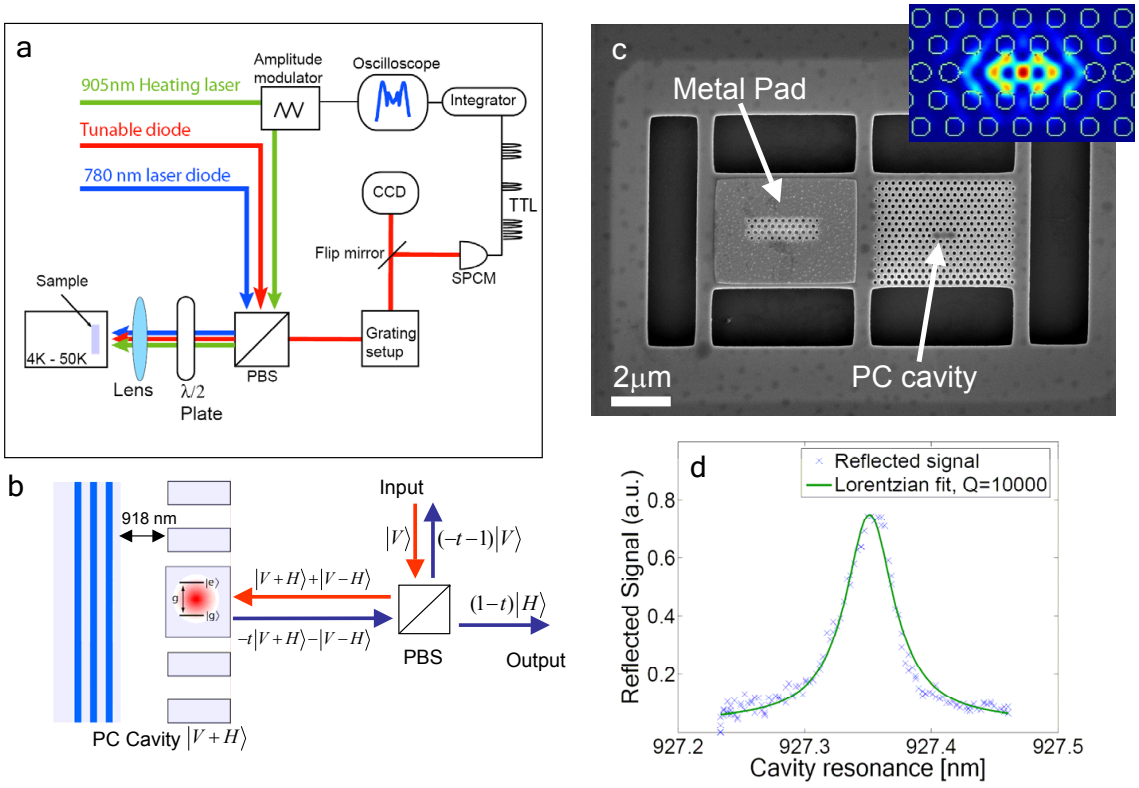

Figure 3.2: Experimental setup. (a) Confocal microscope setup. The cavity can be probed via photoluminescence using a 780 nm diode laser. The reflectivity is measured with a narrow-band tunable diode laser (focal spot diameter $\sim 1\mu$m for all beams). The temperature of the cavity is locally tuned using a heating laser (in this case a 905nm Ti:Saph laser). A grating setup monitors the photoluminescence and filters the reflectivity signal from background noise. The filtered reflected signal is detected by a Single Photon Counting Module (SPCM). (b) Principle of the reflectivity measurement off a PC cavity. (c) Suspended structure composed of a heating pad and a PC cavity. The heating laser incident on the metal pad controls local temperature. *Inset:* simulated electric field intensity of PC cavity. (d) Reflectivity spectrum obtained by tuning an empty cavity (no coupled QD) through the probe laser, indicating $Q = 1.0 \cdot 10^4$.

frequency-dependent coefficient $-t(\omega)$. The $|V-H\rangle$ component reflects directly with a π phase shift. The polarizing beam splitter (PBS) passes $|H\rangle$, giving a signal that is proportional to $|1-t|^2$ on the detector (see Eq.3.1). This is analogous to observing transmission through a polarizing cavity inserted between two crossed polarizers. A GaAs/AlAs Distributed Bragg Reflector (DBR) underneath the PC membrane effectively creates a single-sided cavity system and enhances collection efficiency of the probe beam. The horizontal $|H\rangle$ component of the scattered probe beam then carries the cavity reflectivity R as given by Eq.3.1.

Reflectivity is measured by scanning the narrow-linewidth probe laser beam through the cavity resonance, as shown in Figs. 3.2(a-b). In this way, we greatly exceed the 0.03nm resolution of the spectrometer in order to sample the narrow spectral features of the system (i.e., 0.05nm Rabi splitting).

The first trials to do reflectivity measurements were done by trying to scan a tunable diode (Sacher Lasertechnik) through the cavity resonance. These experiments were not successful because of the inability of the diode to scan continuously, mod-hop free over the cavity linewidth that is larger than 100GHz. To avoid difficulties related to laser stability and power normalization, we keep the laser wavelength fixed and instead scan the cavity and quantum dot using the local temperature-tuning technique[48] as described in section 2.2. The temperature of the cryostat was set to 27K so the QD emission wavelength is ≈ 0.5nm shorter than the cavity. The power of the heating laser is modulated such that the QD periodically swept through the cavity resonance. Then the tunable diode laser (used for reflectivity measurements) is spectrally aligned to the desired wavelength using the spectrometer. After spectral alignment, the 780 nm laser (exciting PL) is turned off, and the reflectivity signal is spectrally filtered using the grating setup of the spectrometer and sent to the SPCM. The SPCM outputs 10-ns TTL pulses that are integrated with an analog circuit and displayed on an oscilloscope. The tunable diode laser beam is spatially aligned to optimize the coupling into the PC cavity and thus increase the signal to noise ratio. Once the coupling is optimized, the output is switched back from the SPCM to the spectrometer CCD. The reflectivity signal is recorded using the spectrometer taking successive spectra with 0.2s long integration, while the heating laser power (and

subsequently QD and cavity wavelength) is modulated at 10mHz. This scanning speed is slow enough to resolve the relevant features, as seen by the number of data points sampling the QD-induced dips in Fig.3.3. We observed no improvement in resolution when the scan speed is reduced to 5mHz or below, implying that scanning resolution is not limiting the depth of the dip, but instead by heating laser power fluctuations, as explained in the text. A half-wave plate in front of the sample corrects for non-optimal orientation of the cavity and maximizes its visibility in the reflected signal (see Fig.3.2(a)). We verified that the visibility vanishes when the probe polarization is orthogonal or parallel to the cavity polarization. We obtain a cavity signal-to-background ratio of unity, which together with the imperfect extinction ratio of the polarizing beam splitter, lets us estimate that the coupling efficiency into the cavity mode in this experiment is $1 - 2\%$.

To accurately interpret the PL and reflectivity data, we need to know the frequency of the cavity and strongly coupled QD. Direct tracking of the strongly coupled QD is difficult because of its modified spectrum when coupled to the cavity, and because it rapidly decreases in intensity as it exits the cavity. This problem is solved by instead tracking a nearby QD that precisely follows, at a fixed offset, the strongly coupled QD's trajectory.

The reflectivity of the QD/cavity system is probed at five different spectral detunings $\Delta\lambda = \lambda - \lambda_{SC}$ of the probe laser (a narrow linewidth diode laser) from the intersection of QD and cavity. The incident power is in the weak excitation limit at 3nW (measured before the objective lens), corresponding to less than one photon inside a cavity per cavity lifetime, as required for probing the vacuum Rabi splitting. For each reflectivity scan, a corresponding PL scan is obtained to track QD and cavity wavelengths. Fig.3.3 plots the reflectivity signal as a function of temperature scan. In this data set, the temperature tuning is used to sweep the QD and cavity back and forth through the probe laser. As the single QD sweeps across the cavity, it strongly modifies the reflected intensity. Instead of observing a Lorentzian-shaped cavity spectrum as in Fig.3.2(d), a drop in the reflected signal is observed at the QD wavelength, as expected in the strong coupling regime.

The reflected signal from the described cavity is derived following Refs. [34] and

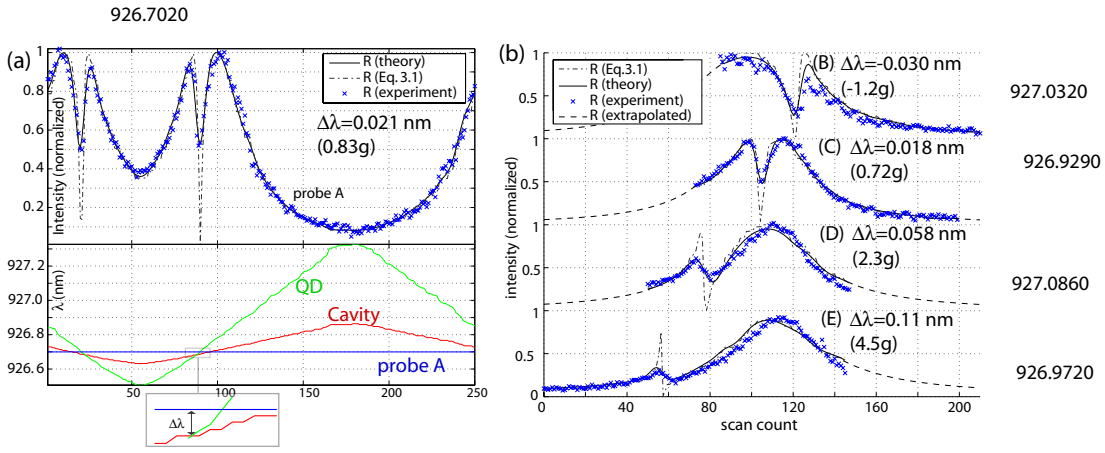

Figure 3.3: QD-controlled cavity reflectivity. (a) Reflectivity spectrum of probe laser as function of QD and cavity detunings, as determined from corresponding PL spectra. Detuning is controlled by local temperature tuning and horizontal axes correspond to tuning cycle. The probe laser is detuned by $\Delta\lambda = 0.021$nm (corresponding to $\Delta\lambda = 0.83g$) from the anticrossing point between QD and cavity (see inset). Ideal theoretical plots are calculated from Eq.3.1. Also shown are theoretical plots that take into account a ~ 0.005 nm-jitter of cavity and QD wavelength resulting from the heating laser power fluctuation. (b) Probe laser at various detunings $\Delta\lambda$ from the anticrossing point samples different QD-cavity detunings. Incomplete scans result from the limited range of temperature tuning.

[11]. The spectrum of the reflected probe signal after the polarizing beam splitter is then given by

$$R = \eta \left| \frac{\kappa}{i(\omega_c - \omega) + \kappa + \frac{g^2}{i(\omega_d - \omega) + \gamma}} \right|^2 , \tag{3.1}$$

where η accounts for the efficiency of coupling to and collecting from the cavity, ω_c is the cavity frequency, ω_d is the quantum dot frequency, and ω is the laser frequency. We fit this relation to the observed spectrum as shown in Fig.3.3(a) together with the tracked QD and cavity wavelengths. The experimental data show smoother features than the plot of Eq.3.1 based on tracked QD and cavity lines (dashed line). We attribute this difference to spectral fluctuations in the QD and cavity which are below the resolution limit of the spectrometer, but are greater than the linewidth of the probe beam. These fluctuations arise from instabilities in the power of the

heating laser of $\sim 0.7\%$. When thermal fluctuation in the QD/cavity wavelength is taken into account as a Gaussian broadening with FWHM=0.005 nm, the theoretical model matches the data (black fits). The fits yield values for coupling strength g and cavity Q that agree with PL measurements in above-band pumping. The reflectivity data for the other probe wavelengths, shown in Fig.3.3(B-E), capture the QD at various detunings from the cavity/QD intersection ranging from $-1.2g$(-0.03nm) to $4.5g$(0.11nm). The reflected probe drops toward zero precisely where the QD crosses its wavelength, and the depth and shape of the drop changes with cavity detuning as predicted by theory. We note that an alternative model of an absorbing QD[62] inside the cavity does not fit the reflectivity data and predicts a cavity spectral linewidth that does not agree with the measured value. These measurements also point to one of the advantages of the solid-state cavity QED system: it is possible to capture the spatially fixed QD in various states of detuning, while atomic systems are complicated by moving emitters.

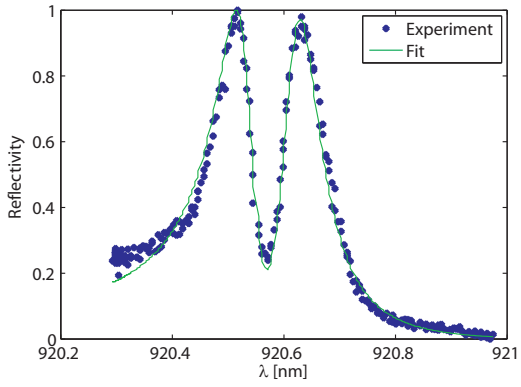

Figure 3.4: Reflectivity spectrum acquired by scanning the laser wavelength. The parameters of the system are $\kappa/2\pi = 29GHz$, $g/2\pi = 21GHz$

While the initial coherent probing of photonic crystal resonators was done using the local temperature tuning technique and in reflectivity, in later experiments we

used a new tunable laser diode (NewFocus Velocity) and we also performed experiments with waveguide coupled cavities (presented in section 4.3). A spectrum of a strongly coupled cavity/QD system acquired using the tunable laser[63] across the QD-cavity split spectrum is shown in Fig.3.4.

3.3 Photon Blockade and Photon-Induced Tunneling With a Strongly Coupled Quantum Dot

The development of coherent probing enabled fundamental studies of light-matter interactions in a coupled cavity/QD system. One of these studies involved the generation of nonclassical states of light using a quantum dot strongly coupled[36, 46] to a photonic crystal resonator. We showed that the capture of a single photon into the cavity affects the probability that a second photon is admitted. This probability drops when the probe is positioned at one of the two energy eigenstates corresponding to the vacuum Rabi splitting, a phenomenon known as photon blockade whose signature is photon antibunching [15, 64]. In addition, we showed that when the probe is positioned in between the two eigenstates, the probability of admitting subsequent photons increases, resulting in photon bunching. We called this process *photon-induced tunneling*. This system represents an ultimate limit for solid-state nonlinear optics at the single photon level. Along with demonstrating the generation of nonclassical photon states, we proposed an implementation of a single photon switch[65, 21] in this system.

The optical system consists of a self-assembled InAs quantum dot (QD) with decay rate $\gamma/2\pi \approx 0.1$ GHz coupled to a three-hole defect cavity in a two-dimensional GaAs photonic crystal, as described in ref. [19]. The QD-cavity coupling rate $g/2\pi = 16$ GHz equals the cavity field decay rate $\kappa/2\pi = 16$ GHz (corresponding to a cavity quality factor Q=10,000), which puts the system in the strong coupling regime[46, 36]. We first characterize the system in photoluminescence (PL) by pumping the structure above the GaAs bandgap. The PL scans in Fig.3.5(b) show the anticrossing characteristic of strong coupling between the QD and the cavity. Here, the QD is tuned into

resonance using local temperature tuning[48] around an average temperature of 20 K maintained in a continuous He flow cryostat. To generate nonclassical light, we coherently probe the system with linearly polarized laser beams (Fig.3.5(a)) and observe the cross-polarized output as described in our previous chapter. The cross-polarized setup allows us to separate the cavity coupled signal from the direct probe reflection, which is essential for achieving large signal to noise ratios needed in autocorrelation measurements. Our setup is such that the measurement on the reflected port from this single-sided cavity is analogous to a transmission measurement in a Fabry Perot arrangement.

The energy eigenstates of a two-level system strongly coupled on resonance to an optical resonator are grouped into two-level manifolds denoted $|n, \pm\rangle$, with energies $\hbar\omega_{n,\pm} = \hbar(n\omega_0 \pm g\sqrt{n})$, where n is the number of energy quanta in the system and ω_0 is the bare cavity frequency (Fig.3.6(a)). The anharmonic energy level spacing causes phenomena such as photon blockade or photon-induced tunneling. To observe photon blockade, a coherent probe beam (frequency ω_p) tuned to $\omega_{1,\pm} = \omega_0 \pm g$ is coupled to the cavity. This probe is resonant with the first-order manifold, but detuned from transitions to the second manifold, $\omega_{1\to 2} = \omega_0 \pm g(\sqrt{2} - 1)$ as shown in Fig.3.6(a). Consequently, once a photon is coupled into the system, it suppresses the probability of coupling a second photon with the same frequency. As a result, the output field acquires sub-poissonian statistics. In addition to photon blockade, photon-induced tunneling is expected near the bare cavity resonance ($\omega_p - \omega_0 = \Delta\omega_p \to 0$): the absorption of a first photon enhances the absorption of subsequent photons due to resonance with higher order manifolds, so the output consists of "photon bunches." These phenomena are purely quantum effects that cannot be explained using semi-classical theories. These effects can be probed by measuring the second-order correlation function, $g^{(2)}(\tau)$. The signature of the photon blockade effect is the antibunching in $g^{(2)}(\tau)$ (i.e. $g^{(2)}(0)$ is a local minimum, $g^{(2)}(0) < g^{(2)}(\tau)$), as recently demonstrated by Birnbaum et al [15] in an experiment with neutral atoms. In the case of photon induced tunneling $g^{(2)}(0)$ is a local maximum.

In Fig.3.6(b) we show the simulated theoretical output spectrum as a single-frequency probe beam is tuned through the cavity and indicate the resonance of

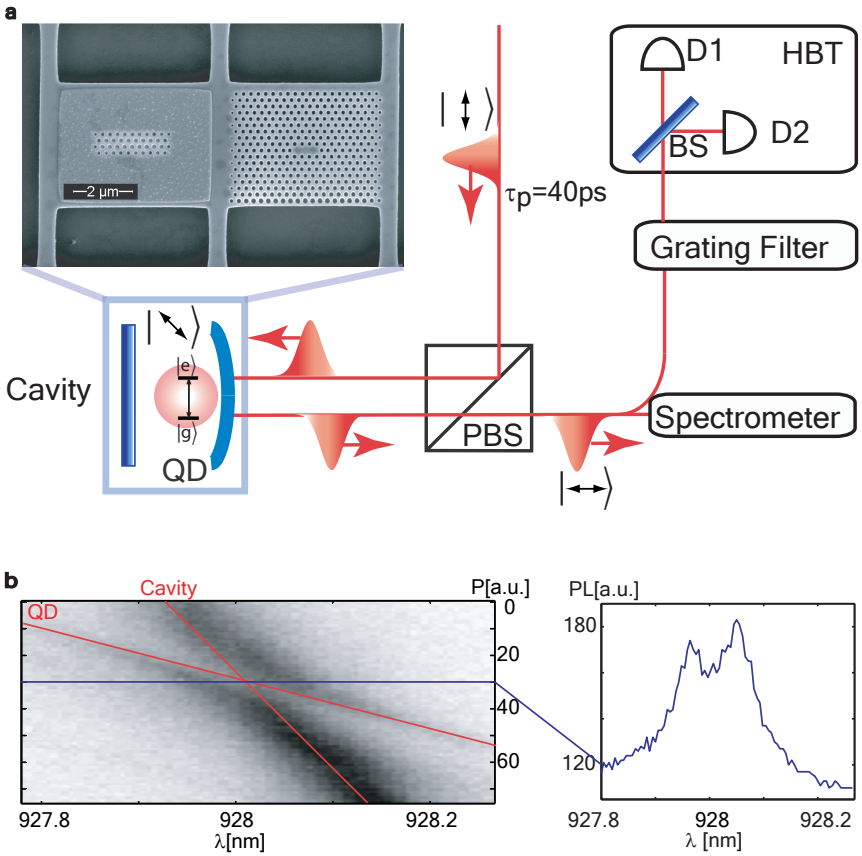

Figure 3.5: Schematic diagram of the experimental setup. (a) Laser pulses (40ps FWHM) are reflected from a photonic crystal cavity that is linearly polarized at 45° relative to the input laser beam polarization set by the polarizing beam splitter (PBS). The output light, observed in cross-polarization and carrying the cavity-coupled signal, is analyzed using a Hanbury-Brown and Twiss (HBT) setup that measures second-order correlation. The inset shows the suspended structure with the photonic crystal cavity and the metal pad for local temperature tuning. (b) Anti-crossing observed in photoluminescence as the QD is tuned into resonance with the cavity. The temperature tuning is done by linearly increasing the power (P) of the heating laser. The right inset shows the spectrum at the anticrossing point marked by the blue line. The red lines mark the cavity and QD resonance as if they were decoupled.

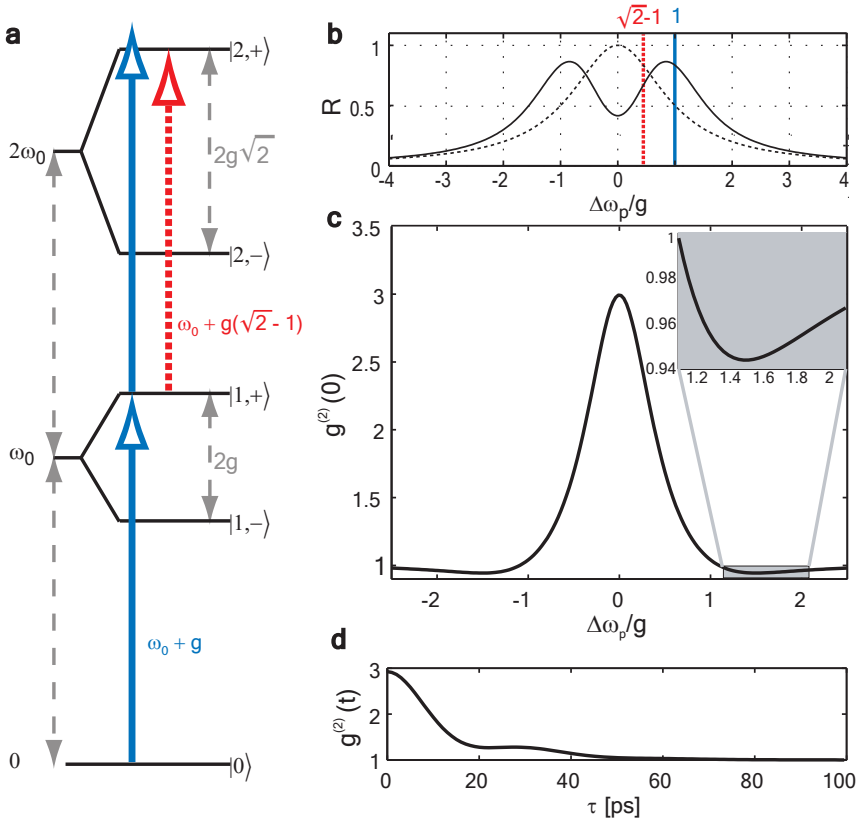

Figure 3.6: Theoretical analysis of the optical field reflected from the cavity. (a) Energy diagram showing the first and second-order manifolds of the strongly coupled cavity/QD system. The energy difference between consecutive manifolds is not constant as shown by the blue and the red arrows. (b) Simulated output intensity for a probe beam frequency tuned through the cavity/QD strongly coupled system (solid line). Dotted line shows the bare cavity reflectivity corresponding to QD in the *dark* state. The blue and red lines indicate the frequencies for the $|0\rangle \rightarrow |1,+\rangle$ and $|1,+\rangle \rightarrow |2,+\rangle$ transitions. (c) Computed second-order correlation $g^{(2)}(0)$ for a coherent laser probe reflected from the cavity. Inset shows that photon blockade is expected when the probe detuning is $\Delta\omega_p/g \sim 1.5$. As $\Delta\omega_p \rightarrow 0$ *photon induced tunneling* occurs, which results in a bunched output field. (d) Simulated time dependence of the second-order correlation for $\Delta\omega_p = 0$. The value for $(g^{(2)}(\tau))$ drops rapidly for time delays greater than $\sim$ 5ps, corresponding to the cavity photon lifetime.

the transitions $|0\rangle \rightarrow |1,+\rangle$ and $|1,+\rangle \rightarrow |2,+\rangle$. The simulated driving field injects an average cavity photon number $\langle n \rangle \sim 0.4$ when resonant with the polaritons in the first manifold, and slightly saturates the QD. The expected second-order correlation function for our system is shown in Fig.3.6(c), where we plot the dependence of $g^{(2)}(0)$ on the detuning $\Delta\omega_p$ of the probe from the anticrossing frequency ω_0. As expected from the intuitive argument above, the simulation predicts photon bunching as $\Delta\omega_p \rightarrow 0$. Photon blockade is evident in the antibunched region near $\Delta\omega_p \sim \pm 1.5g$ (see inset of Fig.3.6(c)). The blockade does not occur at $\Delta\omega_p = \pm g$ as previously explained because the linewidth of the eigenstates ($\sim \kappa$) is comparable to the splitting of the manifolds ($\sim 2g$), which results in a significant overlap of the allowed transitions between consecutive manifolds. As $\Delta\omega_p \rightarrow 0$, the probability of absorbing the first photon decreases. However, if a photon is absorbed, it enhances the probability of capturing subsequent photons, and produces a photon-bunched output.

We measure the time-dependent autocorrelation function $g^{(2)}(\tau)$ (Eg. 2.1) using the Hanbury-Brown-Twiss (HBT) setup shown in Fig.3.5(a) and described in (Eq.2.1) as described in Section 2.2 [66, 27]. The relevant features occur at time scales that correspond to the QD-cavity coupling rate g, enveloped by the coherence time[67], as shown in Fig.3.6(d). The coherence time for our system is given by the cavity photon lifetime $1/2\kappa \sim 5$ps. Hence, the time-dependent features in $g^{(2)}(\tau)$ occur much faster than the 300 ps time-resolution of the single photon counting modules in the HBT setup. In order to resolve the relevant features, we sample the autocorrelation function by short pulses ($\Delta t_{FWHM} \sim 40$ ps, $\Delta\omega_{FWHM}/2\pi \sim 12$ GHz) with a repetition rate of 12.5 ns. This probe pulse duration represents a compromise between fast sampling and a linewidth that is narrow enough to resolve the relevant spectral features. In the remainder of this section we present the measurements of $g^{(2)}(\tau)$ for different detunings of the probe beam, denoted as $g^{(2)}(\tau, \Delta\omega_p/g)$.

We scan several cavities until we find one which contains a strongly coupled QD, as determined by the anticrossing behavior in photoluminescence between QD and cavity during temperature tuning. Then we direct the pulsed laser beam at the cavity and observe the reflected beam in cross-polarization. While tuning the local temperature with an additional heating beam, we adjust the probe beam coupling to optimize the

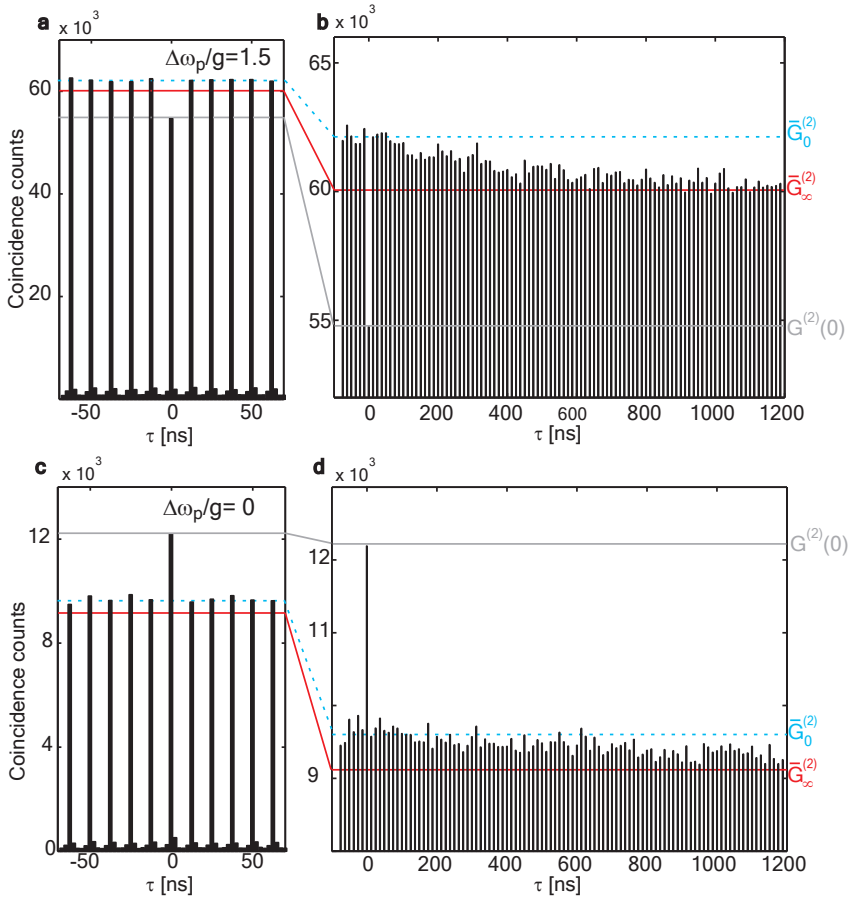

Figure 3.7: Measurement of the second-order correlation ($\overline{G}_0^{(2)}(\tau, \Delta\omega_p/g)$) function. (a) Photon blockade, manifested here in the sub-poissonian statistics ($\overline{g}^{(2)}(0, 1.5) = 0.91$), observed when the probe is detuned by $\Delta\omega_p/g = 1.5$. (b) The same data set as in panel **a** plotted for longer time delays. The red continuous line marks the normalization level $\overline{G}_\infty^{(2)}$. The blue dashed line indicates the classical bunching caused by quantum dot blinking. (c) Photon-induced tunneling ($\overline{g}^{(2)}(0, 0) = 1.34$) is observed when the laser pulse is tuned to the anticrossing point $\Delta\omega_p/g = 0$ (d) The same data set as in panel **c** plotted for longer time delays.

QD-induced reflectivity drop, as described for the continuous-wave beam in ref. [19] and in the previous section. Then we stop scanning and temperature-tune the QD and cavity into resonance. With the pulsed probe beam at different detunings with respect to the anticrossing point, we measure the autocorrelation signal by passing the reflected probe through a grating filter (to remove stray light) followed by the HBT setup. To limit sample drift, the alignment procedure is repeated for every detuning.

To observe photon blockade and photon-induced tunneling, we measured the unnormalized second-order correlation function at probe detunings $\Delta\omega_p/g = 1.5$ and $\Delta\omega_p/g = 0$ as shown in Fig.3.7. The expected photon antibunching and bunching behavior is clearly visible at zero time delay (Fig.3.7(b,d)). The histograms also show bunching over timescales of hundreds of nanoseconds. This bunching is a purely classical effect that results from the poissonian blinking of the QD. As reported by Santori et al[68], such blinking is caused by quantum dot transitions between an optically *bright* and *dark* state, and results in bunching near $\tau = 0$ that falls off with the mean switching rate. Our observations indicate that the blinking rates vary for different QDs. The QD measured in this experiment spends $\sim 80\%$ of the time in the *bright* state.

The blinking behavior of the quantum dot was also studied under continuous wave excitation. A CW laser was tuned at the anti-crossing point (photon induced tunneling) and the second order correlation was measured using the HBT setup. The blinking was analyzed for various power of the CW laser. It was obseved (see Fig.3.8 and Fig. 3.9) that for higher powers, the mean switching rate between the bright and the dark state becomes faster. A detailed analysis of the second order coherence in blinking systems can be found in ref.[69].

Photon blockade and photon-induced tunneling are quantified by the normalized second-order correlation function $g^{(2)}(\tau, \Delta\omega_p/g)$. Each peak in the histogram of Fig.3.7 represents the unnormalized value of the second-order correlation averaged over the pulse duration of 40 ps. We express this time averaging by using the notation $\overline{g}^{(2)}(\tau, \Delta\omega_p/g)$. The data is normalized such that $\overline{g}^{(2)}(\tau \to \infty, \Delta\omega_p/g) = 1$. We stress that $\overline{g}^{(2)}(\tau, \Delta\omega_p/g)$ captures both the quantum and classical nature (i.e.,

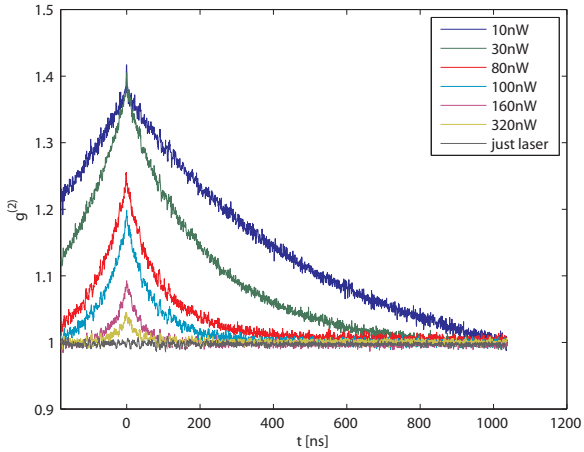

Figure 3.8: The second order correlation spectrum for different powers of the driving laser.

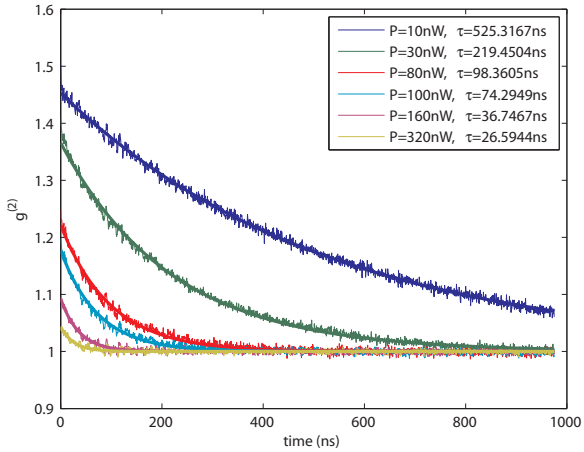

Figure 3.9: The second order correlation spectrum for different powers of the driving laser. The fit indicates the exponential decay in $g^2(\tau)$ which is related to the mean switching time between the dark and the bright state.

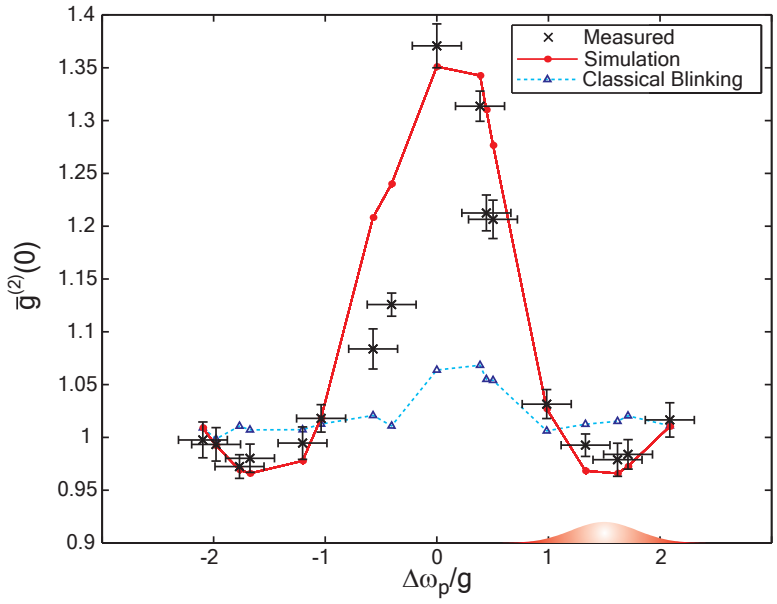

Figure 3.10: Measured normalized second-order correlation function $\overline{g}_0^{(2)}(0, \Delta\omega_p/g)$ for different detunings between the probe and the anticrossing frequency. As the probe is tuned through the resonance of the QD-cavity system, the output field shows either antibunched or bunched behavior as it transitions from the photon blockade regime to the photon-induced tunneling regime. For comparison we also plot the quantity $\overline{g}^{(2)}_{blinking} = \overline{G}^{(2)}_0/\overline{G}^{(2)}_\infty$, which corresponds to the bunching caused by quantum dot blinking (blue dashed line). The red continuous line shows the expected values of $\overline{g}_0^{(2)}(0, \Delta\omega_p/g)$ determined via a simulation that takes into account the finite pulse-width of the probe, QD blinking, and background due to the imperfect extinction of the cross-polarized setup. In the bottom-right corner we show the relative width of the pulsed laser probe.

blinking) of the output field. To find the normalization constant $\overline{G}^{(2)}_{\infty}$ we fit the histogram with the function $\overline{G}^{(2)}(mT_0) = (\overline{G}^{(2)}_0 - \overline{G}^{(2)}_{\infty})\exp[-mT_0/T] + \overline{G}^{(2)}_{\infty}$ for $m \geq 1$. The quantity $\overline{G}^{(2)}(mT_0)$ represents the number of counts at time mT_0, where m indexes the peak number with $m = 0$ corresponding to $\tau = 0$, and $T_0 = 12.5$ ns is the pulse repetition period. The normalized second-order correlation at $\tau = 0$ is $\overline{g}^{(2)}(0, \Delta\omega_p/g) = \overline{G}^{(2)}(0)/\overline{G}^{(2)}_{\infty}$ (see Fig.3.7 for details). In the case of photon blockade, $\overline{g}^{(2)}(0, 1.5) = 0.912 \pm 0.005$, showing the antibunched quantum nature of the system. For photon-induced tunneling, $\overline{g}^{(2)}(0, 0) = 1.33 \pm 0.02$ (Fig.3.7(d)), which indicates bunching.

There are several factors that account for the difference between the theoretically predicted (Fig.3.6(c)) and measured values for $\overline{g}^{(2)}(0, \Delta\omega_p/g)$: background due to imperfect extinction of the cross-polarized experimental setup (signal to noise ratio $\sim 6 : 1$), QD blinking and finite bandwidth of the probe that affects the spectral resolution. Both the background and the output signal when the QD is in the *dark* state result in a flat second-order correlation with $\overline{g}^{(2)}(\tau, \Delta\omega_p/g) = 1$ (coherent light). With the quantum dot in the dark state, the cavity reflectivity becomes that of an empty cavity as plotted by the dashed line in Fig.3.6(b). Near $\Delta\omega_p/g = 0$, the empty cavity (QD in dark state) has high transmission, so the observed signal has a large coherent-state component. As a result, the region near $\Delta\omega_p/g = 0$ is expected to show the largest deviation in $g^{(2)}(0)$ compared to the ideal (non-blinking) dot in Fig.3.6(c). This deviation will bring the observed $g^{(2)}(0)$ closer to $g^{(2)}(0) = 1$ of a coherent beam. At the blockade frequency ($\Delta\omega_p/g \sim 1.5$), the transmitted intensity in the dark state decreases relative to the bright state intensity (Fig.3.6(b)), and coherent light represents a smaller fraction of the collected signal.

We repeated the autocorrelation measurements for a large set of detunings to map the full spectrum of $\overline{g}^{(2)}(0, \Delta\omega_p/g)$. The measurement of the full autocorrelation spectrum entails several challenges such as sample drift resulting in fluctuating coupling intensity into the cavity, and fluctuating temperature. To map the dependence of $\overline{g}^{(2)}(0, \Delta\omega_p/g)$ on probe detuning, we maintained constant coupling into the cavity mode for the full duration of the experiment. Our most consistent data set is presented in Fig.3.10 where we plot $\overline{g}^{(2)}(0, \Delta\omega_p/g)$ for different detunings of the probe

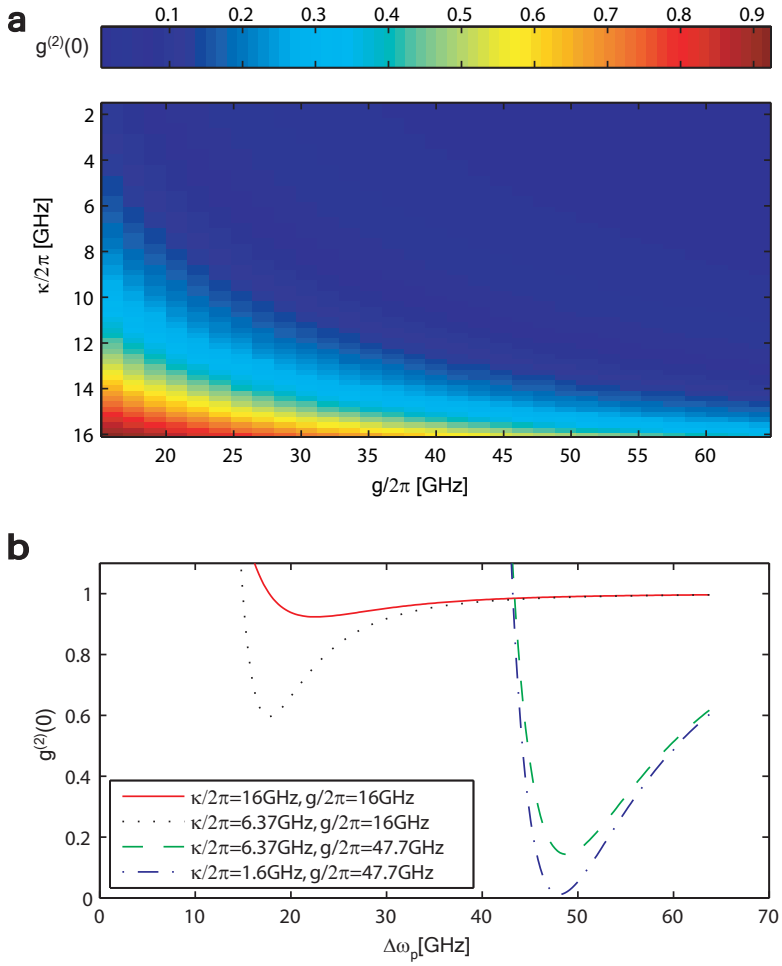

Figure 3.11: Expected photon blockade effect for various parameters of the strongly coupled system. (a) Colormap plot for $g^{(2)}(0)$ obtained in the photon blockade regime for $1.6 < \kappa/2\pi[\text{GHz}] < 16$ (i.e. $10^4 < Q < 10^5$) and $16 < g/2\pi[\text{GHz}] < 64$. (b) Plot of $g^{(2)}(0)$ versus probe laser detuning for four relevant cases. $\kappa/2\pi = 16\text{GHz}$ ($Q = 10^4$), $g/2\pi = 16\text{GHz}$ (red line) corresponds to the system reported here. $\kappa/2\pi = 6.37\text{GHz}$ ($Q = 25000$), $g/2\pi = 16\text{GHz}$ (black dotted line) is for a system with coupling strength similar to the one reported here but with the highest Q measured in our lab. $\kappa/2\pi = 6.37\text{GHz}$ ($Q = 25000$), $g/2\pi = 48\text{GHz}$ (green dashed line) corresponds to the highest measured Q and the highest achievable g with this type of cavity and quantum dot. $\kappa/2\pi = 1.6\text{GHz}$, ($Q = 10^5$), $g/2\pi = 48\text{GHz}$ (blue dash-dot line) is for the highest achievable g in this system and a quality factor four times higher than what has been currently achieved in GaAs photonic crystals at this wavelength.

frequency. To emphasize the nonclassicality of the signal, we plot in the same figure $\overline{g}^{(2)}_{blinking}(0, \Delta\omega_p/g)$, the bunched second-order correlation resulting from QD blinking. For every autocorrelation measurement, the nonclassical and classical contributions were easily distinguished by their greatly differing timescales as in Fig.3.7(c,d). The plots in Fig.3.10 show the transition from the blockade regime ($\overline{g}^{(2)} < \overline{g}^{(2)}_{blinking}$) to the photon induced tunneling regime $\overline{g}^{(2)} > \overline{g}^{(2)}_{blinking}$. The values for the classical bunching were obtained by taking the ratio $\overline{g}^{(2)}_{blinking}(0, \Delta\omega_p/g) = \overline{G}^{(2)}_0/\overline{G}^{(2)}_\infty$ (see Fig.3.7). As expected, $\overline{g}^{(2)}_{blinking}(0, \Delta\omega_p/g)$ is higher as $\Delta\omega_p/g \to 0$ because the intensity fluctuations due to blinking are largest at this detuning. While taking the data we kept a constant probe power of ~ 1.0 nW before the objective lens that corresponds to an average intra-cavity photon number $\langle n \rangle \sim 0.4$, and the coupling was re-optimized for every data point. The lowest value for $\overline{g}^{(2)}(0, \Delta\omega_p/g)$ obtained in this data set is not as antibunched as the value $\overline{g}^{(2)}(0, 1.5) = 0.912$ reported in Fig.3.7(b), because we could not reproduce exactly the same coupling conditions. We found that the experimental data in is well fit by a numerical model that takes into account pulses of finite bandwidth, QD blinking and background from the imperfect extinction of the cross-polarized setup (see Fig.3.10).

The numerical model for the second-order coherence in Fig. 3.10 is based on numerical integration of the quantum master equation. A time-dependent driving term in the Hamiltonian represents the 40-ps excitation pulses. The intensity of the drive field matches the intensity used in the experiment, representing one-third of the QD saturation intensity. In our experiment, this intensity was ~ 1 nW for the incident beam, measured before the objective lens. The state of the QD/cavity is time-evolved using a quantum Monte Carlo approach, which we based on the qotoolbox of ref. [70]. The Hamiltonian is given by

$$H = (\omega_d - \omega)\sigma_+\sigma_- + (\omega_c - \omega)a^\dagger a + ig(a^\dagger\sigma_- - \sigma_+ a) + E(t)(a^\dagger + a) \tag{3.2}$$

where the field $E(t)$ represents the time-dependent driving field (frequency ω) of the cavity and is given by a sequence of gaussian pulses. $a, a^\dagger$ denote the annihilation and creation operators of the cavity mode, while $\sigma_{+,-}$ are the raising and lowering

operators of the quantum dot. The QD can emit into free space or into the cavity mode, which in turn leaks photons into the output channel at the loss rate ω/Q. We then compute the autocorrelation on the output channel. The simulation additionally accounts for QD blinking and laser background. The full second-order coherence is calculated as a weighted sum of the different contributions,

$$G^{(2)}(\tau) = \langle \mathbf{a}^\dagger(t)\mathbf{a}^\dagger(t+\tau)\mathbf{a}(t+\tau)\mathbf{a}(t)\rho\rangle \quad (3.3)$$

$$= p_B G_B^{(2)}(\tau) + p_{BG} G_{BG}^{(2)}(\tau) + p_D G_D^{(2)}(\tau) \quad (3.4)$$

where the autocorrelation function $G_B^{(2)}(\tau)$ accounts for the QD bright state, $G_D^{(2)}(\tau)$ for the QD-dark state (calculated using $g \to 0$), $G_{BG}^{(2)}(\tau)$ for background laser signal (a coherent state) and p_B, p_D, p_{BG} are corresponding probabilities. The second-order correlation for zero time delay is computed as $g^{(2)}(0) = G^{(2)}(0)/G^{(2)}(1) \cdot [G^{(2)}(1)/G^{(2)}(\infty)]_{experiment}$. Here $G^{(2)}(1)$ is the the autocorrelation of the nearest-neighbor peak to $\tau = 0$ in the simulation. Due to computational constraints, this is not evaluated at the actual pulse repetition time $\tau = 12.5$ns but at $\tau = 300$ ps, a sufficient separation that amounts to nearly 60 coherence lengths. The factor $[G^{(2)}(1)/G^{(2)}(\infty)]_{experiment}$ is estimated from each autocorrelation measurement as $G^{(2)}(\tau = 12.5\text{ns})/G^{(2)}(\infty)$.

The experimental data in Fig.3.10 show that, starting from a coherent state, the strongly coupled system allows control of the statistics of the output field from sub-poissonian to super-poissonian. Thus, by engineering the parameters of the system and by choosing the appropriate probe frequency, one could generate various nonclassical states of light on demand. One of the most useful states is the single photon state that has applications in quantum cryptography and distributed quantum networking. To achieve efficient single photon sources based on photon blockade in strongly coupled solid state systems, the quality factor (Q) and the coupling strength (g) need to be higher than those in our current work. In Fig.3.11(a) we show the expected second-order coherence $g^{(2)}(0)$ when operating in the blockade regime for the range of parameters $1.6 < \kappa/2\pi[\text{GHz}] < 16$ (i.e., $10^4 < Q < 10^5$) and $16 < g/2\pi[\text{GHz}] < 64$. These estimations show that with $Q = 25000$ and $g/2\pi = 48$GHz, values achievable

in photonic crystals with InAs quantum dots [71], the single photon source should exhibit antibunching with $g^{(2)}(0) \sim 0.15$ (Fig.3.11(b)). For even higher quality factors ($Q = 10^5$), almost complete antibunching is expected ($g^{(2)}(0) \sim 0.01$). These simulations were performed assuming continuous-wave weak excitation (average cavity photon number $\langle n \rangle \sim 0.01$) of the system.

Using the anharmonicity of the eigenenergy spacing in this system, a single photon switch[65], could be implemented. In our switch scheme, the frequency of the gate field is resonant with one of the polaritons in the first-order manifold, say $\omega_0 + g$. A photon injected at $\omega_0 + g$ increases the probability of absorbing photons that are resonant with the $|1, +\rangle \rightarrow |2, +\rangle$ transition at $\omega_0 + g(\sqrt{2} - 1)$. If the signal is tuned to this frequency, the presence of the gate field enhances the transmission of the signal field [13]. The photonic crystal architecture allows for easy integration of such a single photon switch with photonic crystal waveguides[72, 73] so the single photon switching is done directly on the chip. The most straightforward configuration would be a photonic crystal cavity butt-coupled in between two photonic crystal waveguides[74]. For a practical implementation it is desirable that both the single photon source and the single photon switch operate in pulsed mode, with one photon emitted (or switched) per pulse. The performance of the device depends on the coupling efficiencies in and out of the cavity, the bandwidth, and the intensity of the pulse.

Chapter 4

Solid State Quantum Networks

4.1 Introduction

In this section I discuss our work on implementing on-chip optical networks based on the photonic crystal architecture. The main interest was toward developing devices where quantum dots coupled to photonic crystal cavities are integrated in a optical network via photonic crystal waveguides. I started working on this by looking into the coupling efficiency between photonic crystal cavities and waveguides[75, 72, 66, 76]. This is presented in section 4.2. I also worked with Dirk Englund on single photon sources coupled to waveguides, as discussed in Ref.[66]. After we obtained coherent probing of quantum dots coupled to photonic crystals, I worked on observing the coherent probing in waveguide-coupled photonic crystal cavities as described in section 4.3 [76].

4.2 Efficient Photonic Crystal Cavity-Waveguide Couplers

In this section I present the theoretical and experimental work on analyzing the coupling of photonic crystal linear three-hole defect cavities (L3) to PC waveguides. Efficient implementation of quantum computation devices requires on-chip integration

of photonic circuits consisting of PC cavities and waveguides [66]. The performance of these circuits is limited by the cavity-waveguide coupling efficiency. Our work investigates this coupling with the goal of improving the efficiency of single photon transfer into PC waveguides. The results are also relevant for channel drop filter applications in optical telecommunications. The systems are designed to increase the overlap between the evanescent cavity field and the waveguide mode, and to operate in the linear dispersion region of the waveguide. Our simulations indicate increased coupling when the cavity is tilted by 60^o with respect to the waveguide axis, which we have also confirmed by experiments (Fig. 4.1). We obtained up to 90% coupling efficiency into the waveguide. The results presented in this section were obtained on chip A17.

We investigated the waveguide coupling efficiency of linear three-hole cavities. The L3 cavities have a high quality factor to mode volume ratio and provide good matching between cavity and W1 waveguide field patterns, which improves in-plane coupling efficiency [28, 77]. The fundamental cavity mode has magnetic field with even/odd symmetry with respect to the **x/y** axes (Fig. 1.4). This mode (Fig. 4.1(a)) needs to be coupled to one of the guided modes in the PC waveguide. Of the possible waveguide bands inside the PC band gap [28] the best choice for coupling the L3 cavity is the one with similar symmetry and frequency as the L3 cavity mode (Fig. 4.1(b)). For efficient coupling, the cavity and waveguide modes need to be spatially overlapped and frequency matched. A closer look at the L3 cavity field profile (Fig. 4.1(a)) reveals that the evanescent field is strongest along a direction tilted with respect to the cavity axis and is weak along the cavity axis. A good approach for obtaining a larger overlap between the cavity and waveguide mode is to tilt the cavity with respect to the waveguide axis by an angle of 60^o (Fig. 4.1(c)). The choice of this angle is determined by the symmetry constraints of the triangular lattice. Directional couplers with cavity axes non-parallel to waveguide axes have also been studied by Kim et al [78] and by Shinya et al [79, 80]. In contrast with that work, we have developed optimized designs of couplers, and presented detailed theoretical and experimental data, confirming the advantage of the tilted configuration for coupling L3 cavities to PC waveguides.

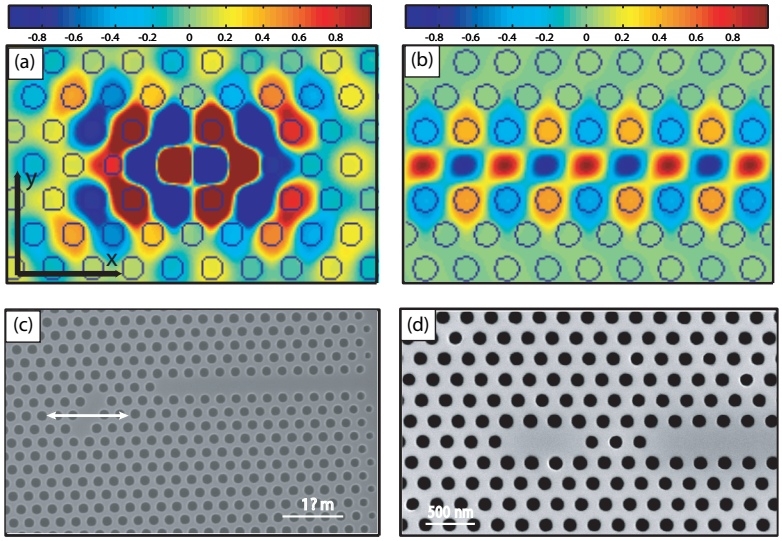

Figure 4.1: (a) Magnetic field (B_z component) for the mode with the highest quality factor in a L3 cavity. (b) Magnetic field pattern of the even mode in a PC waveguide. (c) Fabricated tilted cavity coupled to a waveguide (four holes separation). In this experiment we shift the cavity with respect to the waveguide along the direction indicated by the arrow. (d) Fabricated straight cavity coupled to a waveguide (three holes separation).

To test the validity of our approach, we compare the coupling parameters for the tilted cavity configuration (Fig. 4.1(c)) to the standard approach where the cavity and the waveguide share the same axis (straight cavity configuration) (Fig. 4.1(d)). First, three dimensional finite difference time domain (3D FDTD) simulations of coupled cavity waveguide systems were performed with both tilted and straight couplers. The frequency of the waveguide band was lowered with respect to the cavity frequency by reducing the size of the PC holes that bound the waveguide. In this way, coupling occurs in the dispersion-free linear region of the waveguide band. We directly simulated tilted and straight coupler configurations with spacing of two-to-five lattice holes separation between the cavity and the waveguide. The inset of Fig.4.3 shows an image of the simulated magnetic field profile for a tilted cavity coupled to a waveguide with three-hole separation. In the tilted configuration,

the separation between the cavity and the waveguide is changed along a direction indicated by the arrow in Fig. 4.1(c) and in Fig.4.2.

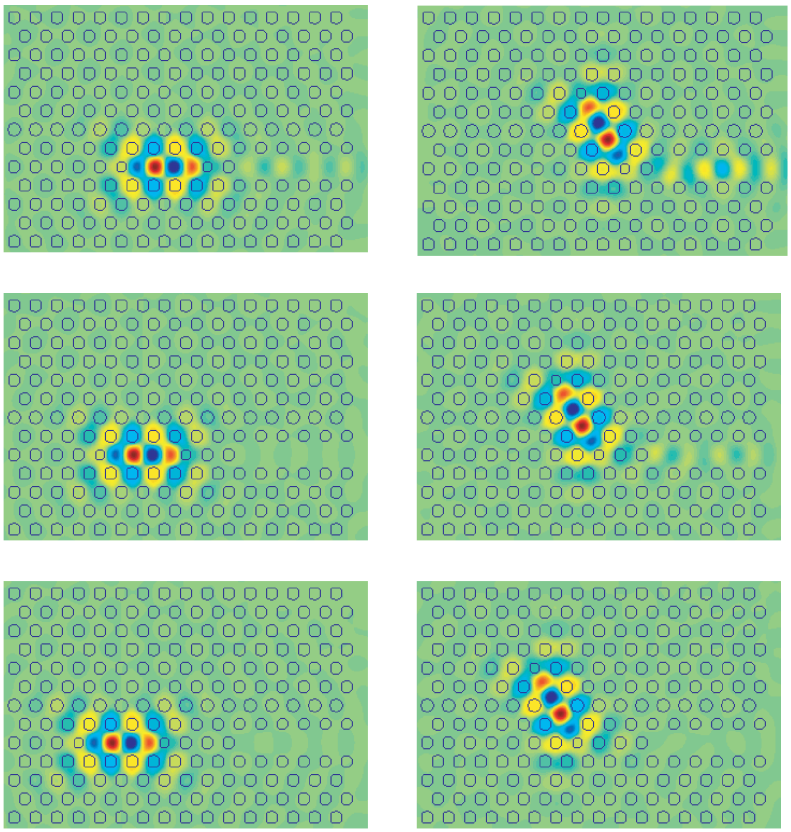

Figure 4.2: Simulated configurations for cavity-waveguide coupling. Magnetic field (B_z) is shown in all plots. Left: straight butt-coupled configuration with 2, 3 and 4 holes separation. Right: tilted configuration with 2, 3, 4 holes separation

The energy transfer into the waveguide degrades the Q of the coupled cavity. The total Q of a coupled cavity relates to the uncoupled cavity quality factor (Q_c) according to:

$$Q^{-1} = {Q_c}^{-1} + {Q_{wg}}^{-1}, \tag{4.1}$$

where Q_{wg}^{-1} is the loss rate into the waveguide.

Different applications require different coupling. For high-efficiency single photon transfer, the in-plane coupling into the waveguide modes needs to be dominant so Q_{wg} should be lower than Q_c. On the other hand, the advanced single photon sources [27] require cavities with a quality factor on the order of thousands, which implies Q_{wg} should also be in the same range. For other applications, single photons need to be scattered out of plane from a PC waveguide through an output cavity. To achieve high transfer efficiency from waveguides to the output cavities, the cavity-waveguide system needs to be in the critical coupling regime defined by $Q_{wg} = Q_c$. In that case, we do not need the output cavity to have a high quality factor.

The coupling strength between the cavity and the waveguide is given by $1/Q_{wg}$ which is proportional to the decay rate of the cavity field into the waveguide. The quality factor Q_{wg} was computed from the 3D finite difference time domain (FDTD) simulations, with results presented in Fig. 4.3. For the same cavity-waveguide separation, Q_{wg} is generally smaller for the tilted than for the straight configuration. This is an indication of better cavity-waveguide coupling obtained by tilting the cavity. One peculiar aspect of the simulations is that for the tilted coupling configuration, the Q is actually larger for four-holes than for five-holes separation. This is unexpected because it is natural to assume that reducing the distance between the cavity and waveguide should improve the overlap integral between the two modes. However, this increase in the quality factor is observed under a large variety of different simulation parameters, suggesting that it is real, as opposed to a simulation artifact. We suspect that, at four hole separation, the anti-node of one of the modes overlaps with the node of the other resulting in an lower overlap integral. Further investigation is required in order to conclusively confirm this.

The coupling changes from $Q_{wg} \approx 500$ for the tilted cavity with two-hole separation to $Q_{wg} \approx 10^6$ for four and five-holes separation (both configurations). For single photon sources based on PC cavities with InGaAs QDs operating at $900nm - 1000nm$, the experimental out-of-plane quality factor is limited to about $Q_c = 10^4$ because of material loss and fabrication imperfections [81]. On the other hand, to get efficient photon transfer into the waveguide, Q_{wg} needs to be lower than Q_c; therefore, only the coupling configurations with two- and three-hole separation represent good options.

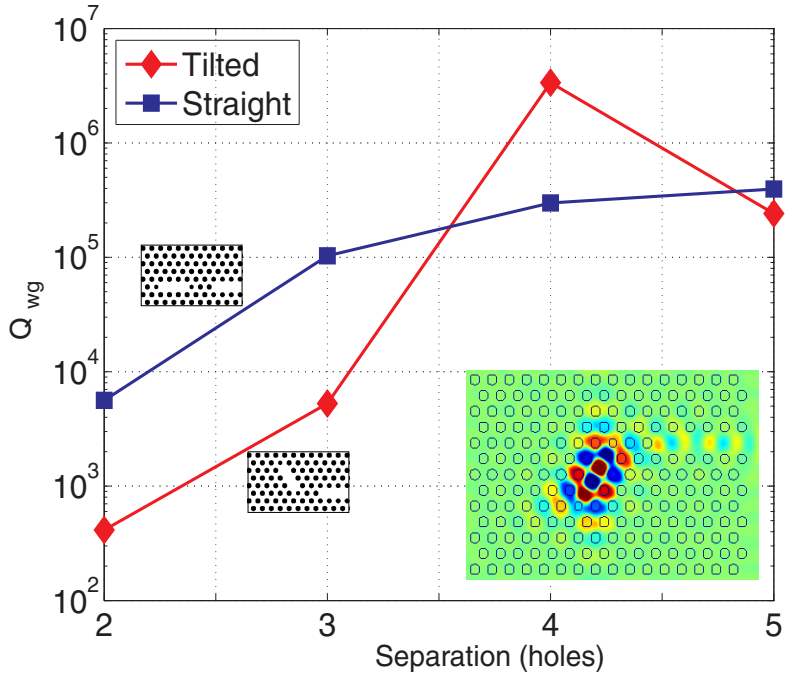

Figure 4.3: Simulation results for the cavity waveguide coupling expressed in terms of the quality factor. The coupling strength is proportional to $(1/Q_{wg})$. Simulated magnetic field of a cavity-waveguide coupler in tilted configuration with three hole separation (inset).

Experimentally we expect the total Q to be independent of the waveguide coupling in the case of four and five holes separation.

To test the validity of our simulation results, the couplers were fabricated on a 165 nm thick freestanding GaAs membrane containing an InGaAs QD layer, using our standard approach as described earlier in this thesis and in Appendix A. Structures with two- to five-hole separation in both tilted and straight configuration (Fig. 4.1(c, d)) were fabricated. We made seven structures of each kind. The spectrum of each cavity was measured using the InGaAs QDs embedded in the GaAs membrane as an internal light source. The mean value of the quality factor for each configuration is plotted in Fig. 4.4(a), where the error bars are given by the standard deviation in Q due to fabrication fluctuations between the seven structures of each kind.

The InGaAs QDs have a photoluminescence peak centered at 932 nm with an inhomogeneous line-width of 60nm. The quality factor of the coupled cavities was measured using the InGaAs QDs embedded in the GaAs membrane as an internal light source. The sample was cooled down at $5K$ using a continuous flow helium cryostat while the QDs were excited with a Ti:Sapphire laser tuned at 760 nm for above-band excitation. A confocal microscope setup was used for both QD excitation and photoluminescence (PL) collection. The spectrum of each cavity was recorded and the quality factor was determined by Lorentzian fitting. The mean value of the quality factor for each configuration is plotted in Fig.4.4 (a), where the error bars are given by the standard deviation in Q due to fabrication fluctuations between the seven structures of each kind.

As expected from simulations, the experimental data show that for the same cavity-waveguide separation, the total quality factor is lower for the tilted than for the straight configuration. This result is a consequence of higher coupling for tilted cavities.

Since a more efficient coupling between the cavity and the waveguide degrades the cavity quality factor, when designing a PC network one should choose the configuration that gives the optimum trade-off between transfer efficiency and high Q. One advantage of using the tilted cavity is that the same set of parameters can be obtained with the cavity further spaced from the waveguide.

As mentioned before, the cavity coupling was designed to couple in the linear region of the waveguide-band dispersion relation. To test the position of the cavity with respect to the waveguide band, we fabricated longer waveguides closed at the ends. These waveguides act as Fabry-Perot resonators. Fringes can be observed using the broad distribution of the QDs [82]. In the linear region of the dispersion relation the fringes are equally spaced, and get closer together as the frequency approaches the band edge. Since the cavity resonance was positioned in the region with equidistant fringes, we concluded that the coupling occurs in the linear region (Fig. 4.4(d)).

For a direct comparison between simulation and experiment, Q_c of the uncoupled cavity needs to be known. The upper bound for Q_c is limited by fabrication imperfections and material loss. Our simulation results indicate that in the case of coupled

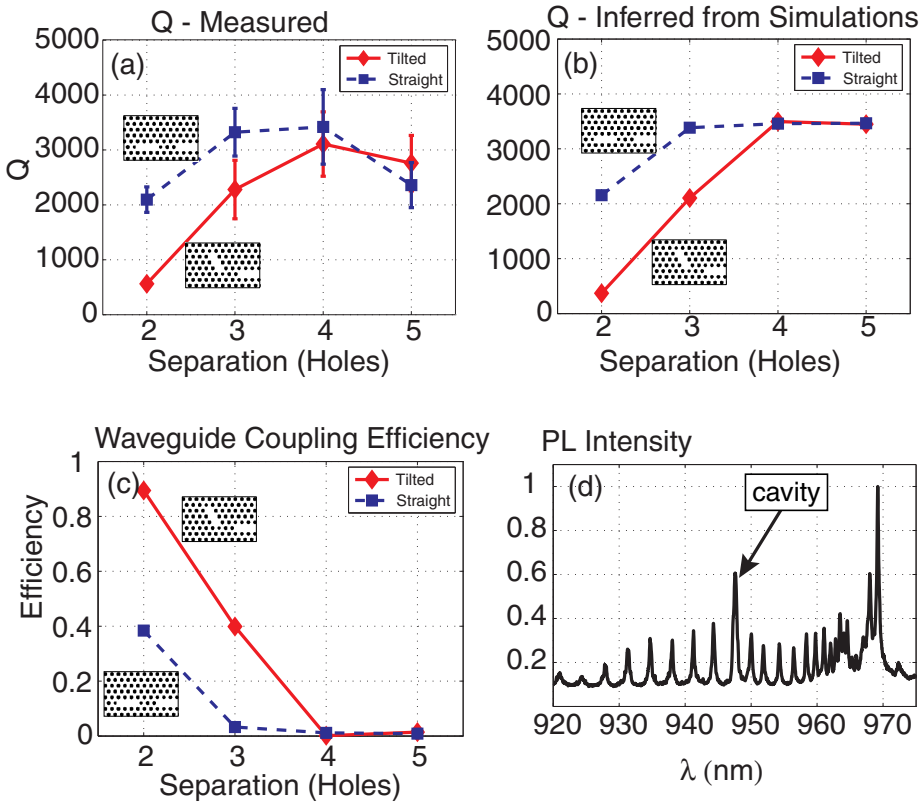

Figure 4.4: Comparison between simulations and experimental data for cavity-waveguide couplers. (a) The measured value of total cavity Q (mean) (b) The value of total Q inferred from simulations by combining simulated Q_{wg} and measured Q_c. (c) The coupling efficiency from the PC cavity into the PC waveguide. (d) Measured spectrum of a closed waveguide coupled to a L3 cavity. The Fabry-Perot fringes are equidistant in the linear region of the waveguide dispersion relation (where the cavity is also located) and they get closer next to the waveguide band-edge (970nm).

cavities with four hole separation the coupling into the waveguide is very small so the total Q is well approximated by Q_c. For this reason, the average value of the measured Q for the tilted configuration with four hole separation was used as Q_c. By plugging Q_c and the simulated value for Q_{wg} into expression (1), the predicted value for the total Q (Q_{tot}) was computed. The values for the Q inferred from simulations are plotted in Fig. 4.4(b) and show good agreement with the experimental data (Fig. 4.4(a)). Some inconsistency is observed in the case of five-hole separation. These inconsistencies result from fabrication errors.

The coupling efficiency into the waveguide was computed by taking the ratio Q/Q_{wg} and the results are plotted in Fig. 4.4(c). The coupling efficiency is up to $\eta \approx 40\%$ in the case of straight configuration with two holes separation and up to $\eta \approx 90\%$ for tilted configuration with two holes separation. Because of the coupling to the waveguide, the total cavity Q dropped to $Q \approx 500$ for the 90% coupling efficiency case. However, the small mode volume of the L3 cavity still enables large Purcell factors ($F \approx 50$) even with such a small Q. With $\eta \approx 90\%$ and $F \approx 50$ an efficient waveguide coupled single photon source with repetition rate of 10s of GHz can be built. As discussed in Ref.[71], these are two parameters that in addition to multiphoton probability suppression (which is unaffected by the cavity) determine the quality of a single photon source for most applications; a higher Q cavity will not improve these properties, as the repetition rate will still be limited to 10s of GHz by the carrier capture time.

In conclusion we have designed PC cavity-waveguide couplers with optimized coupling efficiency and operating in the linear waveguide dispersion region. We have shown both theoretically and experimentally that the coupling between a L3 PC cavity and PC waveguides can be improved by tilting the cavity with respect to the waveguide. The coupling is more efficient because the evanescent tails of the cavity field are not oriented along the cavity axis but at a 30^o angle. Understanding and controlling the coupling mechanism is essential for on-chip single photon transfer and the implementation of on-chip quantum networks.

4.3 Dipole Induced Transparency in Cavities Coupled to Waveguides

4.3.1 Dipole Induced Transparency

The experiments discussed so far focused on QDs strongly coupled to cavities (i.e., the regime in which the QD-cavity field coupling strength g is greater than $\kappa/2$ where κ is the cavity field decay rate). On the other hand, it has been theoretically predicted [34, 35] that a weakly coupled QD (with $g < \kappa/2$) can also control the photon transmission through a resonator, as long as the system is in the strong Purcell regime ($g^2/\kappa\gamma > 1$, where γ is the QD decay into modes other than the cavity mode). Such a regime is much easier to achieve in the solid state systems because $\gamma << g, \kappa$, as opposed to the atomic physics systems where κ is on the same order as γ [15]. This is especially important for the integrated structures, where cavities are coupled to waveguides, as such coupling degrades κ. We refer to such dipole assisted control of the photon transmission through a cavity as the dipole induced transparency [34, 35]; this effect can be classically explained as destructive interference at the output port of the PC cavity field induced by the QD dipole. Thus, by controlling the state of the quantum dot one can change the cavity transmission function from transparent to opaque. The state of the quantum dot can be controlled either by shifting its resonance frequency via various effects such as the AC Stark shift [20], DC Stark shift [83], Zeeman shift [38], or by saturation [19, 20] using coherent laser beams or injected carriers.

4.3.2 Device design and principle of operation

In order to utilize the full potential of PCs and enable high fidelity, low off-chip loss operations, photonic information should be kept on the chip and outcoupled at the final information processing step. Such a scheme results in efficient cavity-waveguide coupling, enhanced signal-to-noise ratios by separation of the input and output channels, and single mode operation, where a single cavity mode couples to a single waveguide mode. In this experiment we take the first step in this direction

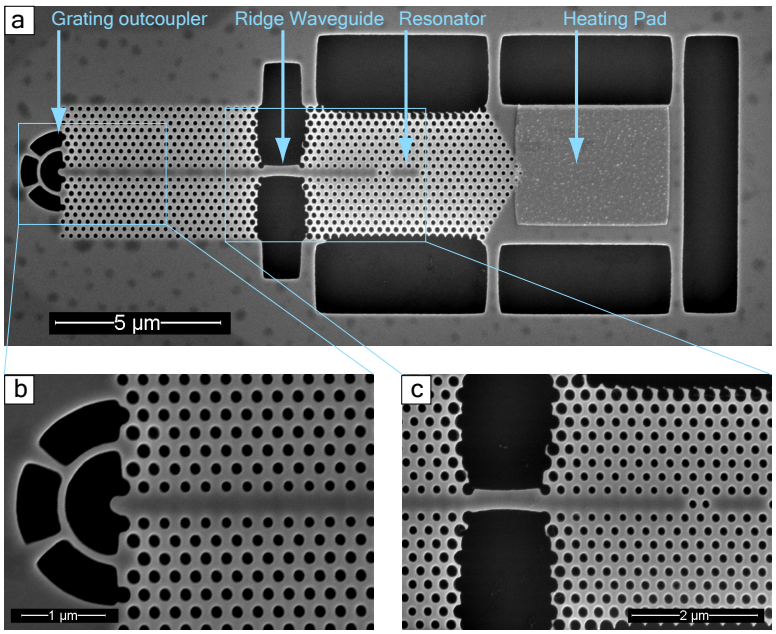

Figure 4.5: (a) Photonic crystal device used to probe dipole induced transparency. The device consists of a PC cavity coupled to a PC waveguide terminated with a grating outcoupler. For local temperature control, the cavity is placed next to a metal pad that can be heated using an external laser beam. To increase the thermal insulation of the structure, the PC waveguide is interrupted and a narrow ridge waveguide link is inserted. (b) Magnified view of the grating outcoupler. (c) Magnified view of the ridge waveguide link

by designing a device that enables on-chip transmission measurements of PC cavities with coupled quantum dots.

To this end, we designed a photonic crystal device that integrates cavities and waveguides. The device was fabricated on chip A53. For efficient light scattering out of the plane of the chip, the waveguide is terminated with a grating outcoupler. This allows us to measure the transmission of a probe beam injected into the cavity from the top, then coupled into the waveguide and outcoupled by the grating. The measurement principle is depicted in Fig. 4.6.

To achieve both large coupling efficiency into the waveguide and quality factors high enough for strong Purcell enhancements, we choose a linear three-hole defect cavity that is butt coupled to a PC waveguide with a two-hole separation between

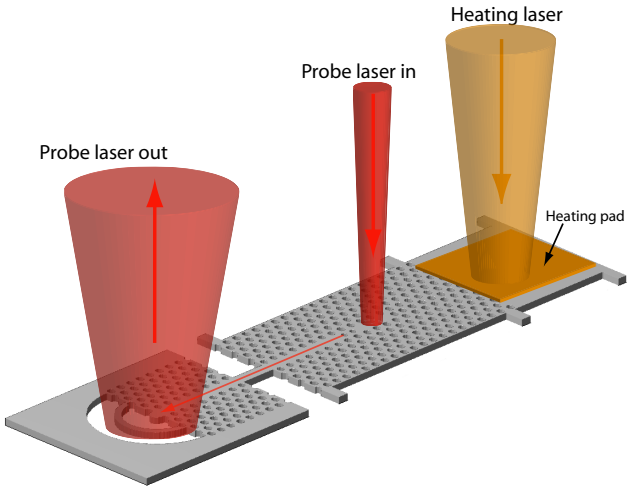

Figure 4.6: Schematic showing the operation of the PC device. A heating laser is used to control the device temperature thus changing the resonance frequency of the cavity and the quantum dots coupled to it. A probe laser is injected into the cavity from the top. The cavity field couples to the waveguide mode and then it is scattered from the grating outcoupler into the collection lens. A pinhole is used to collect only the output scattered by the grating. Using this device, the transmission function of the cavity can be analyzed for different frequencies of the resonator, quantum dot and probe laser.

the cavity and the waveguide[72]. The device is further integrated with a metal heating pad that enables local temperature tuning of the QD and cavity resonance via external laser beams [48, 19]. The suspended structure is connected to the rest of the substrate by only six narrow bridges to reduce the thermal conductivity [48]. One of the main thermally conductive elements is the photonic crystal waveguide. For increased thermal insulation we interrupted the photonic crystal waveguide and used a narrow ridge waveguide link.

To couple light from the photonic crystal waveguide out of the plane of the chip, we designed the grating outcoupler shown in Fig. 4.5(b). The grating outcoupler consists of a $\lambda/(2n)$ pitch grating (half-wavelength circular semiconductor-air stack)

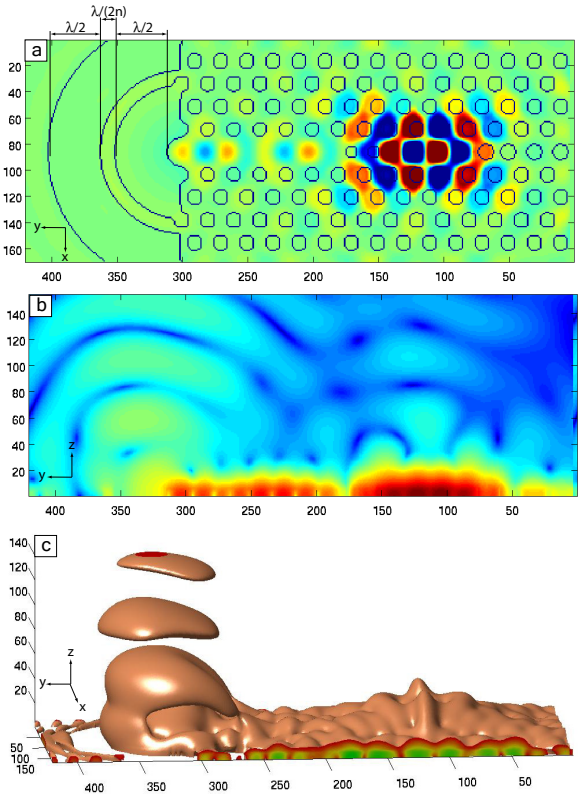

Figure 4.7: Simulation of the L3 cavity field coupled into the waveguide whose output is vertically scattered by the grating outcoupler. (a) Magnetic field distribution in the plane of the photonic crystal, i.e., the x-y plane (the dominant, B_z component is shown) (b) Energy density radiated from the structure, shown in the vertical cross-section through a plane passing through the middle of the waveguide and the cavity (x-z plane). Most of the vertically radiated energy is scattered from the grating outcoupler (c) Three dimensional view of one of the electromagnetic field density isosurfaces. This shows the profile of the evanescent cavity and waveguide field and indicates that most of energy radiated vertically comes from the grating outcoupler.

that causes destructive interference in the forward propagation direction and scatters most of the light into the collection lens. The grating is offset from the output port of the waveguide by $\lambda/(2n)$ (Fig. 4.7(a)).

To verify the scattering properties of the grating, the device was simulated using the finite difference time domain method. Due to limited computing resources, a smaller scale structure than the one shown in Fig. 4.5 was simulated. The structure

is shown in Fig. 4.7 (a) and consists of a L3 photonic crystal cavity butt coupled to a shorter PC waveguide that is directly terminated with the grating outcoupler. Fig. 4.7(a) shows the distribution of the z component of the magnetic field (B_z), and shows how the cavity couples to the waveguide. In Fig. 4.7 (b,c) we plot the energy density of the electromagnetic field, thus showing that the field scattered in the z directions comes primarily from the grating. From the time evolution of the outcoupled field, we computed that $\sim 50\%$ of the light outcoupled from the waveguide is scattered by the grating and collected into the microscope objective with 0.75 numerical aperture (NA) used in the experiment.

4.3.3 Theoretical analysis

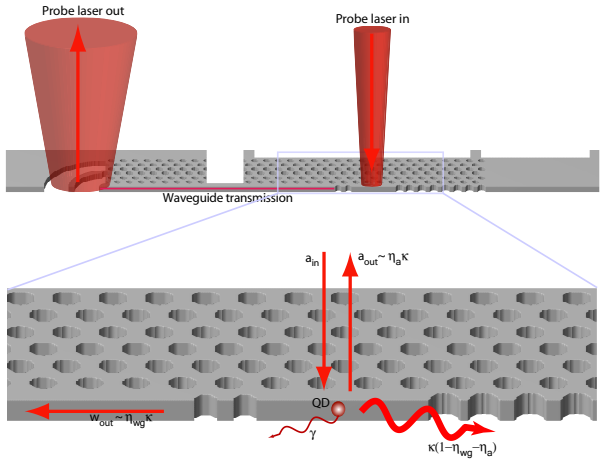

Figure 4.8: Schematic of the cavity mode coupling into various photonic channels. The cavity couples with coupling constant $\eta_a \kappa$ to the forward and backward propagating modes a_{in} and a_{out} of the probe beam. The other coupling channel of interest is the outward propagating waveguide mode w_{out} with coupling rate to cavity equal to $\eta_{wg}\kappa$. The cavity loss into all other coupling channels is $\kappa(1-\eta_{wg}-\eta_a)$. Therefore, the total cavity field decay rate is κ. The uncoupled quantum dot decay rate is γ

.

Following a coupled mode theory formalism similar to the one described in Ref.[34], the transmission function of the system is described by the formula:

$$T(\omega) = \left|\frac{w_{out}}{a_{in}}\right|^2 = \left|\frac{2\sqrt{\eta_{wg}\kappa}\sqrt{\eta_a\kappa}}{i(\omega_c-\omega)+\kappa+\frac{g^2}{i(\omega_{QD}-\omega)+\gamma}}\right|^2, \tag{4.2}$$

where w_{out} is cavity emission outcoupled into the waveguide and a_{in} is the mode of the lens used for coupling into the cavity. The coupling between the cavity and the quantum dot is g, the dipole decay rate without a cavity is γ, and ω_c, ω_{QD}, ω are the resonance frequencies of the cavity, quantum dot and probe laser respectively. The total cavity loss κ is divided into the loss into the waveguide $\eta_{wg}\kappa$, loss into the mode of the lens $\eta_a\kappa$, and loss into all the other channels $\kappa(1-\eta_{wg}-\eta_a)$ as shown schematically in Fig. 4.8.

To probe the dipole induced transparency we kept the probe laser constant and scanned the cavity and quantum dot resonance using local temperature tuning. During the local tuning process the cavity and quantum dot frequency shift linearly with the input power of the heating laser, with the quantum dot shifting approximately three times faster. The formula in Eq.4.2 can be rewritten in terms of the power of the heating laser (P) and the shifting rates of the cavity(α_c) and quantum dot(α_{QD}) with respect to the probe laser ($\alpha_{QD} \sim 3\alpha_c$):

$$T(P) = \left|\frac{2\sqrt{\eta_{wg}\kappa}\sqrt{\eta_a\kappa}}{i\alpha_c P+\kappa+\frac{g^2}{i\alpha_{QD}P+\gamma}}\right|^2, \tag{4.3}$$

When no quantum dot is coupled to the cavity ($g = 0$) the transmission function $T(P)$ has a Lorenzian shape. The effect of a coupled quantum dot is a drop in the transmission function [19, 34]. We stress that the transmission drop is not caused by absorption, but by the destructive interference at the output port caused by the interaction between the probe field, cavity field and the coherently driven quantum dot. While this effect is referred in literature as "dipole induced transparency" [34], in this particular configuration the dipole does not change the cavity transmission from opaque to transparent but the other way around (the quantum dot would induce transparency in a drop filter configuration [34]).

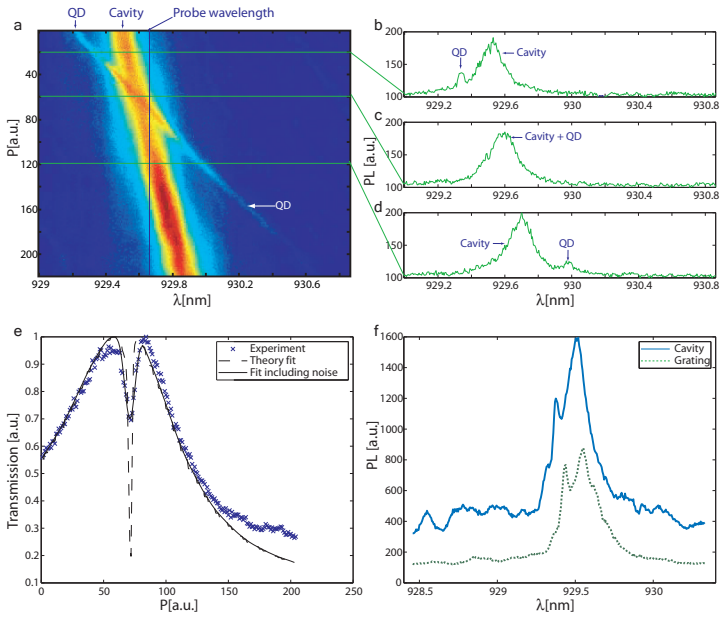

Figure 4.9: (a) Two dimensional photoluminescence plot taken as the quantum dot is tuned into resonance with the cavity by changing the power of the heating laser (plotted on the vertical axis). (b-d) Photoluminescence plots at three different crossections marked by the horizontal lines in panel *a*. As expected for the weak coupling regime, the QD and the cavity lines cross. (e) Transmission measurement done by changing the power of the heating laser while the probe beam is kept fixed at the frequency marked by the vertical line in panel *b*. The plot shows the Lorentzian profile of the cavity resonance and the dipole induced transparency transmission dip induced by the quantum dot. The dashed line is the direct theoretical fit with Eq.4.3. The solid line fit takes into account the fluctuations in the system. (f) Comparison between the photoluminescence spectra collected from the top of the cavity and the grating outcoupler. The two spectra were taken using a small aperture to collect only the photoluminescence from the area of interest. The ratio of the grating outcoupled cavity photoluminescence to cavity outcoupled photoluminescence is 0.64.

4.3.4 Experimental implementation

The device was fabricated on a quantum dot wafer grown by molecular beam epitaxy on a Si n-doped GaAs(100) substrate with a 0.1 μm buffer layer, and a 10-period distributed Bragg reflector consisting of quarter-wave AlAs/GaAs layers to improve collection efficiency into the lens. The distributed Bragg reflector is separated by a

918 nm sacrificial layer of $Al_{0.8}Ga_{0.2}As$ from the 160 nm GaAs membrane that contains a central layer of self-assembled InGaAs/GaAs quantum dots. The structure was fabricated using standard electron beam lithography, dry plasma etching and wet etching with hydrofluoric acid. To minimize the probability that more than one quantum dot couples to the same cavity mode, we used a sample with low quantum dot density ($\sim$ 100 quantum dots per μm^2). The tuning pad was deposited as described in Ref.[48].

The sample was placed inside a continuous flow liquid helium cryostat and the measurements were performed using an experimental setup similar to that described in Chapter 3. Using above-band photoluminescence (PL) under weak excitation, we measured $Q = 6140$ for the cavity quality factor, and a quantum dot weakly coupled to the cavity resonance was identified. The photoluminescence spectrum collected from the grating while locally tuning the temperature is shown in Fig. 4.9(a-d). Since the cavity-QD system is in the weak coupling regime, the spectrum does not show polariton anticrossing [48].

To characterize the grating outcoupler, a small aperture was used to collect photoluminescence either from the grating or the cavity. The collected spectra are plotted in Fig. 4.9(f). After background subtraction, the ratio between the grating collected PL and cavity collected PL was measured to be $PL_{grat}/PL_{cav} = 0.63$. Since for this cavity $Q = 6140$, assuming a uncoupled quality factor of $Q_c = 10000$ (similar to uncoupled cavities fabricated on the same chip) the Q corresponding to coupling into the waveguide can be deduced as $Q_{wg} = 15900$ [72]. This implies that $\sim 39\%$ of the cavity PL couples into the waveguide and $\sim 61\%$ is radiated vertically (because of the reflecting DBR under the cavity), thus indicating a ratio of $PL_{grat}/PL_{cav} = 0.64$ between the grating collected and cavity collected PL. This number is in excellent agreement with the one observed experimentally. However, we stress that despite the good matching the estimation is not completely accurate because the coupling losses at the PC/ridge waveguide interface and the coupling efficiencies into the numerical aperture of the lens were not taken into consideration. The losses in the system can only drive down the value for PL_{grat}/PL_{cav} observed experimentally, so the experimental result indicates that the grating radiates into the NA of the lens more efficiently than the cavity.

This is in agreement with simulations which show that $\sim 50\%$ of the light coupled into the waveguide is coupled into a lens with NA=0.75 while only $\sim 30\%$ of the light readiated by the cavity is coupled into the same NA (these estimations take the back reflection of the DBR stack into consideration). The exact coupling efficiencies both form the grating and the cavity are currently under more careful characterization. Further design optimizations could lead to $PL_{grat} >> PL_{cav}$, as desired.

The transmission measurements were performed using a focused diode laser (focal spot $\sim 1\mu m^2$) tuned to 929.65nm. The relative wavelength of the probe with respect to the cavity and quantum dot frequency is marked in Fig. 4.9(a). First, the coupling of the laser into the cavity was optimized using the cross-polarized reflectivity technique described in Ref.[19]. Once coupled, a small aperture was used to collect only the laser light transmitted from the cavity into the waveguide and then scattered by the grating. The experimental data for the device transmission is shown in Fig. 4.9(e). The data shows the Lorentzian transmission function of the cavity with a abrupt drop in transmission caused by dipole induced transparency with the weakly coupled quantum dot, as theoretically predicted [34]. To avoid quantum dot saturation, the experiment was performed at low probe power (tens of nW) [19].

To compute the parameters of the system, the data was fit with Eq.4.3 and the following values were obtained: $g/2\pi = 9.4$GHz, $\kappa/2\pi = 33$GHz, $\gamma/2\pi = 0.3$GHz. The result of the theoretical fit using Eq.4.3 is shown in Fig. 4.9(e). As seen from the fit, our data is not fully described by Eq.4.3 because of various sources of noise in the system, mainly the temperature fluctuations due to small power fluctuations of the heating laser (which in turn induce wavelength fluctuations of the QD)[19]. When taking into account these fluctuations (as described in [19, 20]), the solid line fit is obtained, in better agreement with the experimental data.

In conclusion, we observed dipole induced transparency in a photonic crystal device that integrates resonators, waveguides, outcouplers and local tuning elements. This shows that the coherent probing of coupled resonator-QD systems can be done not only in reflectivity but also in transmission measurements. In addition, the control of the light transmission through a resonator is done using a weakly coupled QD. The prototype device shown in this paper contains most of the building blocks of

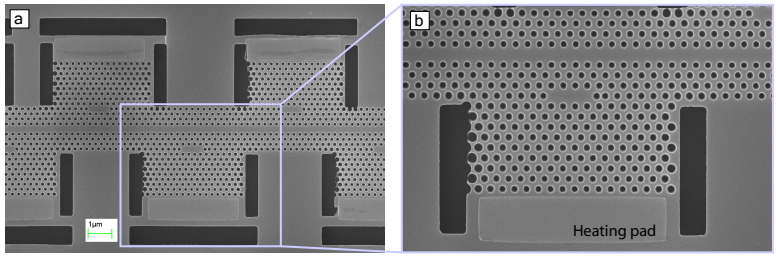

Figure 4.10: (a) Prototype structure consisting the of photonic crystal resonators evanescently side coupled to a waveguide. Each resonator is next to a heating pad so the its temperature and thus its resonance frequency can be controlled independently. (b) Magnified view of the waveguide coupled resonator and its heating pad. The trenches surrounding the resonator provide local thermal insulation.

future quantum dot - photonic crystal networks for classical and quantum information processing. To increase the performance and functionality of future devices the coupling into the resonator should be done via another waveguide and more cavities and quantum dots should be interconnected. A prototype design of this kind is shown in Fig. 4.10.

Chapter 5

Fast Electrical Control of Quantum Dots

5.1 Introduction

As previously described in this thesis, the quantum optics community puts a lot of emphasis on QDs because of their potential for coherently storing quantum bits[84, 85]. QDs don't have an inherent quantum level structure that allows for this kind of storage, but this can be engineered by placing the QD in specific environment of semiconducting layers and electromagnetic fields. The most promising scheme relies on QDs loaded with a single electron/hole such that the ground state can be split by applying a magnetic field. The loading of the electron/hole can be either deterministic by aligning the QD level with the Fermi level of a free electron/hole bath by applying a bias electric field[86, 87]. It has already been shown that the population in an electron-loaded quantum dot can be coherently manipulated using laser pulses[88, 16]. For quantum information applications, the QD manipulation should be done at singe photon level, so the QD needs to be placed in a optical resonator to enhance the light-matter interaction. Photonic crystal resonators are one of the best candidates for this task, so we investigated the possibility of doing electrical control of quantum dots in photonic crystals.

Beside the applications for quantum information science, electrical control of QDs

in photonic crystals can find applications in optoelectronic devices. As we have shown in Ref.[19], a well coupled QD can be used to change the reflectivity of a small mode volume resonator from transmissive to reflective via dipole induced transparency[34]. This directly implies that an optical switch can be implemented in this system by controlling the state of the quantum dot. All optical and electrical control are some of the most desirable control methods for optical switches because they enable speeds larger than 1GHz. In Ref.[20] we have already shown that the state of a quantum dot can be controlled via saturation with a detuned laser beam, which in turn can be employed to build an all-optical switch..

In this chapter I discuss our results in electrical control of the quantum dot using a lateral bias electric field. Using this method we realize an electro optical switch based on the quantum confined Stark effect(QCSE)[89] and the cavity quantum electrodynamics (CQED) in a strongly coupled QD.

5.2 Electro-optic switching with a strongly coupled quantum dot

The switch consists of an InAs QD coupled to a linear three hole defect photonic crystal cavity fabricated in a 160nm thick GaAs membrane (Fig.5.1(a,b)). The electrical control was achieved by applying a lateral electric field across the QD and thus shifting its resonant frequency via QCSE[83, 90]. The field was created in the depletion layer of a Schottky contact (20nm Cr/25nm Au on GaAs) deposited in the vicinity of the QD[91]. A scanning electron microscope of the device that integrates the photonic crystal resonator and the laterally positioned electrode is shown in Fig.5.1(a,b). Another Schottky contact located on the surface of the chip a few hundred microns away from the photonic crystal was used to set the ground potential.

One challenge in designing the device, is the small extent of the depletion layer in the vicinity of the Schottky contact. For typical undoped GaAs grown by molecular beam epitaxy, there is still a dopant concentration of $\sim 10^{16}/cm^3$ that limits the size of the depletion layer to a few microns for a 10V bias voltage. This requires the

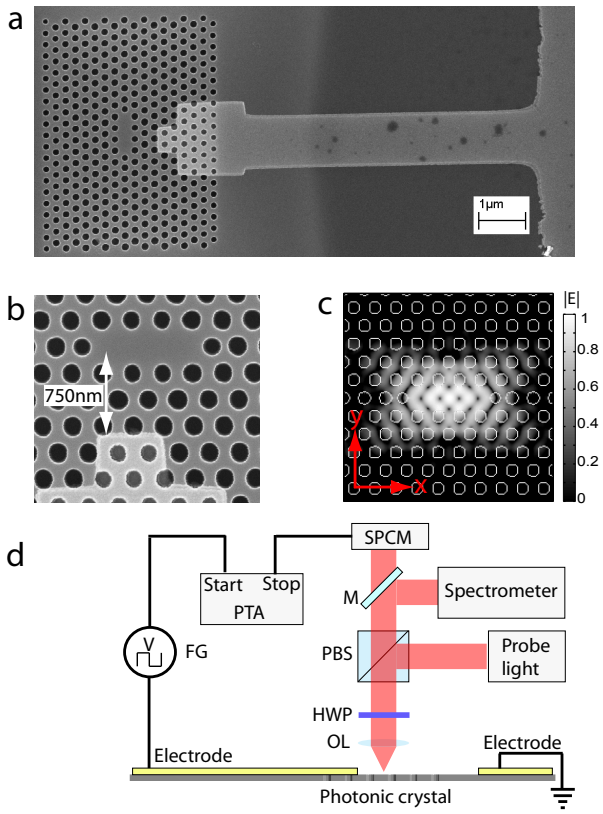

Figure 5.1: Design of a single QD-based electro-optic switch and experimental setup used for its characterization (a) Scanning electron microscope image of the photonic crystal cavity and the metallic electrode. (b) Magnified view the electrode placed within $1\mu m$ from the center of the cavity. (c) Simulated electric field density of the fundamental cavity mode. The field has minimal overlap with the metallic electrode. (d) Schematic representation of the experimental setup (not drawn to scale). A cross-polarized confocal microscope setup was used for photoluminescence and reflectivity measurements as described in the previous chapters The voltage on the chip was controlled using a function generator (FG) and the time domain measurements were performed using a picosecond time analyzer(PTA).

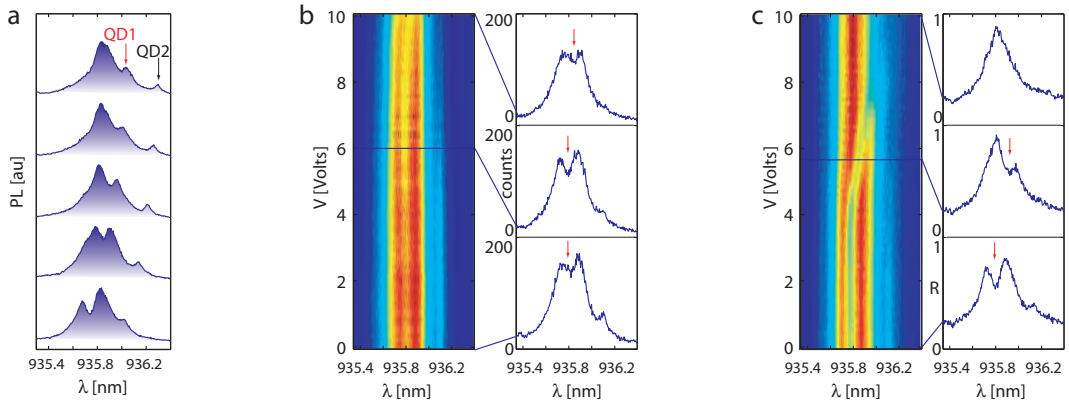

Figure 5.2: System characterization via photoluminescence and broadband reflectivity(a) Photoluminescence spectra taken for different cavity/QD detunings by increasing the temperature of the sample. The avoided crossing of the polaritons indicates that QD1 is strongly coupled. (b) Photoluminescence spectra while increasing the applied voltage V from 0V to 10V. At 0V the QD was tuned on resonance with the cavity (T=48K). The PL intensity decreases and the QD shows red shift as V approaches 10V. (c)Broadband reflectivity spectra while changing V from 0V to 10V (T=48K). The QD red shifts for $V > 4V$.

contact to be brought into a proximity of a few microns from the QD embedded in the photonic crystal cavity. Since metals introduce high optical losses, the device was designed such that the metal electrode, located within $\sim 1\mu m$ from the center of the resonator, has a minimum overlap with the optical mode. As shown in Fig.5.1(c), the fundamental mode of the resonator extends mainly in a direction that makes an angle of $\sim 30^o$ with the cavity axis (x) and has small extent in the y direction[72]. To minimize the optical loss, we bring the electrode in the proximity of the resonator along the y direction. With the electrode fabricated in this configuration, we did not observe significant degradation of the quality factor. On the same chip, we measured electrically controlled resonators with quality factors as high as 17000, similar to cavities without the metal electrode. The cavity studied in this chapter has a lower quality factor because it is integrated with a grating structure that allows efficient

resonant in/out coupling from the resonator, as discussed in [63]. The device was fabricated using standard semiconductor fabrication techniques as already discussed in this dissertation.

The measurements were performed in a liquid helium flow cryostat at temperatures from 4K to 50K. First, a photoluminescence (PL) measurement was used to identify a strongly coupled QD. The signature of strong coupling is the vacuum Rabi splitting, observed (Fig.5.2(a)) as an avoided crossing of the system eigenstates when the QD is tuned into resonance with the cavity [46]. From the PL spectra one can identify two QDs with frequency close to the cavity resonance, labeled as QD1 and QD2 in (Fig.5.2(a)). Only QD1 shows the avoided crossing, thus indicating strong coupling. All the measurements reported here were done using QD1, but the signature of QD2 was still visible in some of the data sets. For clarity, QD1 is marked with a red arrow in some of the figures. The experimental data indicate a cavity quality factor ($Q \sim 4000$, corresponding to field decay rate $\kappa/2\pi \sim 40GHz$), and a QD cavity coupling rate ($g/2\pi \sim 20GHz$). Since $g \geq \kappa/2$ and $g, \kappa >> \gamma$, ($\gamma/2\pi \sim 0.1$GHz), the system operates on the onset of the strong coupling regime.

The vacuum Rabi splitting can also be observed via resonant probing in a cross-polarized reflectivity measurement[19] as shown in Fig.5.2(c). The reflectivity measurement gives the transmission function of the optical resonator. In this experiment we use two types of resonant probing. In one case, a continuous wave (CW) laser beam is scanned through the cavity resonance and the output is monitored with a photodetector. This measurement is referred as 'CW reflectivity'. In the second case, a broadband light source is coupled into the resonator and the entire reflectivity spectrum is monitored on a spectrometer. This measurement is referred as 'broadband reflectivity'. While CW reflectivity gives very precise spectral information of the system due to the narrow linewidth of the laser (∼300KHz), it is relatively slow. The broadband reflectivity gives all the spectral information at once but it is limited by the resolution of the spectrometer (∼0.025nm).

With the QD and the cavity brought into resonance (temperature set to $T = 48K$), the effect of the electric field was first studied in PL by changing the bias voltage from 0V to 10V. As the bias approached $\sim 10V$, the total PL intensity decreased and the

QD showed a red shift of only $\sim 0.03nm(0.04meV)$ as shown in Fig.5.2(b). The shift in the QD resonance is due to the QCSE, and the reduction in the PL intensity is caused by the carriers being swept away before recombining in the QD. The DC Stark shift and the PL reduction were only observed when using low powers of the excitation laser (tuned at 875nm). By increasing the intensity of the laser, more carriers were excited in the cavity and thus screened the electric field.

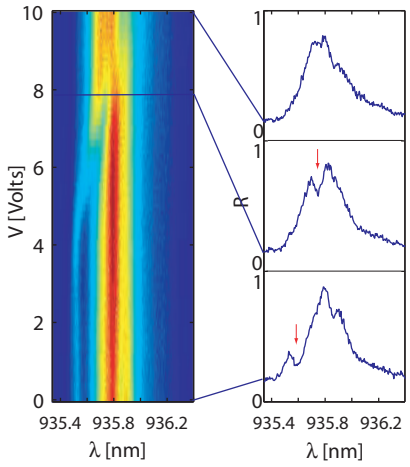

Figure 5.3: Broadband reflectivity spectra while changing the applied voltage V from 0V to 10V (T=46K).

To overcome the screening due to free carriers, the system was probed using broadband reflectivity. A superluminescent diode with broad emission around 935nm was used as the light source, thus minimizing free carrier generation. As shown in Fig.5.2(c), the effect of the bias voltage on the QD wavelength is more pronounced than in the PL measurement. The DC Stark shift could be observed for bias voltages larger than $V \sim 4V$, and for voltages exceeding $V \sim 7V$ the QD was completely detuned with the cavity. As seen from Fig.5.2(c), by applying the electric field the transmission at the cavity resonance is switched from a local minimum to a local maximum. Another data set taken at $T = 46K$ (Fig.5.3) indicated that the QD

continues to red shift until $V \sim 8V$, then its signature vanishes most likely because the QD confining potential became strongly perturbed by the electric field.

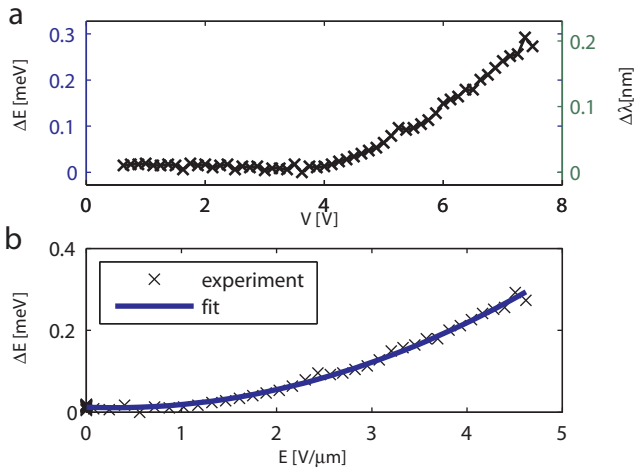

Figure 5.4: QD energy shift with bias voltage (a) DC Stark shift of the QD with applied bias. (b) Experimental data and fit indicating the quadratic dependence of the red shift with electric field

The dependence of the quantum dot Stark shift with the applied bias voltage was extracted from the spectra[19] in Fig.5.2(b), and is shown in Fig.5.4(a). The Stark shift is only observed for voltages larger than $V \sim 4V$, which corresponds to the depletion layer extending to the location of the quantum dot. The magnitude of the electric field in the center of the cavity was inferred by modeling the Schottky contact. The size of the depletion layer ($x_d(V)$) and the electric field in the cavity ($F(V)$) are given by $x_d = \sqrt{2\epsilon_0\epsilon_{GaAs}(V-\phi)/(eN_d)}$ and $F = -eN_d(x_d - \Delta x)H(x_d - \Delta x)/(\epsilon_0\epsilon_{GaAs})$. Here, $\Delta x = 750nm$ is the distance between the electrode and the center of the cavity, $N_d = 9\times10^{15}/cm^3$ is the doping concentration, $\phi = 0.36V$ is the potential barrier of the Schottky contact, e is the electron charge, $\epsilon_{GaAs} = 12.9$ is the dielectric constant of GaAs at low temperatures, ϵ_0 is the electrical permittivity of vacuum, and $H(x)$ is the unit-step function. The effect of the surface states were not considered when estimating the electric field. The dependence of the energy shift with electric field is shown in Fig.5.4(b). The shift was quadratic in electric field, since the perturbation of the energy levels due to electric field is a second order effect.

The data was fit using[91] $\Delta E = pF - \beta F^2$ with $\beta = -0.015 meV\mu m^2/V^2 = -2.4 \times 10^{-36} J/(V/m)^2$ and $p = -0.009 meV\mu m/V = -1.4 \times 10^{-30} Cm$. These values are within an order of magnitude but lower than previously measured by other research groups [92, 91, 93]. We believe that the lower value that we estimate is caused by the QD not being located exactly in the middle of the cavity, as we assumed.

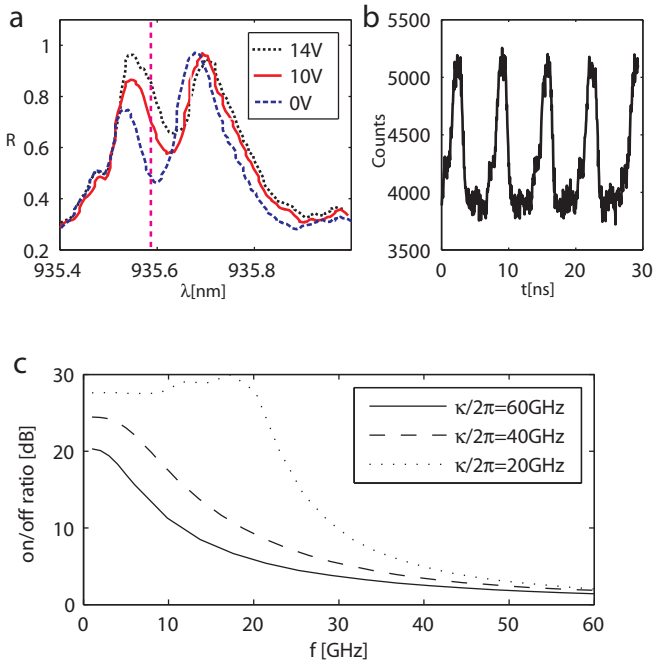

Figure 5.5: (a) CW reflectivity for bias voltages of 0V, 10V and 14V. During the time-domain switching experiment the laser was set at the wavelength marked by the vertical dashed line. (b) Switching of the coupled laser at driving frequency of 150MHz. (c) The dependence of the on/off ratio on the driving frequency (simulation). The system parameters are: $g/2\pi = 20GHz$,$\gamma = 0.1GHz$,$\kappa = (20, 40, 50)GHz$; QD frequency shift is $\delta = 5GHz$.

To demonstrate time domain switching, a CW laser was resonantly coupled into the cavity. The CW reflectivity spectra for different values of the bias voltage are shown in Fig.5.5(a). The DC Stark shift was still present but its magnitude was smaller compared to the broadband reflectivity measurement ($0.04meV$ for $V \sim 10V$). Unlike the broadband source, the CW laser had long coherence length, so it could efficiently drive the cavity/QD system thus creating resonance fluorescence[63] and

carriers that could screen the electric field[94]. The screening became more pronounced with increasing laser intensity. The presence of more than one QD in the cavity could also contribute to the generation of extra carriers. For a more quantitative estimation on how the resonant driving affects the electric field screening, the experiment should be repeated on samples where only one QD is present in the cavity. The CW reflectivity spectra in Fig.5.5(a) indicate that an on/off switching ratio of 2:1 is achievable with this system. The on/off ratio is limited by the properties of the QD, especially decoherence[63] and blinking[21]. For an ideal QD the on/off ratio can exceed 100:1(Fig.5.5(c)), depending on the system parameters. The best strongly coupled systems studied in our lab[63] had an on/off ratio of 5:1.

The time domain measurement was performed by setting the probe laser at the QD frequency (marked by the vertical dashed line in Fig.5.5(a)) and by controlling the voltage using a function generator. The modulated output was monitored using a single photon counting module (SPCM). A dual channel picosecond time analyzer(PTA) had its start channel connected to the sync of the function generator and the stop channel connected to the SPCM. The time delay between the start and stop events was recorded in a histogram that resembles the temporal profile of the modulated laser beam. We performed experiments at 150MHz modulation speed using a 5-10V sine wave. To minimize the amount of screening due to coherently excited carriers and thus allow device operation under 10V, the laser power coupled into cavity was $\sim 10pW$. The experimental results are shown in Fig.5.5 (b) that indicate a 150MHz signal modulation with an on/off ratio of 1.3:1 (limited by the attenuation in the transmission line). Attempts to drive the system at higher frequencies were not successful because the chip was not connected to a high speed transmission line in the cryostat.

The performance of optoelectronic switches is characterized by: bandwidth, on/off ratio, maximum intensity of input signal, and energy required per switching operation. When evaluating the maximum switching speed of this device, one needs to take into account both the electronic timescale (τ_{el}) set by the time it takes to deplete the carriers, and the optical timescales τ_{opt} set by $2\pi/g$, $2\pi/\kappa$ and $2\pi/\gamma$. Since the dimensions of the device are on the order of $1\mu m$, $\tau_{el} < 1ps$ and thus much

shorter than τ_{opt} which is on the order of 10ps. For the case of InAs QDs in photonic crystals resonators, where $g, \kappa >> \gamma$ (i.e. strong coupling regime or high Purcell factor regime), the maximum bandwidth is limited to $min(g/\pi, \kappa/\pi)$ in the strong coupling regime and $g^2/(\pi\kappa)$ in the weak coupling regime. A simulation of the on/off ratio as a function of the driving frequency is shown in Fig.5.5(c). The QD/cavity coupling rate and the shift of the QD resonance were set to $g/2\pi = 20GHz$ and $\delta/2\pi = 5GHz$, and the cavity decay rate was varied from $\kappa = 20GHZ$(onset of strong coupling) to $\kappa = 60GHz$(weak coupling). As seen from Fig.5.5(c), for the device discussed here ($\kappa = 40GHz$), the maximum bandwidth should theoretically exceed $\sim 10GHz$. So far, the shortest measured lifetime for this type of cavity/QD system was $\tau_{min} \sim 17ps$[63], corresponding to a switching speed of $1/(2\pi\tau_{min}) \sim 10GHz$. The maximum input intensity that can be switched is fundamentally limited by the QD saturation. For QDs coupled to photonic crystals, the saturation occurs at power levels corresponding to one photon in the cavity per modified QD lifetime τ_{QD}. The device under discussion operates in the strong coupling regime, so the QD lifetime is on the same order of magnitude as the cavity lifetime $\tau_{QD} \sim \tau_{cav} \sim 2ps$, implying a maximum operating power of $I_{max} \sim 100nW$.

To obtain the maximum operation speed reported in Fig.5.5(c), the system was modeled using the Quantum Optics Toolbox [70]. The master equation describing a QD (lowering operator $\sigma = |g\rangle\langle e|$) coupled to a cavity mode (with annihilation operator a) is given by

$$\frac{d\rho}{dt} = -i[H,\rho] + \frac{\kappa}{2}(2a\rho a^\dagger - a^\dagger a\rho - \rho a^\dagger a) + \frac{\gamma}{2}(2\sigma\rho\sigma^\dagger - \sigma^\dagger\sigma\rho - \rho\sigma^\dagger\sigma) + \frac{\gamma_d}{2}(\sigma_z\rho\sigma_z - \rho) \quad (5.1)$$

where γ, κ and γ_d accounts for QD population decay, cavity population decay and QD pure dephasing; $\sigma_z = [\sigma^\dagger, \sigma]$. H is the hamiltonian of the system without considering the losses and is given by (in Rotating Wave Approximation)

$$H = (\omega_c - \omega_l)a^\dagger a - (\omega_a - \omega_l)\sigma_z + ig(\sigma a^\dagger - a\sigma^\dagger) + E\sqrt{\kappa}(a + a'), \quad (5.2)$$

where ω_c,ω_a and ω_l are cavity resonance, QD resonance and driving laser frequency respectively. E is the amplitude of the driving field. When this system behaves as a

switch then E and ω_l are the input signal amplitude and frequency. As the electric field causes the QD resonance to shift, we assume $\omega_c = \omega_l$ and $\omega_d = \frac{1}{2}\Delta\omega_0 sin(\Omega t)$ where Ω is the frequency of the modulation and ω_0 is the amplitude of the modulation.

For most of the modern optoelectronic devices, the energy required per switching operation is the most important parameter. In this case, where the metallic electrode was placed laterally, the device can be modeled as a capacitor with the following dimensions: width $w \sim 1\mu m$, thickness $t \sim 100nm$ and length $L \sim 1\mu m$. This gives a capacitance $C \sim \epsilon_0\epsilon_r wt/L \sim 10^{-17}F$ ($\epsilon_r \sim 13$) and a switching energy of $CV^2/2 \sim 1000eV \sim 100aJ$ when the switching voltage is a $V \sim 5V$. This translates into a operating power of $\sim 1\mu W$ at $10GHz$. Since the energy consumption has a quadratic dependence on the applied voltage, the operating power can be lowered by at least two orders of magnitude by bringing the electrode closer to the QD or by using samples of higher purity to increase the extent of the depletion layer for a given bias voltage. These energy scales are on the same magnitude to those employed in all optical switching devices where the challenge is to build devices that operate at $100aJ$ per operation.

At the most fundamental limit, the active volume responsible for the switching action is the QD itself. If by some method one could only deplete the QD, the switching energy would be limited by the capacitance of the QD itself. For an InAs QD, with a volume of $\sim 1nm \times 5nm \times 5nm$, the minimum capacitance is $10^{-19}F$, thus setting the switching energy to $\sim 1eV$ considering a switching voltage of 1V. However, depleting such a small volume is technologically very challenging.

In conclusion, we demonstrate an electro-optical switch based on a single emitter coupled to a ultra-small volume optical resonator. The fundamental limit of the switching speed exceeds $10GHz$, and it can operate at light intensities as high as $100nW$. The energy required per switching operation is on the order of $\sim 100aJ$. While in terms of the speed, bandwidth and switching intensity the switch presented in this chapter is comparable in performance with state of the art devices, in terms of its energy consumption it sets a new standard. This type of device is an essential building block for future optoelectronic devices for classical and quantum information science. In a nanophotonic network for classical information processing it can serve as

an electro-opto switch. For quantum information science devices, it can be used for routing photons, fine and fast tuning of the QD resonance, or deterministic charging of the QD.

For optoelectronic applications it is interesting to implement the single quantum dot switch in an integrated device where the input/output coupling into the cavity is done via optical waveguides. In Fig.5.6, we show a device of this kind, with a waveguide-coupled cavity and electrical control.

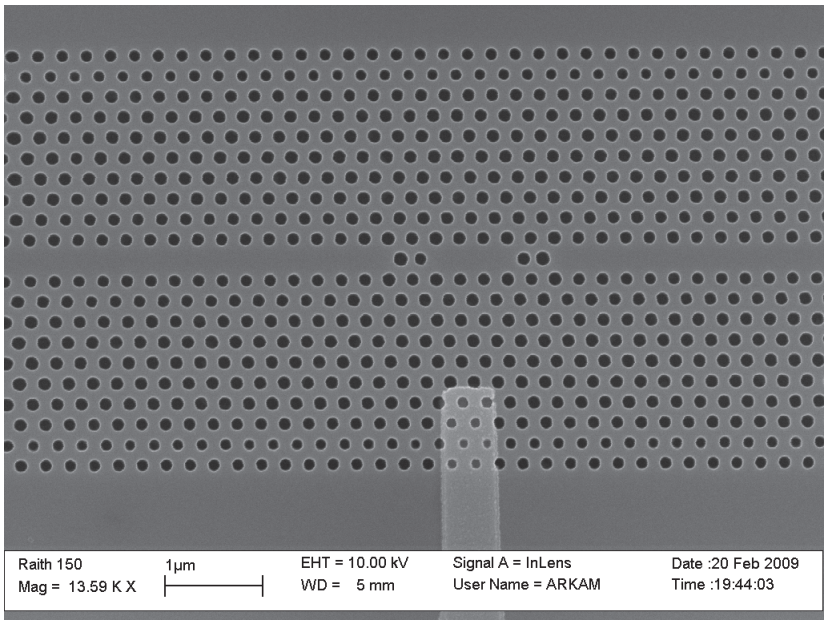

Figure 5.6: Waveguide-coupled cavity with electrical control for single quantum dot electro-optical switching.

Chapter 6

Conclusion and Future Directions

6.1 Summary of Results

As discussed in detail in this dissertation, my PhD work has been focused on the study of GaAs photonic crystals with coupled InAs quantum dots. We achieved significant progress both in the study of the fundamental properties of these systems, and in developing technologies that hopefully will be found some day in working devices for classical and quantum information processing.

Regarding the study of the fundamental properties of cavities with coupled QDs, we have performed the first experiments on coherent probing of these systems [19], thus showing that a single emitter in a cavity can be used to control the transmission of a light beam. This represents an ultimate limit of optical switching that occurs at ultra-low light intensities corresponding to an average photon number in the cavity much less than one. The system exhibits large optical nonlinearities and saturates once the energy accumulated in the cavity approaches one photon per cavity lifetime [19]. We have used this nonlinearity to control the phase of a signal beam reflected from the cavity by up to $\pi/4$ using a control beam as discussed in Ref. [20]. This type of control is essential for control phase shift gates required for some of the optical quantum information science devices [13].

One of the most fundamental experiments that we performed using strongly coupled cavity/QD systems was to probe photon blockade and photon induced tunneling

[21]. These are nonlinear optical phenomena at the single photon level that occur because of the anharmonicity of the Jaynes-Cummings spectrum of the energy eigenstates of the strongly coupled system. Unlike the dipole-induced transparency and the control phase shift experiments that can be explained using semi-classical theories, photon blockade and photon induced tunneling can only be explained by considering the full quantum description of the system.

The technological developments in the photonic crystal/QD platform have been motivated either by our fundamental experiments or by the future vision to develop an integrated platform for optical information processing. One of the main difficulties in achieving integrated devices is the inhomogeneous broadening of quantum dots and the lack of precise control of the cavity resonance due to imperfections in the fabrication process. To overcome these difficulties we developed a set of tuning techniques that rely on local control of the temperature and index of refraction [48, 95, 51]. These techniques allow for control of the cavity and QD resonance for a few nm (thousands of GHz) and are sufficient for some initial proof of concept experiments involving a few QDs. Another challenge is the design of photonic crystal devices such that light can be efficiently controlled on the chip level. To this end we have designed efficient methods to couple waveguides and photonic crystal cavities [72] and performed the first experiments integrating cavities, waveguides, quantum dots, tuning elements and coherent probing [76].

From a practical point of view it is very desirable to electrically control quantum dots coupled to cavities. This would enable fast electro-optic switches that can operate at ultra-low energies per switching operation. We have performed the first experiments with this type of device where a strongly coupled QD was controlled via an electric field created in the depletion region of a Schottky contact electrode located in the close vicinity of the cavity/QD system. The system has been used to perform electro-optic switching of laser beams up to speeds as high as 150MHz [96].

6.2 Future Directions

Even though the promise of combining QDs and photonic crystals is that an integrated platform could be developed, no experiments on multiple quantum dots have been performed so far. One of the next goals for the research in this field is performing experiments involving multiple (at least two) quantum dots located on the same chip. This could be done using the local tuning techniques but may also require precise alignment of photonic crystal cavities [30] on pre-positioned quantum dots [97]. One of the first experiments of this kind could be the interference of two photons coming from QDs located on the same chip, or cascading two electro-optic switches.

For quantum information science it is essential that the cavities are combined with QDs where coherent control of their levels can be achieved. This would probably be achieved in the near future given the recent progress in complete optical control of the electron spin in QDs[16]. Moreover, several other possibilities for single QD manipulation using two photon processes have been proposed by our group [98, 99] and they will be implemented in the near future.

For classical applications, one of the future directions is to increase the speed of the electro-optic switching up to the decay rate of the optical system (10 GHz). One of the concerns in doing electro-optic switching using strongly coupled systems is the limited on:off ratio ($\sim 2:1$) experimentally demonstrated so far. At the moment it is not clear what is limiting the on:off ratio and whether or not this is a fundamental limitation. One possibility is that the limitation is imposed by the quantum dot dephasing [63]. Another direction of research for optical signal processing is the development of devices with multiple optical ports interconnected via highly non-linear devices with single QDs in cavities.

The research field of nano-photonics is extremely dynamic and the most promising research direction changes fast depending on the latest achievements in the field. This has happened several time during my PhD and this trend will most probably continue in the Vuckovic group. I am looking forward with great excitement at the research that will be done by the students who will continue the solid state quantum optics project in the group.

Appendix A

Fabrication of photonic crystals in GaAs

GaAs photonic crystal devices were fabricated via a process consisting of electron beam lithography, dry plasma etching and under-etching in hydrofluoric acid. The photonic crystals were fabricated on GaAs membranes. A typical layer structure for the GaAs wafers that we used is shown in is shown in Fig.A.1. The wafer in Fig.A.1 has a membrane with doped layers that we used to electrically contact the sample. In most of the experiments that we performed, we used undoped membranes.sisting of electron beam lithography, dry plasma etching and under-etching in hydrofluoric acid. The photonic crystals were fabricated on GaAs membranes. A typical layer structure for the GaAs wafers that we used is shown in is shown in Fig.A.1. The wafer in Fig.A.1 has a membrane with doped layers that we used to electrically contact the sample. In most of the experiments that we performed, we used undoped membranes.

The fabrication procedure followed the following steps:

1. Sample preparation

   (a) Spin wafer with electron beam resist (PMMA 4.5% 950K) at 4500rpm for 40sec to obtain a desired thickness of $\sim 300nm$. Stick the wafer on blue tape before spinning to keep the back of the wafer clean.

   (b) Bake wafer at 200C for 2 minutes (remove blue tape before baking).

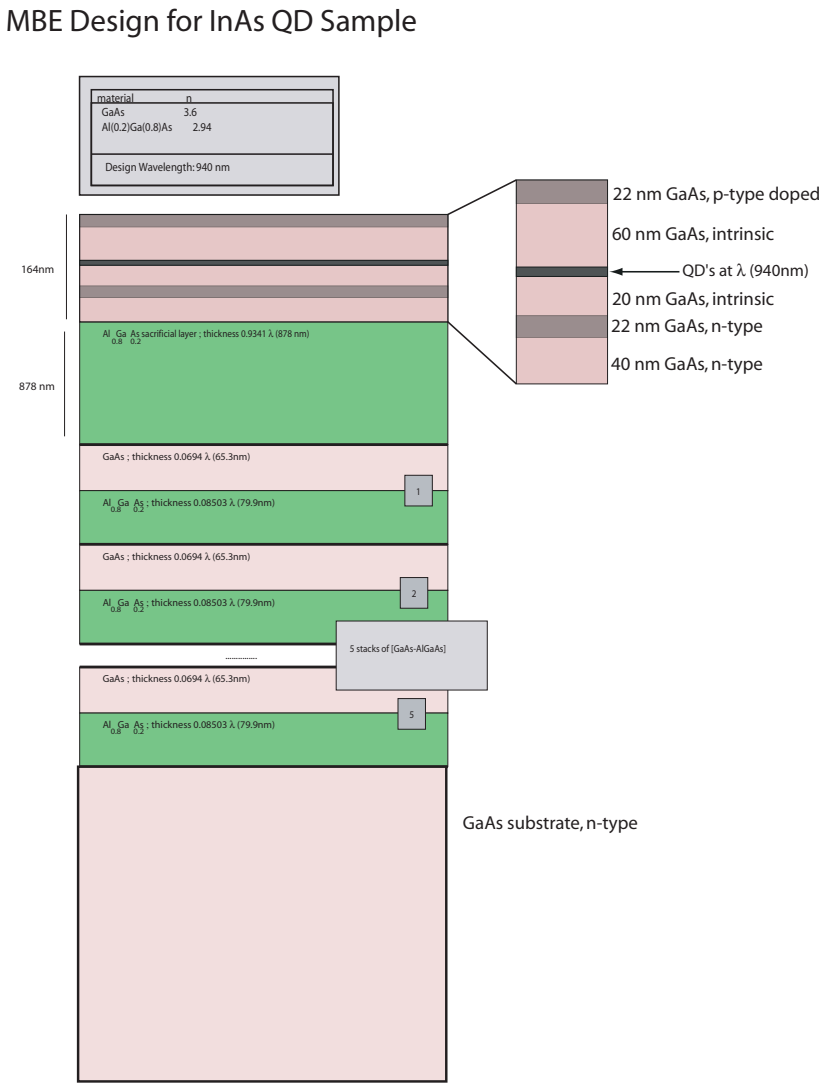

Figure A.1: The design of one of the wafers we used to fabricate photonic crystals. For this particular wafer design the membrane had p and n doped layers that can be used to make electrical contacts to the wafer.

(c) Cleave small pieces ($\sim 5mm \times 2mm$) for electron-beam lithography.

2. E-beam lithography

(a) Design photonic crystal e-beam mask. The L3 cavities that we used for our experiment were designed on a triangular PC lattice with lattice constant $a = 246nm$ and hole radius $r = 60nm$. The lateral holes of the cavity were shifted outward by $37nm$

(b) Use electron-beam lithography (Raith 150 e-beam system) to write the photonic crystal devices. We used the following exposure parameters: $10\mu m$ aperture, dose $140\mu C$, area step size of $3.2nm$

(c) Develop the chip for 40sec in a solution of 3:1 IPA:MIBK then rinse in IPA for 30sec.

3. Dry Plasma Etching

(a) The recipe for dry plasma etching has changed several times during the years of my PhD, generally after repairs had been done to the machine (Plasma Quest). Here I report the recipe we used to fabricate A53.

(b) Attach the chip on a Si wafer using a small drop of PMMA and bake at 90C for 1min. Attaching the chip in this way ensures consistent thermal contact of the GaAs chip to the carrier wafer.

(c) We used the following recipe to etch the chip:

(d) After etching, clean the chip by sonicating in acetone for 1min, then rinse in IPA.nicating in acetone for 1min, then rinse in IPA.

4. Undercutting

(a) Before undercutting leave the chip in citric acid (1mol) for 1 minute

(b) Prepare one beaker with hydrofluoric acid (6%) and one beaker with water

(c) Dip sequentially the chip in HF($\sim 3sec$) and water($\sim 3sec$) about 5 times and then put the chip in citric acid for 1 min.

(d) Rinse the chip in acetone then IPA for 1 minute each.

	Step 1	Step 2 (ignition)	Step 3
Ar (sccm)	15	15	15
BCl_3 (sccm)	10	10	10
Cl_2 (sccm)	2.5	2.5	2.5
Pressure (mTorr)	2	2	2
ECR power (W)	0	400	200
RF power (W)	0	47	47
He pressure (mTorr)	10	10	10
Temperature (C)	13	13	13
time (s)	70	until ignition	220

Table A.1: Plasma Quest etching recipe

Appendix B

Cross-Polarized Reflectivity Measurements

The content of this appendix is based on the writeup for a lab class experiment (EE234) that I set up while at Stanford. It should be very instructive for anyone who wishes to set up reflectivity measurements in the lab. It includes an educative prelab, all the parts used for the experiment and the procedure on how to perform reflectivity measurements. The experiment was set to probe cavities operating at 1550nm but the setup is almost identical for near infrared.

B.1 Preparatory problems: Cross-polarized reflectivity measurement

1. A polarizing beam splitter reflects vertically ($|V\rangle$) polarized light and transmits horizontally ($|H\rangle$) polarized light as shown in Fig.B.1. In this problem, $|V\rangle$-polarized means perpendicular to the plane of the figure, and $|H\rangle$ means polarized in the plane of the figure and perpendicular to the direction of propagation. Consider the setup in Fig.B.1, composed of a polarizing beam splitter, a mirror and a photodetector. A laser beam with intensity I_0 and polarized at angle θ_{in} with respect to $|V\rangle$, is incident on the beam splitter as shown in in

Fig.B.1. What is the intensity detected by the photodetector as a function of θ_{in} and I_0?

Notice that in this setup, the light incident on the mirror is $|V\rangle$ polarized, and the light detected by the photodetector is $|H\rangle$ polarized. In other words, the light incident on the mirror (or any other object replacing that mirror) is cross-polarized with the light detected at the output. For this reason, the setup is called a cross-polarized reflectivity setup.

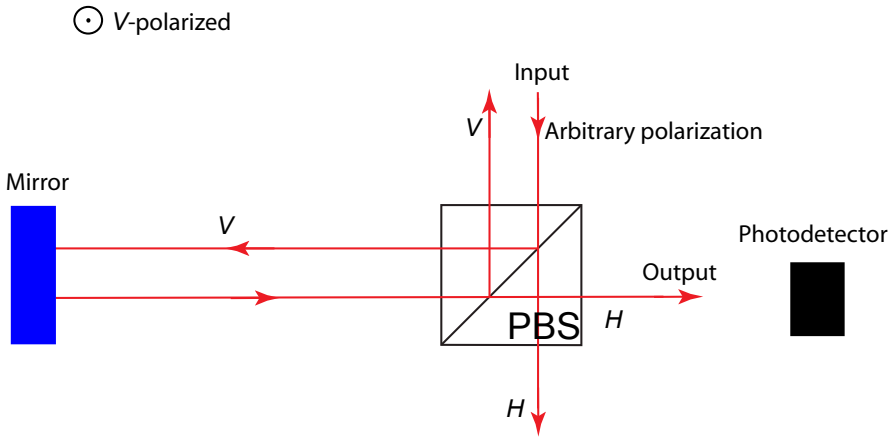

Figure B.1: Schematic of the cross-polarized reflectivity measurement.

2. A linear polarizer (P1) whose polarization axis makes an angle θ_p with the $|V\rangle$ axis is placed in between the PBS and the mirror as shown in Fig.B.2. Set the input polariation to $\theta_{in} = 0$ ($|V\rangle$ - polarized). What is the intensity detected by the photodetector as a function of I_0 and θ_p? Answer the same question if in place of the polarizer you put a half wave plate (HWP) whose fast axis makes an angle of θ_{HWP} with $|V\rangle$? A good tutorial on how half-wave plates and quarter wave plates work can be found on the Newport website (http://www.newport.com/servicesupport/Tutorials/default.aspx?id=118).

3. Replace the linear polarizer and the mirror with a linearly polarized optical resonator as shown in Fig.B.3. This type of resonator only transmits light of a specific frequency and specific linear polarization, all the other light being reflected. Let's orient the resonator polarization axis at say, 45^o with respect

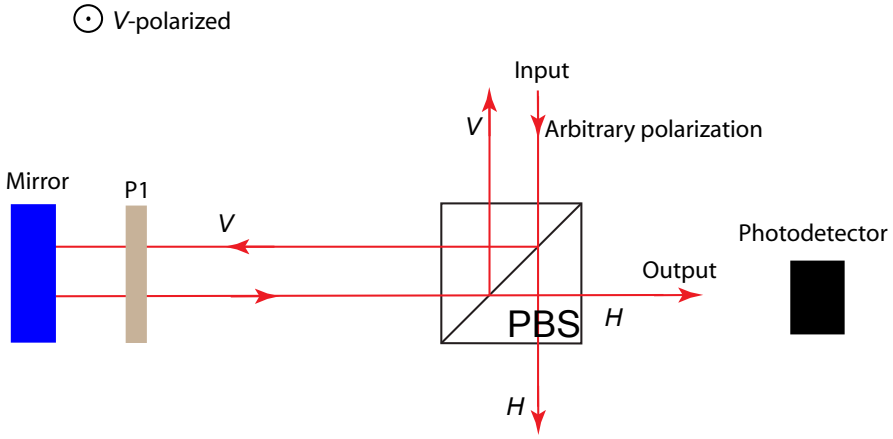

Figure B.2: Schematic of the cross-polarized reflectivity measurement.

to $|V\rangle$. To make things easier we can define a new coordinate system ($|+45\rangle = 1/\sqrt{2}(|V\rangle + |H\rangle), |-45\rangle = 1/\sqrt{2}(|V\rangle - |H\rangle)$), rotated by 45^o with respect to the initial coordinate system ($|V\rangle, |H\rangle$). The linearly incident light, that is $|V\rangle$ polarized, can be decomposed in a new basis as $|V\rangle = \frac{1}{\sqrt{2}}(|45\rangle + |-45\rangle)$. The $|-45\rangle$ component is polarized orthogonal to the resonator and fully reflects back with a (-1) phase factor. The $|45\rangle$ component is polarized collinear with the resonator so it reflects back with reflection coefficient $r(\lambda)$, where λ is the frequency of the light. The reflection coefficient $r(\lambda)$ is defined for the electric field, not the intensity (intensity reflects as $|r(\lambda)|^2$). So, while the incident is $|V\rangle$ polarized, the reflected light is polarized as $r(\lambda)\,|45\rangle - |-45\rangle$. What is the electric field vector ($E_{out}(r)$) transmitted through the beamsplitter and incident on the photodetector? What is the intensity measured by the photodetector as a function of $r(\lambda)$?

4. For a resonator, the reflection coefficient is:

$$r(\lambda) = \frac{1}{2iQ(1-\lambda/\lambda_0)+1} - 1, \tag{B.1}$$

where Q is the quality factor of the resonator and λ_0 is its resonance wavelength. Using this expression, derive a formula for the electric field ($E_{out}(\lambda)$) and the

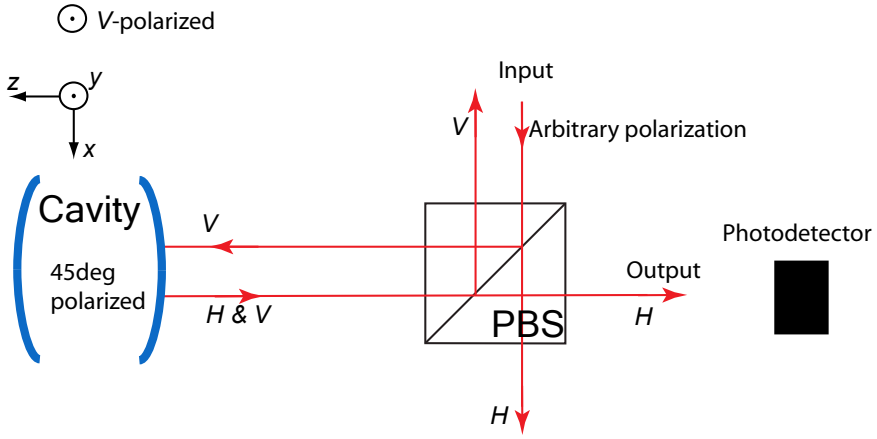

Figure B.3: Schematic of the cross-polarized reflectivity measurement.

intensity detected by the photodetector ($I_{out}(\lambda)$) as a function of λ. Plot this expression for the case where the wavelength of the resonator is $\lambda_0 = 1550$nm and the quality factor is $Q = 10000$.

5. Because of the imperfections in the experimental setup (as not perfect cross-polarization), at the output port you can also get light that is not coupled at all to the cavity. This light has some amplitude and some phase, say $Ae^{i\phi}$. At the output you now have a field that looks like the previously computed $E_{out}(\lambda)$ plus the additional term: $E_{out}^{real} = E_{out}(\lambda) + Ae^{i\phi}$. Plot the intensity of the light at the output for $A = 1/\sqrt{2}$ and $\phi = (0, 5\pi/8, \pi)$ (these values are going to give you some typical spectra you will measure during the experiment). Notice how the spectra change with the phase ϕ. You are strongly encouraged to explore how the output changes with various values of A and ϕ.

6. Consider the same situation as in Part.4 and set the probe frequency at the cavity resonance ($\lambda = \lambda 0$). A HWP is placed in between the beam splitter and the resonator. How does the intensity you detect at the output depend on the angle between the fast axis of the HWP and the $|V\rangle$ direction?

7. Consider the same situation as in Part.4 and set the probe frequency at the cavity resonance ($\lambda = \lambda 0$). How does the intensity you detect at the output

change when you rotate the resonator? Give your answer in terms of the angle between the polarization axis of the resonator and the $|V\rangle$ direction.

B.2 Introduction

The linear three hole photonic crystal cavity has aigenmodes that are linearly polarized, with the fundamental mode polarized on a direction perpendicular to the cavity axis (the line that joins the centers of the three missing holes). Fig.B.4(a) shows a scanning electron microscope(SEM) image of a linear three hole defect cavity, and Fig.B.4(b) shows how the electric field profile of the fundamental mode of this cavity looks like. The polarization of the light leaking from this cavity in the z direction (see drawn coordinate system), is y polarized.

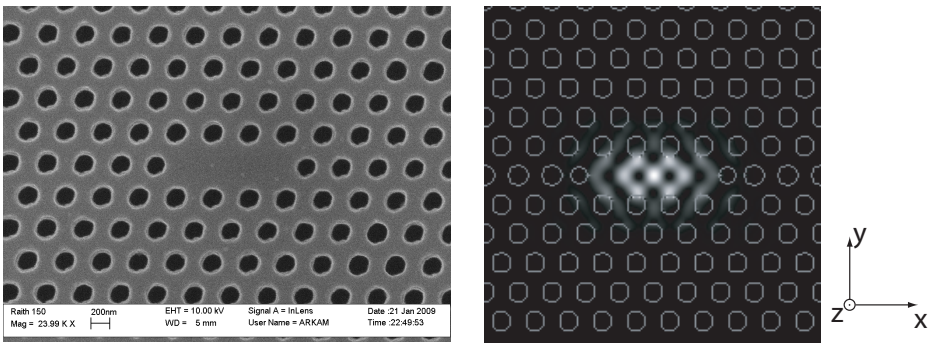

Figure B.4: (a) SEM image of a linear three hole defect cavity similar to the one you will measure. (b) Simulation of the electric field intensity of the fundamental cavity mode. The polarization of the light leaking from this cavity in the z direction (see drawn coordinate system), is y polarized.

B.3 Experimental Setup

The experimental setup is shown in Fig.B.5. Please read the figure caption for an explanation on how the setup works.

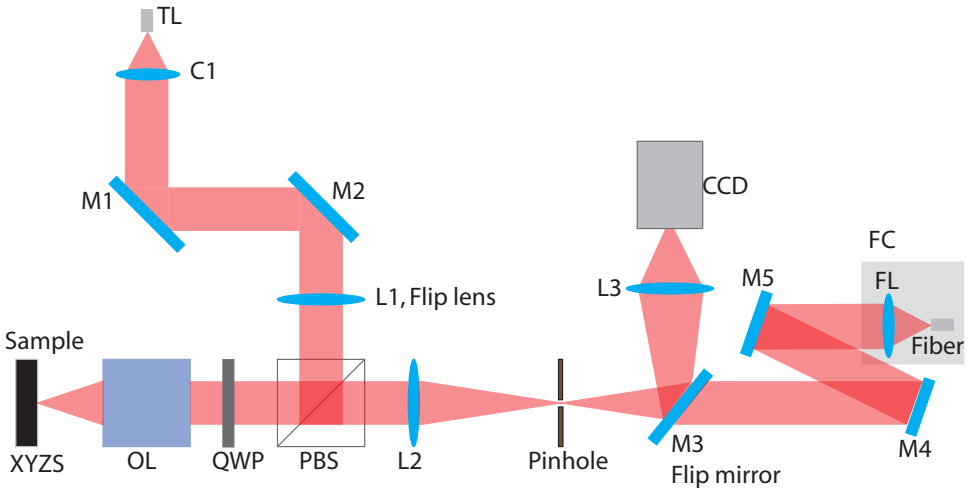

Figure B.5: Schematic of the experimental setup. The fiber carrying the light from the tunable laser (TL)is coupled into a collimator (C1), then mirrors M1 and M2 are used to align the beam onto the polarizing beam splitter (PBS). The light reflected from the PBS is focused on the sample using an objective lens (OL). The sample is mounted on a XYZ stage (XYZS) The same OL collects the laser light reflected from the cavity. Only the light that is horizontally polarized gets transmitted through the PBS toward the output port. On the output part, the lens L2 is used to create a real image of the sample on the pinhole, and lens L3 is used to re-image the pinhole and the sample image on the camera. The flip mirror M3 is used to redirect the output either at the camera or into a fiber coupler. Mirrors M4 and M5 align the beam into the fiber coupler. The flip lens L1 is used to de-collimate the input beam of light such that when the sample is in the focal plane of the objective lens the laser is not focused on the cavity. This helps with the sample imaging.

B.4 Experimental Procedure

1. First you need to image the chip so you know what cavity to probe. Turn on the laser and flip lens L1 into the beam path. The chip is mounted on a XYZ stage so you can move it. The X and Y coordinates are in the plane of the chip. The Z coordinate is perpendicular to the chip, and along the axis of the objective lens. Change the Z axis to bring the chip in focus. On the camera you should see an image of the chip. Moving the stage in the X and Y directions, identify the cavity that you want to probe and place it such that the cavity (i.e. the middle of the photonic crystal structure) is in the middle of the screen. Make sure that the cavity polarization is not oriented along one of the polarization direction of the polarizing beam splitter, such that the reflectivity measurement can be performed.

2. Close the aperture to its minimum size and observe it on the screen. Position the cavity as close as possible to the center of the aperture. Tune the laser to the cavity resonance (assuming you know it from a photoluminescence measurement). Now you should see the cavity as a bright spot because the laser couples to it. If you don't see it as a bright spot then change the Z axis of the stage until you see this. Move the stage in X and Y directions such that the bright spot of the cavity is exactly in the middle of the aperture. For better coupling you should flip the lens L1 out of the beam path and try to couple the focused laser into the cavity. Optimize the coupling by changing Z and moving mirror M2 until you make the cavity as bright as possible. Close the aperture to isolate only the bright cavity spot. Now you want to measure how much of the coupled power you are collecting at the output. The output signal is coupled into a fiber that is connected to a powermeter. To direct the light to the powermeter, flip the mirror M3. Now you are ready to measure the cavity resonance.

3. The scan is done by scanning the laser wavelength and monitoring the coupled power using a powermeter. The analog output of the powermeter is sent to an oscilloscope. Both the oscilloscope and the laser are controlled via GPIB using

Matlab. To collect the data you will use the matlab script shown in B.5. You can set several parameters in the script: the start wavelength (*lambda_start*), the number of steps (*n_steps*) and the step size (*lambda_step*). When you set these parameters keep in mind that the script runs at about 2 seconds per step. I suggest that you start with n_steps=100 so you only wait a couple of minutes per scan. Beside the initialization of the GPIB devices, the code is basically a *for* loop in which you set the laser wavelength, then wait for a few seconds for the wavelength to change, then read the average voltage measured by the scope, which is proportional to the power incident on the powermeter. Set the scanning parameters to do a scan from 1511nm to 1513nm. Run the matlab code. The code will also plot and save the data automatically. Now you should get a spectrum showing the cavity resonance.

To compensate for the phase of the signal uncoupled to the cavity, mount a quarter wave plate in between the PBS and OL (closer to the PBS). Look at the camera and rotate the QWP get a good contrast between the bright spot on the cavity and the reflected light from the photonic crystal. Aquire a new spectrum.

Fit the spectra you obtained with and without the QWP with the formula you derived in the prelab for $E_{out}^{real} = E_{out}(\lambda) + Ae^{i\phi}$ and report the fitting parameters.

4. Insert a half wave plate in between the beam splitter and the objective lens (you can keep the QWP). Tune the laser at the cavity resonance and monitor the cavity coupling on the camera. **What happens when you rotate the half wave plate?** Direct the output toward the powermeter. Record the power measured by the powermeter while rotating the half wave plate. First see at what angle of the half wave plate the output signal is maximized, then twist the half wave plate by 90 degrees in increments of 5 degrees. Record the power after each 5 degree increment. **How do you expect the output power to change with the angle of the half wave plate? Does the output follow the same dependence as you computed in Problem.6 of the**

prelab? Explain any similarities or differences and fit the data with the formula you obtained in Problem.6

B.5 Matlab code

```
%%Code to set the laser wavelength and to read from the oscilloscope for
%%reflectivity measurements
%%Written by Andrei Faraon 02/25/2009



clear all
close all
%this are the start wavelength, the step size and the number of steps
lambda_start=1511;
lambda_step=0.05;
n_steps=50;

%this is the name of the file where you will save the data
file_name='reflectivity.txt'

%this variable stores the voltage from the scope
V=[];

%this commands initialize the GPIB connection to the oscilloscope and the laser.
%The GPIB ports usually are 7 for the oscilloscope and 20 for the laser.
sc = gpib('ni',0,7);
fopen(sc)

las = gpib('ni',0,20);
fopen(las)
```

```
%This tests if the oscilloscope and the laser are connected via GPIB
fprintf(las,'*IDN?')
idn_las = fscanf(las)
fprintf(sc,'*IDN?')
idn_sc = fscanf(sc)


%fprintf(las,'VI_ATTR_TMO_VALUE,20000')

%This for loop sets the laser wavelength and reads the voltage on the
%oscilloscope.
ii=1;
jj=1;

for ii=1:n_steps
    ii
    %this is the laser wavelength
    lambda(ii)=(lambda_start + lambda_step*ii);
    %here the wavelength is set on the laser
    fprintf(las,['SOURCE1:WAV ',num2str((lambda_start + ...
    ...lambda_step*ii)*10^-9,'%11.7g'),''])
    %Wait a second for the laser to set the wavelength
    pause(1)
    %measure the reading of the oscilloscope
    fprintf(sc,'MEAS:VAV?')
    V(ii) = str2num(fscanf(sc));

end

%close the GPIB connections
fclose(las)
```

```
fclose(sc)

%plot the data
figure
plot(lambda,V)
xlabel('\lambda [nm]')
ylabel('R')

%save the data
save(file_name,'lambda','V','-ASCII')
```

B.6 Parts used in the experimental setup

Part acronym	Name and description	Part number and manufacturer
TL	Tunable laser - 1465nm-1575nm	Agilent 81989A mounted in 8163B mainframe
C1	Mounted fiber collimator 1050-1600nm	Thorlabs CFC-2-C mounted in AD9.5F and KM100
L1	Defocusing lens - 75mm focal length	Thorlabs, LA1608-C BK7, mounted in NewFocus 9897 flip mount
L2	Focusing lens - 400mm focal length	Thorlabs, LA1172-C BK7
L3	Re-focusing lens - 60mm focal length	Thorlabs, LA1134-C BK7
M1 - M4	Silver coated mirrors	Thorlabs PF10-03-P01 mounted in KM100 and other mirror mounts
PBS	Broadband Polarizing Cube Beamsplitter, 25.4mm, 1200-1600nm	Newport 10FC16PB.9
OL	Objective lens	NT46-405, MITUTOYO OBJ PLAN NIR 50X, from Edmund Optics
XYZS	XYZ translation stage	Thorlabs
CCD	CCD camera, near infrared	NT56-567 NEAR IR CAMERA, from Edmund Optics
FL	Focusing lens for fiber coupling	Newport, MV-10X Valumax Objective Lens, 10x, 0.25 NA, 15.8mm Focal Length, 8.0mm Clear Aperture
Fiber coupler	Fiber coupler	Newport, F-91-C1-T Multimode Fiber Coupler, Connectorized Fiber Positioner
HWP	Half wave plate for 1550nm	Thorlabs WPH05M-1550 mounted in Thorlabs RSP1
Fibers	Input/output fibers	Thorlabs, TP3-SMF28-FC-2

Table B.1: Parts used in the experiment

Bibliography

[1] K. Vahala, "Optical microcavities," *NATURE*, vol. 424, pp. 839–846, AUG 14 2003.

[2] E. Ozbay, "Plasmonics: Merging Photonics and Electronics at Nanoscale Dimensions," *Science*, vol. 311, no. 5758, pp. 189–193, 2006.

[3] S. Noda, "Recent Progresses and Future Prospects of Two- and Three-Dimensional Photonic Crystals," *Journal of Lightwave Technology*, vol. 24, pp. 4554–4567, December 2006.

[4] D. A. B. Miller, "Device requirements for optical interconnects to silicon chips," *Proc. IEEE Special Issue on Silicon Photonics*, 2009.

[5] Q. Xu, S. Manipatruni, B. Schmidt, J. Shakya, and M. Lipson, "12.5 gbit/s carrier-injection-based silicon micro-ring silicon modulators," *Opt. Express*, vol. 15, no. 2, pp. 430–436, 2007.

[6] A. Liu, L. Liao, D. Rubin, H. Nguyen, B. Ciftcioglu, Y. Chetrit, N. Izhaky, and M. Paniccia, "High-speed optical modulation based on carrier depletion in a silicon waveguide," *Opt. Express*, vol. 15, no. 2, pp. 660–668, 2007.

[7] A. Liu, R. Jones, L. Liao, D. Samara-Rubio, D. Rubin, O. Cohen, R. Nicolaescu, and M. Paniccia, "A high-speed silicon optical modulator based on a metal-oxide-semiconductor capacitor," *NATURE*, vol. 427, pp. 615–618, FEB 12 2004.

[8] Q. Xu, B. Schmidt, S. Pradhan, and M. Lipson, "Micrometre-scale silicon electro-optic modulator," *NATURE*, vol. 435, pp. 325–327, MAY 19 2005.

[9] Q. Xu, D. Fattal, and R. G. Beausoleil, "Silicon microring resonators with 1.5-μm radius," *Opt. Express*, vol. 16, no. 6, pp. 4309–4315, 2008.

[10] J. I. Cirac, P. Zoller, H. J. Kimble, and H. Mabuchi, "Quantum State Transfer and Entanglement Distribution among Distant Nodes in a Quantum Network," *Physical Review Letters*, vol. 78, pp. 3221–24, Apr. 1997.

[11] L.-M. Duan and H. J. Kimble, "Scalable photonic quantum computation through cavity-assisted interactions," *Phys. Rev. Lett.*, vol. 92, p. 127902, Mar 2004.

[12] C. J. Hood, M. S. Chapman, T. W. Lynn, and H. J. Kimble, "Real-time cavity qed with single atoms," *Phys. Rev. Lett.*, vol. 80, pp. 4157–4160, May 1998.

[13] R. J. Thompson, Q. A. Turchette, O. Carnal, and H. J. Kimble, "Nonlinear spectroscopy in the strong-coupling regime of cavity qed," *Phys. Rev. A*, vol. 57, pp. 3084–3104, Apr 1998.

[14] D. Felinto, C. W. Chou, J. Laurant, E. W. Schomburg, H. D. Riedmatten, and H. J. Kimble, "Conditional control of the quantum states of remote atomic memories for quantum networking," *Nature Physics*, vol. 2, pp. 844–848, 2006.

[15] K. M. Birnbaum, A. Boca, R. Miller, A. D. Boozer, T. E. Northup, and H. J. Kimble, "Photon blockade in an optical cavity with one trapped atom," *Nature*, vol. 436, pp. 87–90, 2005.

[16] D. Press, T. D. Ladd, B. Zhang, and Y. Yamamoto, "Complete quantum control of a single quantum dot spin using ultrafast optical pulses," *NATURE*, vol. 456, pp. 218–221, NOV 13 2008.

[17] Charles Santori and Philippe Tamarat and Philipp Neumann and Jörg Wrachtrup and David Fattal and Raymond G. Beausoleil and James Rabeau and Paolo Olivero and Andrew D. Greentree and Steven Prawer and Fedor Jelezko and Philip Hemmer, "Coherent population trapping of single spins in diamond under optical excitation," *Physical Review Letters*, vol. 97, no. 24, p. 247401, 2006.

[18] J. J. Longdell, M. J. Sellars, and N. B. Manson, "Demonstration of conditional quantum phase shift between ions in a solid," *Phys. Rev. Lett.*, vol. 93, p. 130503, Sep 2004.

[19] D. Englund, A. Faraon, I. Fushman, N. Stoltz, P. Petroff, and J. Vuckovic, "Controlling cavity reflectivity with a single quantum dot," *Nature*, vol. 450, pp. 857–861, 2007.

[20] I. Fushman, D. Englund, A. Faraon, N. Stoltz, P. Petroff, and J. Vuckovic, "Controlled Phase Shifts with a Single Quantum Dot," *Science*, vol. 320, 2008.

[21] A. Faraon, I. Fushman, D. Englund, N. Stoltz, P. Petroff, and J. Vuckovic, "Coherent generation of non-classical light on a chip via photon-induced tunnelling and blockade," *Nature Physics*, vol. 4, pp. 859–863, NOV 2008.

[22] Y. Takahashi, H. Hagino, Y. Tanaka, T. Asano, and S. Noda, "High-q photonic nanocavity with a 2-ns photon lifetime," in *Conference on Lasers and Electro-Optics/Quantum Electronics and Laser Science Conference and Photonic Applications Systems Technologies*, p. QFO1, Optical Society of America, 2008.

[23] Z. Zhang and M. Qiu, "Small-volume waveguide-section high q microcavities in 2d photonic crystal slabs," *Opt. Express*, vol. 12, no. 17, pp. 3988–3995, 2004.

[24] K. Nozaki, S. Kita, and T. Baba, "Room temperature continuous wave operation and controlled spontaneous emission in ultrasmall photonic crystal nanolaser," *Opt. Express*, vol. 15, no. 12, pp. 7506–7514, 2007.

[25] J. Vučković, M. Lončar, H. Mabuchi, and A. Scherer, "Design of photonic crystal microcavities for cavity qed," *Phys. Rev. E*, vol. 65, p. 016608, Dec 2001.

[26] Y. Akahane, T. Asano, B.-S. Song, and S. Noda, "High-Q photonic nanocavity in a two-dimensional photonic crystal ," *Nature*, vol. 425, pp. 944–947, Oct. 2003.

[27] D. Englund, D. Fattal, E. Waks, G. Solomon, B. Zhang, T. Nakaoka, Y. Arakawa, Y. Yamamoto, and J. Vučković, "Controlling the Spontaneous Emission Rate of

Single Quantum Dots in a Two-Dimensional Photonic Crystal," *Physical Review Letters*, vol. 95, July 2005.

[28] D. Englund, I. Fushman, and J. Vučković, "General Recipe for Designing Photonic Crystal Cavities," *Optics Express*, vol. 12, pp. 5961–75, Aug. 2005.

[29] P. Michler, *Single quantum dots: Fundamentals, Applications, and New Concepts*. Springer-Verlag: Topics in Applied Physics, 2003.

[30] A. Badolato, K. Hennessy, M. Atatüre, J. Dreiser, E. Hu, P. Petroff, and A. Imamoglu, "Deterministic Coupling of Single Quantum Dots to Single Nanocavity Modes," *Science*, vol. 308, pp. 1158 – 1161, May 2005.

[31] S. M. Thon, M. T. Rakher, H. Kim, J. Gudat, W. T. M. Irvine, P. M. Petroff, and D. Bouwmeester, "Strong coupling through optical positioning of a quantum dot in a photonic crystal cavity," *Applied Physics Letters*, vol. 94, no. 11, p. 111115, 2009.

[32] J. Vuckovic, C. Santori, D. Fattal, M. Pelton, G. Solomon, and Y. Yamamoto, *in Optical Microcavities, edited by K. Vahala*. Singapore: World Scientific, 2004.

[33] E. M. Purcell, "Spontaneous emission probabilities at radio frequencies," *Physical Review*, vol. 69, p. 681, 1946.

[34] E. Waks and J. Vučković, "Dipole induced transparency in drop-filter cavity-waveguide systems," *Physical Review Letters*, vol. 80, April 2006.

[35] A. Auffeves-Garnier, C. Simon, J.-M. Gerard, and J.-P. Poizat, "Giant optical nonlinearity induced by a single two-level system interacting with a cavity in the purcell regime," *Physical Review A (Atomic, Molecular, and Optical Physics)*, vol. 75, no. 5, p. 053823, 2007.

[36] K. Hennessy, A. Badolato, M. Winger, D. Gerace, M. Atatüre, S. Gulde, S. Falt, E. Hu, and A. Imamoglu, "Quantum nature of a strongly coupled single quantum dot-cavity system," *Nature*, vol. 445, pp. 896–899, Feb 2007.

[37] A. Högele, S. Seidl, M. Kroner, K. Karrai, R. Warburton, B. Gerardot, and P. Petroff, "Voltage-Controlled Optics of a Quantum Dot," *Physical Review Letters*, vol. 93, Nov 2004.

[38] D. Haft, C. Schulhauser, A. Govorov, R. Warburton, K. Karrai, J. Garcia, W. Schoedfeld, and P. Petroff, "Magneto-optical properties of ring-shaped self-assembled InGaAs quantum dots," *Physica E*, vol. 13, pp. 165–169, 2002.

[39] A. Kiraz, P. Michler, C. Becher, B. Gayral, A. Imamoglu, L. Zhang, E. Hu, W. Schoenfeld, and P. Petroff, "Cavity-quantum electrodynamics using a single InAs quantum dot in a microdisk structure," *Applied Physics letters*, vol. 78, pp. 3932–3934, June 2001.

[40] S. Seidl, M. K. amd Alexander Högele, K. Karrai, R. J. Warburton, A. Badolato, and P. M. Petroff, "Effect of uniaxial stress on excitons in a self-assembled quantum dot," *Applied Physics letters*, vol. 88, no. 203113, 2006.

[41] W. Fon, K. Schwab, J. Worlock, and M. Roukes, "Phonon scattering mechanisms in suspended nanostructures from 4 to 40 K," *Physical Review B*, vol. 66, no. 045302, 2002.

[42] M. O. S. . M. S. Zubairy, *Quantum Optics*. Cambridge: Cambridge Univ. Press, 1997.

[43] C. Thurmond, "The standard thermodynamic functions for the formation of electrons and holes in Ge, Si, GaAs and GaP," *J. Electrochem. Soc.*, vol. 122, no. 1133, 1975.

[44] K. Hennessy, A. Badolato, A. Tamboli, P. M. Petroff, E. Hu, M. Atatüre, J. Dreiser, and A. Imamoglu, "Tuning photonic crystal nanocavity modes by wet chemical digital etching," *Applied Physics Letters*, vol. 87, no. 021108, 2005.

[45] S. Strauf, M. T. Rakher, I. Carmeli, K. Hennessy, C. Meier, A. Badolato, M. J. A. DeDood, P. M. Petroff, E. L. Hu, E. G. Gwinn, and D. Bouwmeester, "Frequency

control of photonic crystal membrane resonators by monolayer deposition," *Applied Physics Letters*, vol. 88, no. 043116, 2006.

[46] T. Yoshie, A. Scherer, J. Hendrickson, G. Khitrova, H. M. Gibbs, G. Rupper, C. Ell, O. B. Shchekin, and D. G. Deppe, "Vacuum Rabi splitting with a single quantum dot in a photonic crystal nanocavity," *Nature*, vol. 432, pp. 200–203, Nov. 2004.

[47] A. Rastelli, A. Ulhaq, S. Kiravittaya, L. Wang, A. Zrenner, and O. Schmidt, "In situ laser microprocessing of single self-assembled quantum dots and optical microcavities," *Applied Physics Letters*, vol. 90, no. 073120, 2007.

[48] A. Faraon, D. Englund, I. Fushman, N. Stoltz, P. Petroff, and J. Vuckovic, "Local quantum dot tuning on photonic crystal chips," *Applied Physics Letters*, vol. 90, no. 213110, 2007.

[49] S. Song, S. S. Howard, Z. Liu, A. O. Dirisu, C. F. Gmachl, and C. B. Arnold, "Mode tuning of quantum cascade lasers through optical processing of chalcogenide glass claddings," *Applied Physics Letters*, vol. 89, no. 041115, 2006.

[50] M. W. Lee, C. Grillet, C. L. Smith, D. J. Moss, B. J. Eggleton, D. Freeman, B. Luther-Davies, S. Madden, A. Rode, Y. Ruan, and Y. hee Lee, "Photosensitive post tuning of chalcogenide photonic crystal waveguides," *Optics Express*, vol. 15, no. 3, p. 1277, 2007.

[51] A. Faraon, D. Englund, D. Bulla, B. Luther-Davies, B. J. Eggleton, N. Stoltz, P. Petroff, and J. Vuckovic, "Local tuning of photonic crystal cavities using chalcogenide glasses," *Applied Physics Letters*, vol. 92, no. 043123, 2008.

[52] A. Schulte, C. Rivero, K. Richardson, K. Turcotte, V. Hamel, A. Villeneuve, T. Galstain, and R. Vallee, "Bulk-film structural differences of chalcogenide glasses probed in situ by near-infrared waveguide Raman spectroscopy," *Optics Communications*, vol. 1, pp. 125–128, October 2001.

[53] S. Kugler, J. Hegedus, and K. Kohary., "Modelling of photoinduced changes in chalcogenide glasses: a-Se and a-As_2Se_3," *J Mater Sci: Mater Electron*, vol. 18, pp. S163–S167, 2007.

[54] S. J. Skuban, F. Skuban, S. R. Lukic, and Z. Cvejic, "Thermal Coefficient of linear expansion of non-crystalline chalcogenides in the AsSSeTeI system," *Journal of Thermal Analysis and Calorimetry*, vol. 71, pp. 439–444, 2003.

[55] V. Spezialwerkstroffe, "http://cvdmaterials.de/chalcogenide_glasses.htm," 2007.

[56] V. F. Chuprakov, V. V. Sakharov, N. M. Kononova, E. N. L. abd G. E. Kharitonova, and I. A. Baryshnikov, "Infrared chalcogenide optical fibers," *Glass and Ceramics*, vol. 48, no. 5, 1991.

[57] J. C. Sturm, H. Manoharan, L. C. Lenchyshyn, M. L. W. Thewalt, N. L. Rowell, J.-P. Noël, and D. C. Houghton, "Well-resolved band-edge photoluminescence of excitons confined in strained $si_{1-x}ge_x$ quantum wells," *Phys. Rev. Lett.*, vol. 66, pp. 1362–1365, Mar 1991.

[58] J. M. Raimond, M. Brune, and S. Haroche, "Manipulating quantum entanglement with atoms and photons in a cavity," *Rev. Mod. Phys.*, vol. 73, pp. 565–582, Aug 2001.

[59] A. Wallraff, D. I. Schuster, A. Blais, L. Frunzio, R. S. Huang, J. Majer, S. Kumar, S. M. Girvin, and R. J. Schoelkopf, "Circuit quantum electrodynamics: Coherent coupling of a single photon to a cooper pair box," *Nature*, vol. 431, p. 162, 2004.

[60] K. Srinivasan and O. Painter, "Linear and nonlinear optical spectroscopy of a strongly coupled microdiskquantum dot system," *Nature*, vol. 450, pp. 862–866, 2007.

[61] G. Nogues, A. Rauschenbeutel, S. Osnaghi, M. Brune, J. M. Raimond, and S. Haroche, "Seeing a single photon without destroying it," *Nature*, vol. 400, pp. 239–242, 1999.

[62] B. D. Gerardot, S. Seidl, P. A. Dalgarno, R. J. Warburton, M. Kroner, K. Karrai, A. Badolato, and P. M. Petroff, "Contrast in transmission spectroscopy of a single quantum dot," *Applied Physics Letters*, vol. 90, no. 22, p. 221106, 2007.

[63] D. Englund, A. Majumdar, A. Faraon, M. Toishi, N. Stoltz, P. Petroff, and J. Vuckovic, "Coherent excitation of a strongly coupled quantum dot - cavity system," *arXiv:0902.2428v2*, 2009.

[64] A. Imamoglu, H. Schmidt, G. Woods, and M. Deutsch, "Strongly Interacting Photons in a Nonlinear Cavity," *Physical Review Letters*, vol. 79, pp. 1467–1470, August 1997.

[65] D. E. Chang, A. S. Sorense, E. A. Demler, and M. D. Lukin, "A single-photon transistor using nanoscale surface plasmons," *Nature Physics*, vol. 3, pp. 807–812, November 2007.

[66] D. Englund, A. Faraon, B. Zhang, Y. Yamamoto, and J. Vučković, "Generation and Transfer of Single Photons on a Photonic Crystal Chip," *Optics Express*, vol. 15, April 2007.

[67] H. Carmichael, R. J. Brecha, and P. R. Rice, "Quantum interference and collapese of the wavefunction in cavity QED," *Optics Communications*, vol. 82, pp. 73–79, April 1991.

[68] C. Santori, D. Fattal, J. Vuckovic, G. S. Solomon, E. Waks, and Y. Yamamoto, "Submicrosecond correlations in photoluminescence from InAs quantum dots," *Physical Review B*, vol. 69, no. 205324, 2004.

[69] G. C. Hegerfeldt and D. Seidel, "The intensity correlation function of &lquot;blinking&rquot; quantum systems," *Journal of Optics B: Quantum and Semiclassical Optics*, vol. 4, no. 5, pp. 245–250, 2002.

[70] S. M. Tan, "A computational toolbox for quantum and atomic physics," *J. Opt. B*, vol. 1, pp. 424–432, 1999.

[71] J. Vučković, D. Englund, D. Fattal, and E. W. Y. Yamamoto, "Generation and manipulation of nonclassical light using photonic crystals," *Physica E*, vol. 31, no. 2, 2006.

[72] A. Faraon, E. Waks, D. Englund, I. Fushman, and J. Vuckovic, "Efficient photonic crystal cavity-waveguide couplers," *Applied Physics Letters*, vol. 90, no. 073102, 2007.

[73] S. Noda, A. Chutinan, and M. Imada, "Trapping and emission of photons by a single defect in a photonic bandgap structure," *Nature*, vol. 407, pp. 608–610, oct 2000.

[74] T. Tanabe, M. Notomi, E. Kuramochi, A. Shinya, and H. Taniyama, "Trapping and delaying photons for one nanosecond in an ultrasmall high-Q photonic-crystal nanocavity," *Nature Photonics*, vol. 1, pp. 49–52, 2006.

[75] S. Noda, A. Chutinan, and M. Imada, "Trapping and emission of photons by a single defect in a photonic bandgap structure," *Nature*, vol. 407, pp. 608–610, 2000.

[76] A. Faraon, I. Fushman, D. Englund, N. Stoltz, P. Petroff, and J. Vuckovic, "Dipole induced transparency in waveguide coupled photonic crystal cavities," *OPTICS EXPRESS*, vol. 16, pp. 12154–12162, AUG 4 2008.

[77] E. Waks and J. Vučković, "Coupled mode theory for photonic crystal cavity-waveguide interaction," *Optics Express*, vol. 13, pp. 5064 – 5073, June 2005.

[78] G. H. Kim, Y. H. Lee, A. Shinya, and M. Notomi, "Coupling of small, low-loss hexapole mode with photonic crystal slab waveguide mode," *Optics Express*, vol. 12, pp. 6624–6631, Dec. 2004.

[79] A. Shinya, S. Mitsugi, T. Tanabe, M. Notomi, I. Yokohama, H. Takara, and S. Kawanishi, "All-optical flip-flop circuit composed of coupled two-port resonant tunneling filter in twodimensional photonic crystal slab," *Optics Express*, vol. 14, pp. 1230–1235, Feb. 2006.

[80] A. Shinya, S. Mitsugi, E. Kuramochi, and M. Notomi, "Ultrasmall multi-channel resonant-tunneling filter using mode gap of width-tuned photonic-crystal waveguide," *Optics Express*, vol. 13, May 2005.

[81] D. Englund and J. Vučković, "A direct analysis of photonic nanostructures," *Optics Express*, vol. 14, no. 8, pp. 3472–3483, 2006.

[82] X. Letartre, C. Seassal, C. Grillet, P. Rojo-Romero, P. Viktorovitch, M. L. V. d'Yerville, D. Cassagne, and C. Jouanin, "Group velocity and propagation losses measurement in a single-line photonic-crystal waveguide on InP membranes," *Applied Physics Letters*, vol. 79, pp. 2312–2314, Oct. 2001.

[83] A. Högele, S. Seidl, M. Kroner, K.Karrai, R. J. Warburton, B. D. Gerardot, and P. M. Petroff, "Voltage-Controlled Optics of a Quantum Dot," *Physical Review Letters*, vol. 93, nov 2004.

[84] D. Loss and D. P. DiVincenzo, "Quantum computation with quantum dots," *Physical Review A*, vol. 57, pp. 120–126, 1998.

[85] A. Imamoglu, D. D. Awschalom, G. Burkard, D. P. DiVincenzo, D. Loss, M. Sherwin, and A. Small, "Quantum Information Processing Using Quantum Dot Spins and Cavity QED," *Physical Review Letters*, vol. 83, pp. 4204–4207, November 1999.

[86] G. Medeiros-Ribeiro, D. Leonard, and P. M. Petroff, "Electron and hole energy levels in inas self-assembled quantum dots," *Applied Physics Letters*, vol. 66, no. 14, pp. 1767–1769, 1995.

[87] B. D. Gerardot, D. Brunner, P. A. Dalgarno, P. Ohberg, S. Seidl, M. Kroner, K. Karrai, N. G. Stoltz, P. M. Petroff, and R. J. Warburton, "Optical pumping of a single hole spin in a quantum dot," *NATURE*, vol. 451, pp. 441–444, JAN 24 2008.

[88] J. Berezovsky, M. H. Mikkelsen, N. G. Stoltz, L. A. Coldren, and D. D. Awschalom, "Picosecond Coherent Optical Manipulation of a Single Electron Spin in a Quantum Dot," *Science*, vol. 320, no. 5874, pp. 349–352, 2008.

[89] D. A. B. Miller, D. S. Chemla, T. C. Damen, A. C. Gossard, W. Wiegmann, T. H. Wood, and C. A. Burrus, "Band-edge electroabsorption in quantum well structures: The quantum-confined stark effect," *Phys. Rev. Lett.*, vol. 53, pp. 2173–2176, Nov 1984.

[90] A. Laucht, F. Hofbauer, N. Hauke, J. Angele, S. Stobbe, M. Kaniber, G. Bohm, P. Lodahl, M. C. Amann, and J. J. Finley, "Electrical control of spontaneous emission and strong coupling for a single quantum dot," *arXiv:0810.3010v2*, 2008.

[91] B. D. Gerardot, S. Seidl, P. A. Dalgarno, R. J. Warburton, D. Granados, J. M. Garcia, K. Kowalik, O. Krebs, K. Karrai, A. Badolato, and P. M. Petroff, "Manipulating exciton fine structure in quantum dots with a lateral electric field," *Applied Physics Letters*, vol. 90, no. 4, p. 041101, 2007.

[92] V. Stavarache *et al.*, "Control of quantum dot excitons by lateral electric fields," *Appl. Phys. Lett.*, vol. 89, no. 12, p. 123105, 2006.

[93] X. Xu *et al.*, "Manipulating quantum-confined stark shift in electroluminescence from quantum dots with side gates," *New Journal of Physics*, vol. 10, no. 5, p. 053036, 2008.

[94] W. Heller, U. Bockelmann, and G. Abstreiter, "Electric-field effects on excitons in quantum dots," *Phys. Rev. B*, vol. 57, pp. 6270–6273, Mar 1998.

[95] A. Faraon and J. Vuckovic, "Local temperature control of photonic crystal devices via micron-scale electrical heaters," *Appl. Phys. Lett.*, vol. 95, no. 4, p. 043102, 2009.

[96] A. Faraon, A. Majumdar, H. K. , P. Petroff, and J. Vuckovic, "Fast Electrical Control of a Quantum Dot Strongly Coupled to a Nano-resonator," *arXiv:0906.0751v1*, 2009.

[97] C. Schneider, M. Strauss, T. Sunner, A. Huggenberger, D. Wiener, S. Reitzenstein, M. Kamp, S. Hofling, and A. Forchel, "Lithographic alignment to site-controlled quantum dots for device integration," *Applied Physics Letters*, vol. 92, no. 18, p. 183101, 2008.

[98] A. Majumdar, Z. Lin, A. Faraon, and J. Vuckovic, "Fast, high fidelity quantum dot spin initialization without a strong magnetic field by two-photon processes," 2009.

[99] Z. Lin and J. Vuckovic, "Enhanced two-photon processes in quantum dots inside photonic crystal nanocavities and quantum information processing applications," 2009.